A Novel Linear Motor for a Linear Refrigeration Compressor: Modelling, Measurement and Sensor-less Stroke Detection

Hanying Jiang

A thesis submitted to the University of Sussex

For the degree of Doctor of Philosophy

January 2021

Declaration

I hereby declare that this thesis has not been and will not be, submitted in whole or in part to another University for the award of any other degree.

Signature:.....

Date:.....

Abstract

With the increasing global awareness of the environmental conservation, linear compressors have attracted growing attention with their applications in domestic and cryogenic refrigeration systems. A linear compressor is driven directly by a linear motor and the free-piston design allows piston stroke to be variable. An active control of stroke prevents piston-cylinder collision and enables efficient cooling capacity modulation. This thesis introduces the performance of a novel moving magnet type linear compressor/motor and investigates the approaches to sensor-less stroke detection.

An experimental test facility incorporating the linear compressors into a vapour compression refrigeration system was introduced, in which piston displacement was measured with a displacement sensor. The piston stroke and offset were controlled with PID controllers implemented in LabVIEW.

To investigate the characteristics of the moving magnet linear motor, a finite element analysis (FEA) model was built in ANSYS Maxwell 19.2. Simulations were validated through static force measurements. Force constant was given by the static shaft force against current. Saturation can be observed with the increase of current. A smaller saturation current was shown for a larger armature displacement.

For the purpose of increasing cooling capacity of the linear compressor, operations with small axial clearance volumes were considered. Refrigeration performance using R1234yf as refrigerant with various clearance volumes and with an offset of 0 mm were experimentally compared. The cooling capacity for a pressure ratio of 2.5 and a stroke of 13 mm increases by 12% as the clearance decreases from 1.07 mm to 0.4 mm.

Piston stroke detection without a displacement sensor reduces the cost and facilitates the stroke control especially in miniature linear compressors. An artificial neural network (ANN) based stroke detection was presented. Fast Fourier transform (FFT) analysis was performed on current and voltage signals to extract harmonic terms as inputs of the neural network model to predict the stroke. The ANN technique can achieve a good accuracy for most of the cases, but reliability remains a problem.

A more reliable sensor-less stroke detection technique based on flux linkage variation using inductive coils was proposed. The technique requires resonant operation. A 1D (One-Dimensional) electromagnetic model and a 3D (Three-Dimensional) FEA model were built to compute the flux linkage variations. The open-circuit flux linkage in each core produced by NdFebB magnets varies linearly with the piston displacement. Flux linkage difference at two zero-crossing points of current was used to infer stroke. The proposed low-cost sensor-less stroke detection technique can achieve error of only 4%. The adoption of this novel technique is crucial to the commercialization of free-piston machines for high efficiency.

Acknowledgements

The thesis could not have been completed without the help of a number of people.

I am grateful for my main supervisor, Dr. Kun Liang, for his direction and support throughout the study. His enthusiasm for research has influenced me greatly. I would like to thank my second supervisor, Prof. J. F. Dunne, for his advices and encouragement at annual review meetings.

My thanks to my colleagues for their help. It was important to have a discussion with them when I encountered difficulties at research.

I owe particular thanks to my family. My family has given firm support to me when I experienced stressful times. My grandma's care has always been my biggest motivation to carry on.

Last but not least, I would like to express my gratitude to the School of Engineering and Informatics, University of Sussex for offering me the Sussex PhD Scholarship.

Contents

Nomenclature

Acronyms

1D	One-Dimensional
3D	Three-Dimensional
AC	Alternating current
ANN	Artificial neural network
CoP	Coefficient of performance
DAQ	Data acquisition device
DC	Direct current
EMF	Electromotive force
FEA	Finite element analysis
FFT	Fast Fourier transform
HDAQ	High-speed data acquisition
LabVIEW	Laboratory Virtual Instrument Engineering Workbench
LDAQ	Low-speed data acquisition
LVDT	Linear variable differential transducer
MEC	Magnetic equivalent circuit
MSE	Mean squared error
PE	Percentage error
PID	Proportional-integral-derivative
PR	Pressure ratio
P-V	Pressure-volume
PWM	Pulse width modulation

R	Correlation coefficient
ROM	Read only memory
RLC	Resistor, inductor, and capacitor
RMS	Root mean square
SR	Stroke ratio
TDC	Top dead centre
THD	Total Harmonic Distortion
VCR	Vapour compression refrigeration
VI	Virtual instrument

Greek

α	Shaft force constant/Eddy loss coefficients
β	Thrust coefficient
γ	Adiabatic index
δ	Liquid film thickness
ζ	Damping ratio
η	Efficiency
θ	Phase difference
κ	Thermal conductivity
μ	Permeability
ρ	Density
σ	Conductivity
ϕ	Magnetic flux/ Phase in each harmonic term
φ	Magnetic scalar potential
ω	Frequency

Roman

A	Area
B	Flux desnsity
C	Capacitance
c	Clearance
CL	Clearance ratio
Cov	Covariance
D	Diameter
d	Piston offset
f	Frequency
F	Force
G	Mass flux
g	Air gap
H	Magnetic field density
h	Enthalpy
I	Current
J	Current density.
k	Stiffness
L	Inductance/Length
M	Magnetization
MLP	Multi-layer perceptron
m	Moving Mass
$\dot{m}$	Mass flow rate
n	Polytropic index

P	Pressure
$\dot{Q}$	Cooling capacity
R	Resistance/Reluctance
S	Stroke
t	Time
T	Temperature/Time/Target
u	Average velocity of vapour
V	Voltage/Velocity/Volume
w	Width
x	Displacement
$\dot{x}$	Velocity
$\ddot{x}$	Acceleration
y	Network output

Subscripts

0	Vacuum
adb	Adiabatic
c	Cooling/Clearance
core	Core
cu	Copper
d	Discharge
e	Eddy current/Experimental
eva	Evaporator
full	Full
g	Gas

h	hysteresis
i	Input
iso	Isothermal
m	Motor
ma	Magnet
max	Maximum
me	Mechanical
min	Minimum
ms	Magnetic spring
o	Overall
p	Permanent
rms	Root mean square
s	Shaft/Suction/Swept
t	Theoretical/Thermodynamic

List of Figures

List of Tables

1

2

Chapter 1 Background

1.1 Linear Compressors

1.1.1 Background

The recent global awareness of the environmental conservation has drawn growing attention to the energy efficiency of domestic refrigeration and cryogenic refrigeration systems. Cryogenic refrigeration is distinguished from conventional refrigeration in that cooling temperature for a cryogenic refrigeration system is below 150 °C. As one of the most popular household appliances, domestic refrigerator was claimed to consume about 30% of the total electricity in a household and around 17% of the total electricity used worldwide, where there are currently more than 1.5 billion domestic refrigerators in use **[1]**. For several decades, the imminent growth in the refrigeration industry also resulted in a notable increase in energy usage. Thus, refrigeration systems are a key point of interest in pursuit of the environmental impact improvements. Cryogenics plays a vital role on board space-science missions, with a variety of applications, mostly in the domain of astrophysics. To date, Stirling cycle and pulse tube cryocoolers have been used for many years to reach cryogenic temperatures. Vapour compression refrigeration (VCR) system is undoubtedly the most widely adopted technology for domestic refrigeration and air-conditioning. A compressor functions as a key component of a VCR system, and a Stirling cycle or pulse tube cryocooler, and the technical characteristics of the compressor dominates the energy consumption of the system.

Key approach to reducing the environmental impact of refrigeration systems is to develop compressors that are able to deliver higher levels of energy efficiency. Rotary compressors (shown in Fig.1.1) have been studied because of their compact structures, strong adaptability, reliabilities, and low cost **[2, 3]**. A lot of researches have been carried out to improve the efficiency of rotary compressors by optimizing the compression part design to reduce the mechanical losses **[3-5]** and using vapour injection technology **[2, 6]**.

Compared with reciprocating compressors, rotary compressors are lighter in weight, do not require heavy foundations, and experiences less vibration **[7]**. However, rotary compressors are more expensive and require higher maintenance cost, and most importantly, the capacity and pressure ratio cannot be adjusted.

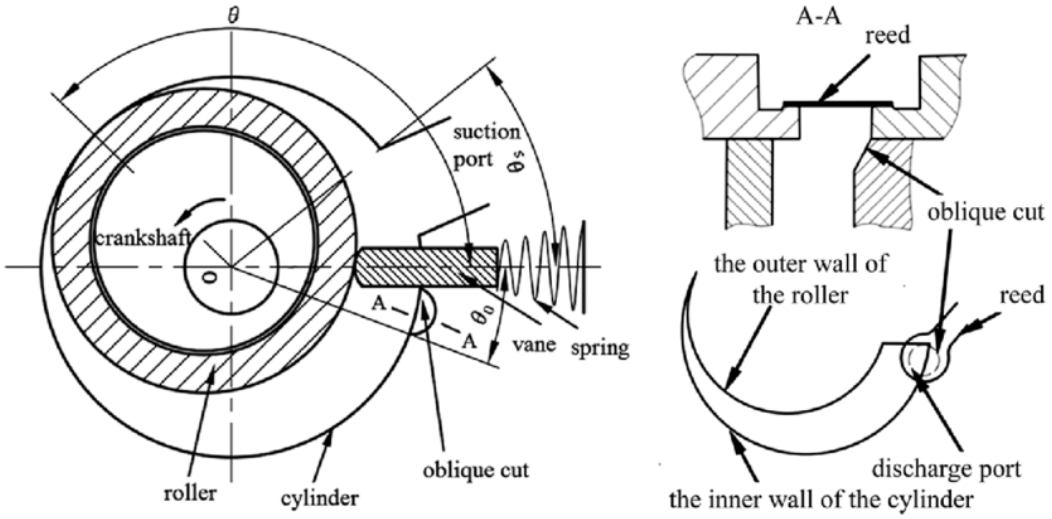

Fig. 1.1 Schematic of a rotary compressor **[8]**

Crank-drive reciprocating compressor has been commonly used in domestic refrigerators. Manufacturers have paid much attention to other types of compressors, as the energy dissipation of mechanical friction due to crank-driven mechanism is undesirable. Linear compressors were selected from alternative candidate technologies for the application in commercial refrigerator and air-conditioner appliances.

1.1.2 Developments of Linear Compressors

A linear compressor is a positive displacement compressor, where the piston is directly driven by a linear motor as shown in Fig. 1.2. Linear compressors, with clearance seals and flexure bearings, have been used for many years to generate pressure wave in Stirling cycle cryocoolers, and the same technology, with the addition of valves, can be used for VCR systems.

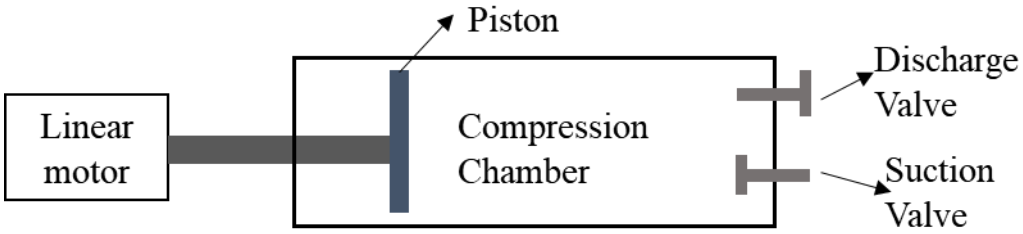

Fig. 1.2 Schematic of a linear compressor

The concepts of linear compressor date back to the 1950s when they were proposed in the Europe and Japan for the application in refrigeration systems **[9]**. However, neither sufficient theoretical study nor commercial linear compressor was reported at that time. Cadman et al. **[10, 11]** developed an approximate method for the design of linear compressor in 1969. In the late 1970s, University of Oxford started to develop the first-generation linear compressor for the space cryocoolers in satellites, and followed by the other two generations of linear compressors developed in 1988 and 2011 for the purpose of cost reduction and compactness **[12, 13]**. Sunpower Inc. has played a significant role in the development of linear compressors since 1992, when the design and simulation of a linear compressor for application in residential refrigerators were presented **[14]**. Several prototyped linear compressors were reported, and some experimental works and modelling of linear compressor were conducted.. Their linear compressors show good potential for the replacement of conventional compressors in refrigeration and cryogenic systems **[15-20].** Unger and Novotny **[20]** reported a compact design of linear compressor, for CPU cooling developed by Sunpower and Sun Microsystems, as shown in Fig. 1.3. Sunpower's free-piston linear compressor technology was adopted in the design, in which traditional oil lubricated bearings were replaced by a gas bearings system. The linear compressor was designed to achieve a cooling capacity of 1200 W. It was reported that a 1250 W heat load was removed and the coefficient of performance (COP), which is defined as the ratio of cooling capacity over power consumption, was 3.6 at an evaporator and condenser temperature of 20°C and 55°C, respectively, with a frequency of 95 Hz.

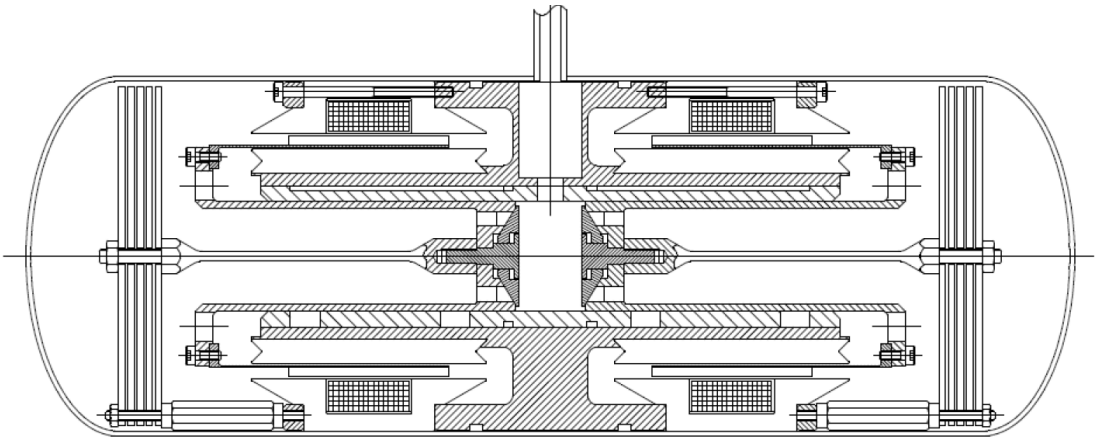

Fig. 1.3 Schematic of a Sunpower design for CPU cooling applications **[20]**

Several designs of linear compressors have been patented and commercialized by LG, Inc. with the employment of the linear motor technology developed by Sunpower Inc. to power the piston oscillation **[21-24]**. The linear compressors have been applied into domestic refrigerators with R600a and R134a as refrigerants. Fig. 1.4 shows a LG type linear compressor for air conditioning. All the LG linear compressors require oil lubrication, and were designed with a number of coil springs and damping systems. A prototype linear compressor as shown in Fig. 1.5 for electronics cooling was reported by Bradshaw et al. **[25, 26]**. The overall displacement of the miniature linear compressor is around 3 cm^3, and the average stroke is 0.6 cm. A comprehensive model including the compression process, heat transfer, leakage model and valve model was also presented. Piston stroke, which means the full travel of a piston along a cylinder was predicted within an error of 1.3%, and the accuracy for volumetric and overall isentropic efficiencies were 24% and 31%, respectively.

Fig. 1.4 LG type linear compressor for air conditioning **[24]**

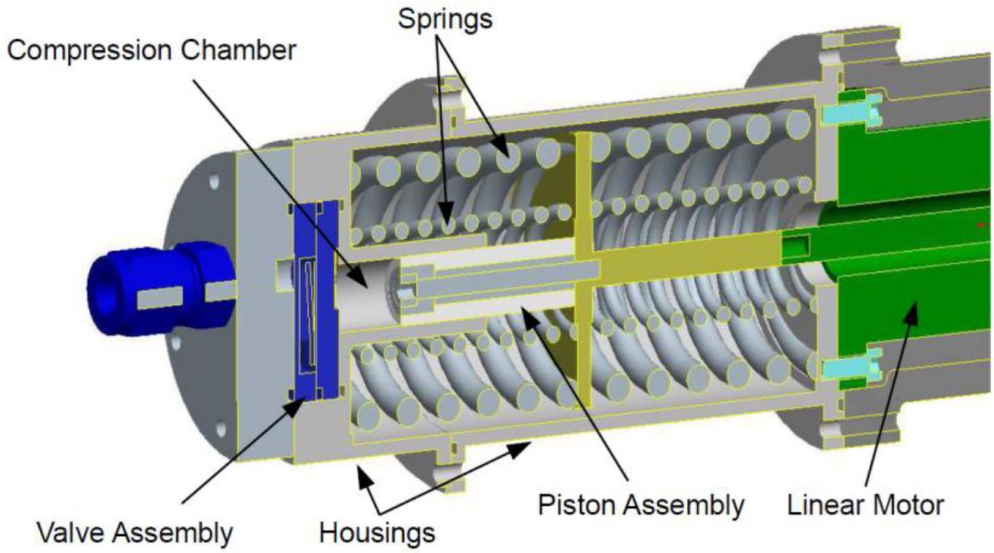

Fig. 1.5 Sectional view of the prototype linear compressor **[25]**

Embraco **[27]** reported another oil-free commercialized linear compressor designed for household refrigerator as shown in Fig. 1.6. The developed linear compressor employing surface gas bearings is a lubricant-free design. Possamai et al. **[28]** introduced a compact refrigeration system designed for a laptop cooling, in which a moving magnet linear compressor was used to drive refrigerant. Operating frequency was proven to have a great influence on size of the linear motor and linear compressor. Under final project conditions, the linear motor efficiency was about 71% and the isentropic compression efficiency was about 42%. Recent developments of linear compressors also include a moving magnet

linear compressor that was recently proposed by Bijanzad et al. **[29, 30]**. However, few of the reported linear compressors have been marketed to date.

Fig. 1.6 Oil-free linear compressor developed by Embraco **[27]**

1.1.3 Comparison with Crank-drive Reciprocating Compressors

Linear compressors employ a different design than either crank-driven reciprocating compressors and they are potentially more efficient than crank-driven compressors. Most linear compressor designs use a free piston arrangement and can be controlled for a range of capacities through adjustment of piston displacement. A general schematic of a crank-drive reciprocating compressor and a linear compressor are shown in Fig. 1.7 and Fig. 1.8 respectively. Compared with crank-drive compressors, the advantages of linear compressors include:

(1) Smaller mechanical friction loss due to the elimination of crank mechanism.

(2) Almost zero side force generated on piston due to operation along a single axis and the direct coupling between the motor and piston, so more stable operation can be assured and operation lifetime can be extended.

(3) Possibility of oil-free operation, as traditional bearings can be replaced by gas bearing systems. Lubricant-free operation allows more refrigerants choices and their

operating temperature range on one hand; On the other hand, it enables additional energy benefit by reducing pressure drop losses in heat exchangers.

(4) No on-off cycling loss, resonant operation and variable cooling capacity modulation. Refrigerator noise levels can also be decreased by operating most of the time at low capacity, similar to how variable-speed compressors are used. In addition, flexible cooling capacity modulation by stroke (peak-to-peak displacement) adjustment significantly reduces the cycling losses compared with the on-off control strategy for modulating.

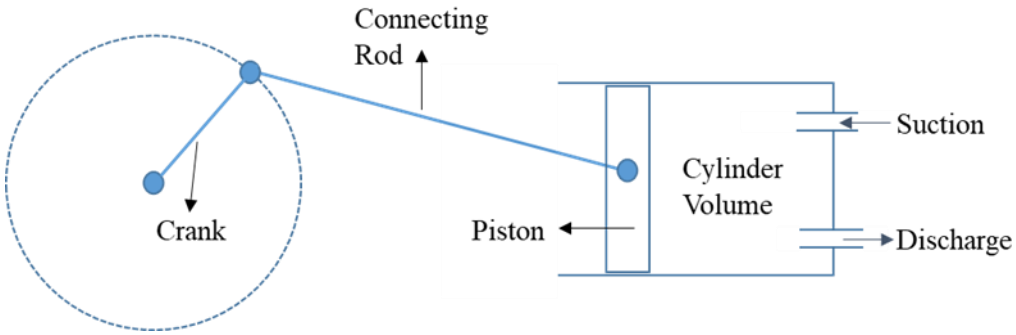

Fig. 1.7 Schematic of a crank-drive reciprocating compressor

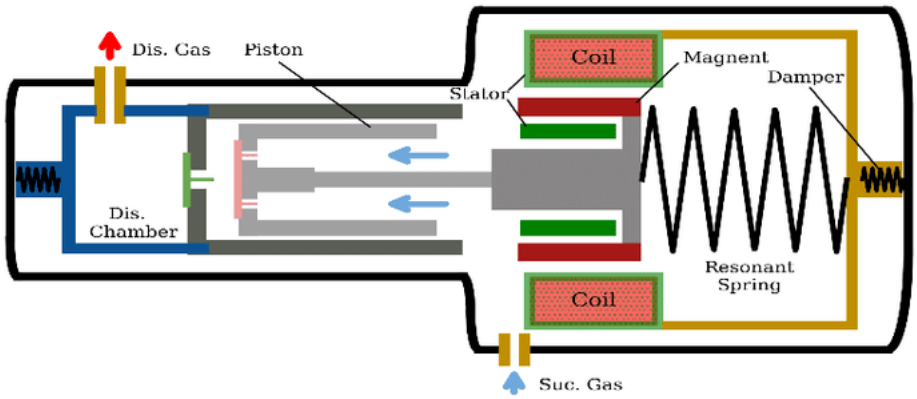

Fig. 1.8 Schematic of a prototyped linear compressor **[31]**

Compared with a crank-drive reciprocating compressor, the investigations carried out by Bradshaw et al. **[32]** shows that better energy recovery characteristics were shown in the linear compressor, and over a wider range of clearance volumes, the linear compressor shows higher efficiency. Ku et al. **[33]** and Park et. al **[21]** concluded that the efficiency

of linear compressors using linear motors designed by Sunpower Inc is above 10% higher than conventional crank-drive compressors, which can be explained by a higher motor efficiency of the linear motor . As shown in Fig. 1.9, the motor efficiency of the linear motor is significantly higher than the rotary induction motor, and the linear motor shows lower sensitivity to speed variation.

Liang et al. **[34]** experimentally compared a moving magnet linear compressor with a conventional crank-drive compressor. It was revealed that the linear motor shows much higher efficiency especially when power input is low. However, at the maximum stroke of 13 mm, about 20% volumetric efficiency was observed in the conventional crank-drive compressor due to its much smaller clearance volume (the volume between the cylinder head and the piston when the piston is at top dead centre). In the two review papers published by Bansal et al. **[35]** and Liang. et al. **[36],** linear compressors were considered as a promising alternative for conventional crank-drive compressors, but barriers still exist and more comprehensive comparisons can be quantitively investigated.

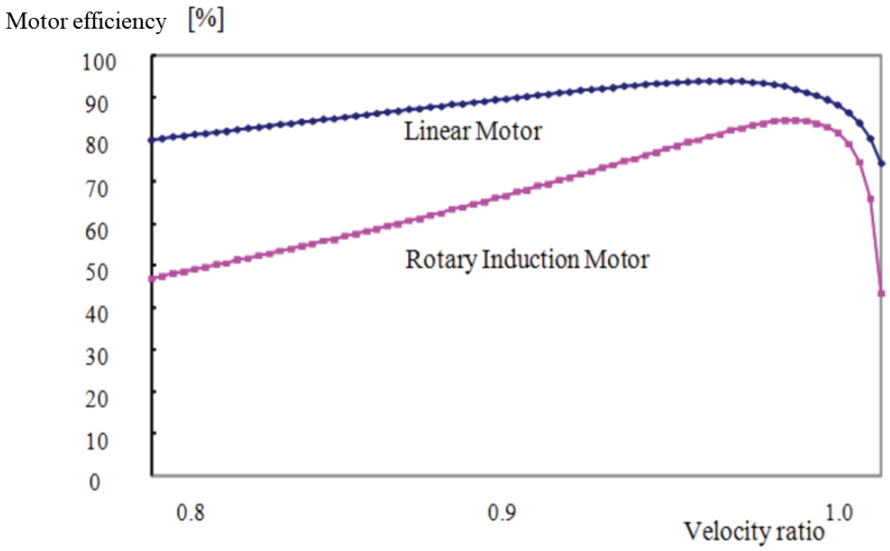

Fig. 1.9 Motor efficiency versus velocity ratio for linear motor and rotary induction motor **[33]**

1.1.4 Challenges

Although linear compressors have been developed for a long period, some key issues

remain unsolved and hinder the progress of the industrial application in the fields of refrigeration:

(1) Further increase in volumetric flow per compressor size to achieve more compact design and higher refrigeration performance **[37]**.

(2) The efficiency of a linear motor is still in need of improvement.

(3) Cost is the main challenge of a linear compressor. Expensive rare earth material is usually used in linear motors to achieve higher motor efficiency, extra manufacturing requirement, i.e. clean room, and solenoid valves also increase the cost of linear compressors **[36]**.

(4) Designing linear compressor for high power application such as air conditioner is very challenging due to high clearance loss, high piston offset, and very non-linear gas spring at high pressure ratios **[38]**.

(5) Different from a crank-drive reciprocating compressor, the motion of piston is not pre-defined by the geometry of crank and connecting rod. Piston position sensing is required for the stroke control, and to control top dead centre (TDC) (shown in Fig. 1.10) so as to prevent piston from colliding into cylinder head and more importantly to modulate the cooling capacity for VCR system. The control and piston displacement detection becomes more difficult for high-frequency linear compressors as higher resolution and faster response are required.

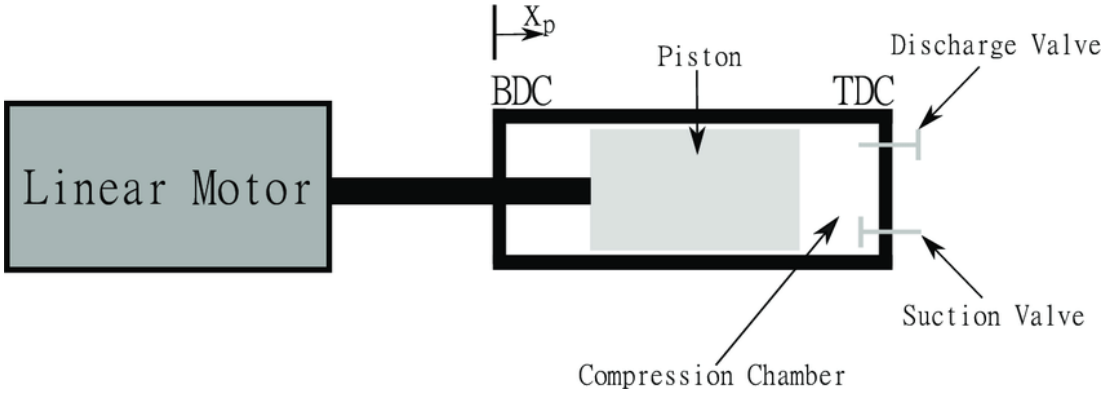

Fig. 1.10 Top dead centre and bottom dead centre in a linear compressor **[39]**

1.2 Linear Motors

1.2.1 Introduction

Linear motors are favoured when translational motions are required to be performed with high flexibility and low friction. A linear motor drives a motion in a single axis by electromechanical force without any motion conversion mechanism such as crankshafts, gears and screws **[40]**. The development of linear motor can be traced back to 1840s, when a pioneering early design of linear induction motor was proposed by Charles Wheatstone for the first time **[41]**. In 1905, Alfred Zehden patented a linear induction motor **[42]**. In the late 1940s, Eric Laithwaite, a British electrical engineer, developed the first full-size working model **[43]**. Many designs have been put forward for linear motors, falling into two major categories, i.e., low-acceleration and high-acceleration linear motors. The latter ones are usually very short, typically developed for hypervelocity appliances, such as mass drivers for spacecraft propulsion and weapons. The former ones have been extensively used in ground-based transportation systems, lifting pumps for deep mining, and other motion control systems. In the past few decades, a lot of work has been done to increase power density and motor efficiency, and to achieve more advanced controls. These advances enable linear motor an ideal solution for high precision motion control systems, e.g., linear compressors.

Linear motors can be considered as linear configurations of rotary motors by cutting the

rotary motor radially and unrolling the stators and rotors as shown in Fig. 1.11. The principle of operation is the same, however there are certain differences like air gap is usually bigger than in a rotary motor and a mover is shorter with respect to a track causing end effect **[44]**. The main technologies for linear machines are permanent magnet (PM) synchronous, induction and switched reluctance machines.

PM motors have the advantages of high power density, and motor efficiency, but the cost is relatively with the expensive permanent magnet. The construction of induction motors is simple; the cost of induction motors is also cheaper compared with other two types of linear motors. Induction motors share the merits of reliable operation and low maintenance operation. However, the speed and position control are more difficult. Switched reluctance motors provide good efficiency with low cost, and they are simple and robust, but the high noises and vibrations are the widely acknowledged drawbacks of them.

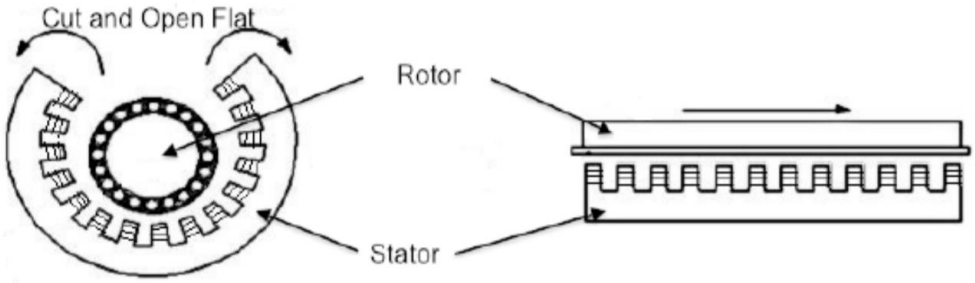

Fig. 1.11 Cutting radially and unrolling a rotary motor **[45]**

There are mainly four different approaches to producing a linear movement by an electrical way. The first solution is to use the electrostatic properties to move a glass way. A maximum force density of about 16 N/m^2 can be obtained **[46]**. As shown in Fig. 1.10, a movement can also be produced by an electromagnetic way. The third and fourth solutions based on mechanical friction use the piezoelectric or magnetostrictive properties to interact with a mover. The two variants differ by their respective material. For the first one, the force is produced under an electric field source (piezoelectric) and for the other one under a magnetic field source. The stroke of these motors is usually small. Fig. 1.12

shows categories of linear motors **[47]**. AC (Alternating Current) linear motors are mainly used to drive working fluid through refrigeration cycles.

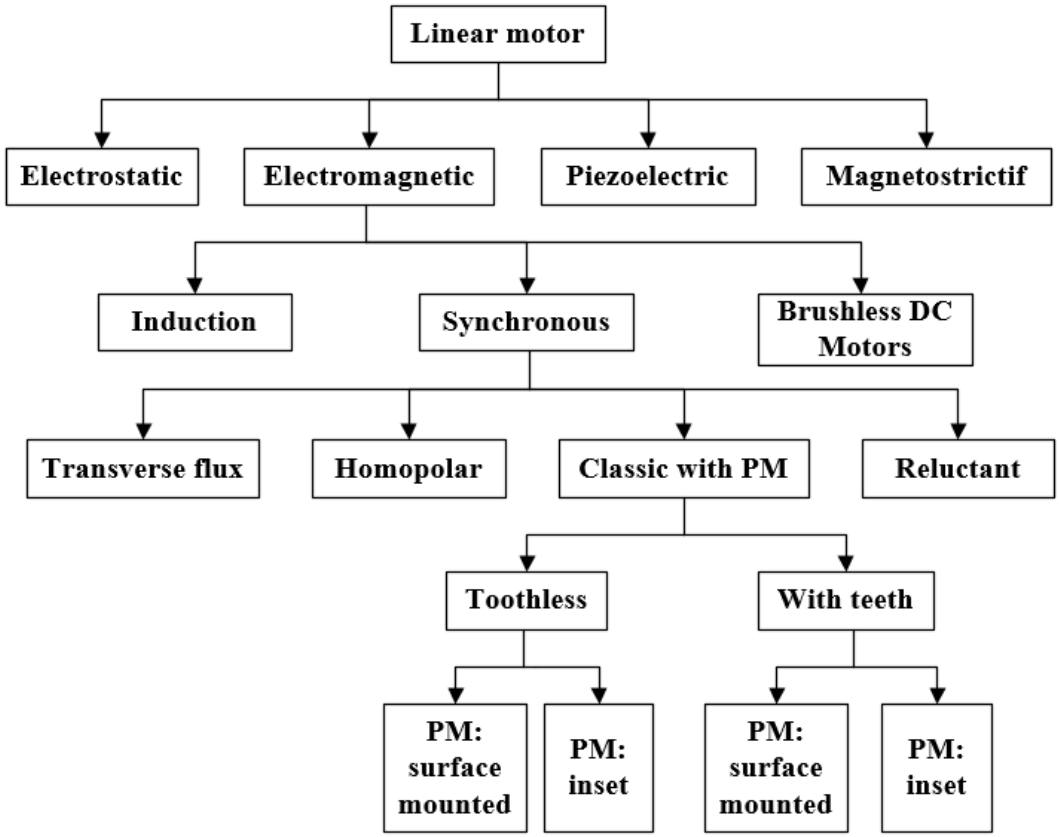

Fig. 1.12 Linear motor classification **[47]** (PM: Permanent Magnet)

Electromagnetic linear motors are composed mainly of three configurations: synchronous, induction or DC motors. The distinction between linear synchronous/DC and induction motors is excitation mode. Linear synchronous/DC motors are excited by PMs or electromagnets, whereas excitation in liner induction motor is generated by inducing current in the secondary. Sinewave current is supplied into linear synchronous motor to produce a sinusoidal electromagnetic force. However, in linear DC motors, trapezoidal electromagnetic force is generated with rectangular phase current supplied. Fig. 1.13 shows various possible topologies for linear motors. Independent of the motor type, linear motors can be single or double-sided, i.e. whether mover faces the stationary track from one side or both. A linear motor can be either flat or tubular. The length of the stator

(active part) compared to the reactive part defines the long-stator and the short-stator linear motor. In applications where high-power density is required, magnets can be embedded and mingled to form a 'Halbach array' **[48]**. Halbach array converge the magnetic field on one side while nullifying on the other.

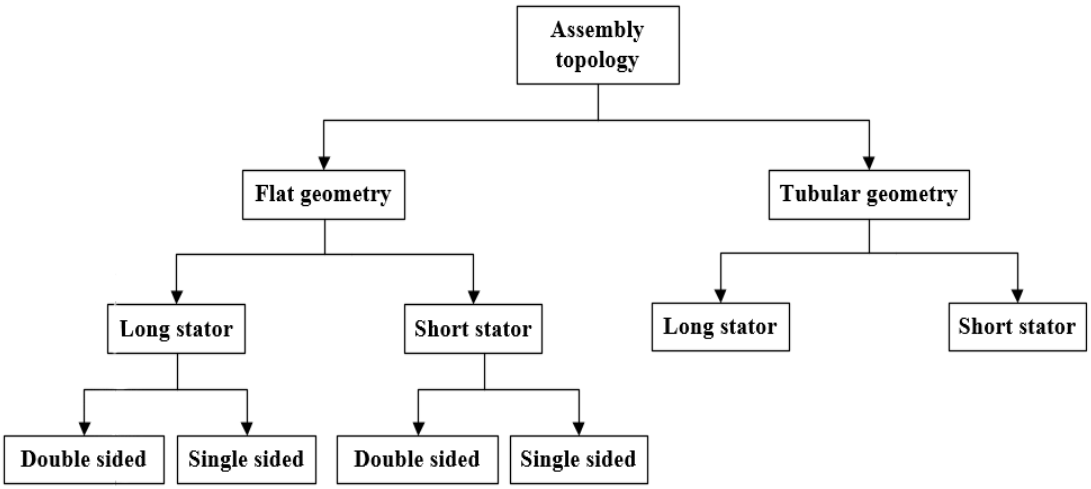

Fig. 1.13 Linear motor topologies **[47]**

Due to significantly greater efficiency and larger power density than other types of linear motors, linear permanent magnet motors are considered as the most appropriate ones for linear compressor applications. Existing permanent magnet linear motors are categorized as: moving coil, moving magnet, and moving iron only based on the respective moving components shown in Fig. 1.14. In general, each type of permanent magnet linear motor has their own pros and cons, depending on their practical applications.

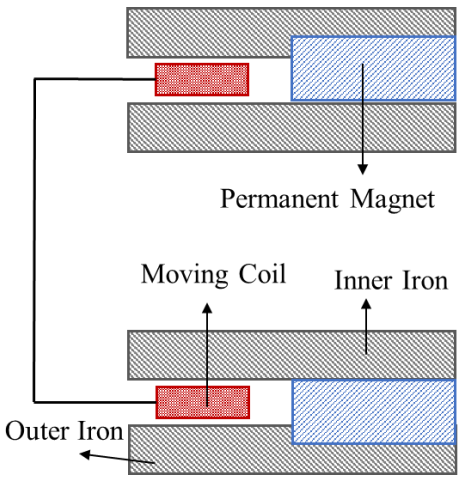

(a)

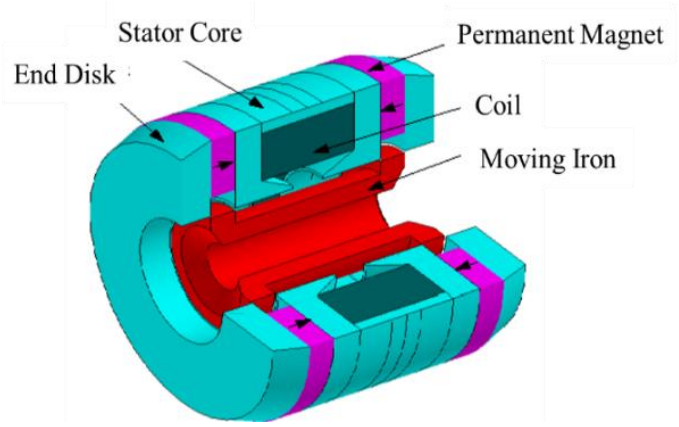

(b)

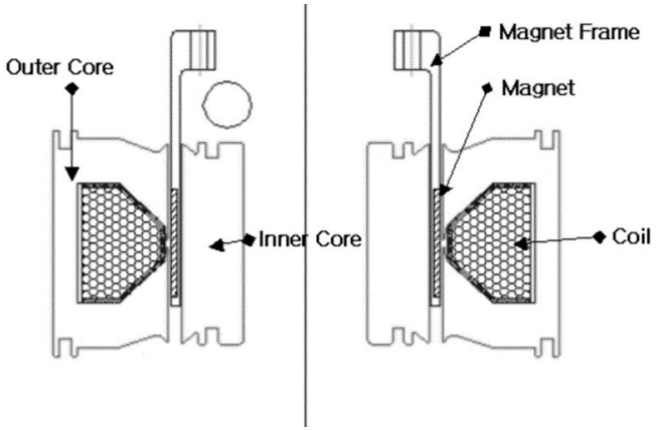

(c)

Fig. 1.14 Examples of three types of linear motors (a) moving coil **[17]** (b) moving iron **[49]** (c) moving magnet **[22]**

1.2.2 Moving Magnet Linear Motors

Reliability and high efficiency are two basic requirements for linear motors used in linear compressors. Typically, 20000 hours of maintenance-free operation should be offered, and demands for cost and functionality should be met, while criteria of minimum volume and loss being fulfilled. In addition to no flying leads, moving magnet linear motor has the merits of bidirectional force production, a high specific force capability, and good thermal dissipation **[50]**.

A tubular moving magnet linear motor with moving mass was manufactured by SunpowerInc , which consisted of a ferromagnetic, stationary armature, back iron and a

homopolar magnet with radical magnetization as shown in Fig. 1.14c. Almost the same motor design was applied to household linear refrigerator compressor systems **[22]**. This motor design remains one of the most extensively adopted linear motor in market. Nevertheless, an additional air gap exists in the topology, which leads to a high leakage field and compromises the force capability. Although the design enables low moving mass to improve the dynamic capability, the manufacturing cost is still high owing to the special support for the moving magnets in order to achieve robust reciprocating operation. Further, to produce same thrust force capability, larger number of turns of windings are needed, which causes a higher copper loss and lower efficiency **[51]**.

An initial design of linear permanent magnet motor aimed at application in a domestic refrigerator was proposed **[52]** and further optimization was carried out in terms of efficiency and cost **[53]**. The tubular linear motor used soft magnetic composites and buried ring-shaped magnet arrangement. A flux concentration-type linear motor with embedded axially magnetized bar-shaped magnets structure in the mover was patented **[54]**. Compared with the design with surface-mounted magnets, the proposed design eliminated the adhesive part that fixed the magnet to the mover, so higher reliability can be assured as mover performs a high-speed reciprocating motion. In addition, the flux concentration-type linear motor showed a higher power density and a lower cogging force **[50]**.

A recent design of linear motor for linear refrigerator compressor was proposed by Hassan et al. **[55]**. The stator assembly consisted of three parts: two oppositely circular-wound coils in series, coil holder, and the coil cover as shown in Fig. 1.15. The mover assembly was composed of magnet holder, three rows of radially magnetized magnets, and the spring mounting plate. Nickel (Ni-Cu-Ni) coated Sintered Neodymium N38H permanent magnets were used.

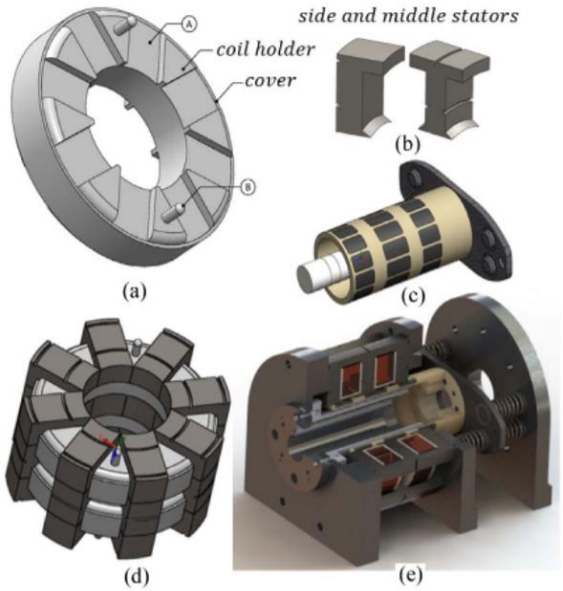

Fig. 1.15 CAD models of the linear actuator components: (a) Coil assembly; (b) stator core; (c) mover assembly; (d) stator assembly; (e) linear actuator assembly. **[55]**

Conventionally, permanent magnet arrays include axial and radial magnetization arrays. A general framework for tubular linear motors was presented **[56]**. The framework facilitated comparative studies on magnetization arrays, design optimization, and laid a foundation for multiple researches that was published later. With axial and radial magnetization magnet arrays, thick back-iron is required to create flux paths and minimize saturation **[53]**. For the purpose of back-iron thickness reduction, a Halbach array was used to weaken magnetic field in back-iron. In this way, the mover mass can be reduced. However, it is difficult to manufacture ideal Halbach magnetization magnets owing to complicated magnetization direction **[57]**. Generally, a quasi-Halbach array is a compromising solution **[58, 59]**. The shape of the magnet in the quasi-Halbach array was studied, e.g. triangle, trapezoidal, and T-shape, for the further improvements in self-shielding effect and thrust **[60]**. A tubular quasi-Halbach magnetized linear motor was proposed **[61]** and deeply analysed **[62-64]**, which includes an analytical field expression of the quasi-Halbach magnetized motor **[61, 62]**, comparative studies on multiple magnetization structures **[63]** and design optimization **[64]**. Ibrahim et. al **[65]** mounted quasi-Halbach magnetized tubular magnets on non-Ferromagnetic Support Tube, to remove the back-iron completely. Although mover mass was reduced significantly,

incomplete self-shielding on the back-iron side still remained a problem. Luo et al. **[66]** studied the influences of the mover gaps on the motor thrust and magnetic flux density with an analytical model.

A number of studies have demonstrated that moving-magnet linear motors can offer higher efficiencies than moving-coil linear motors **[67, 68]**. Further, a comparison between moving-coil and moving-magnet linear motors has indicated that the volume of magnet required for a moving-coil is greater than for a moving-magnet linear motors of the same power **[21, 69]**. In addition, the absence of flying leads to the armature makes moving-magnet linear motors more reliable and rugged, making them more suitable for higher duty operation **[70]**.

1.2.3 Moving Coil Linear Motors

A moving-coil linear motor comprises a stationary permanent magnet, either radially or axially magnetised in the stator and a moving-coil armature. Moving coil configuration requires much more magnet volume than a moving magnet configuration. Since magnets are the costliest component of most linear motors, moving coil configurations are only appropriate for cost insensitive applications, e.g., space cryocoolers. Moving coil linear motor has already been extensively used in long-life space cryocooler for about three decades **[71-73]**. However, very limited applications in domestic refrigeration systems have been reported.

Clark **[69]** complied multiple generic configurations of moving coil linear motors. With rare-earth magnets, topologies shown in Fig. 1.16 were used for applications which require high thrust force. It was pointed out that high coercivity and energy magnets were conducive to a high magnetic loading, which reduces the electrical loading, while at the same time reducing the volume of copper, which may reduce the moving mass **[51]**.

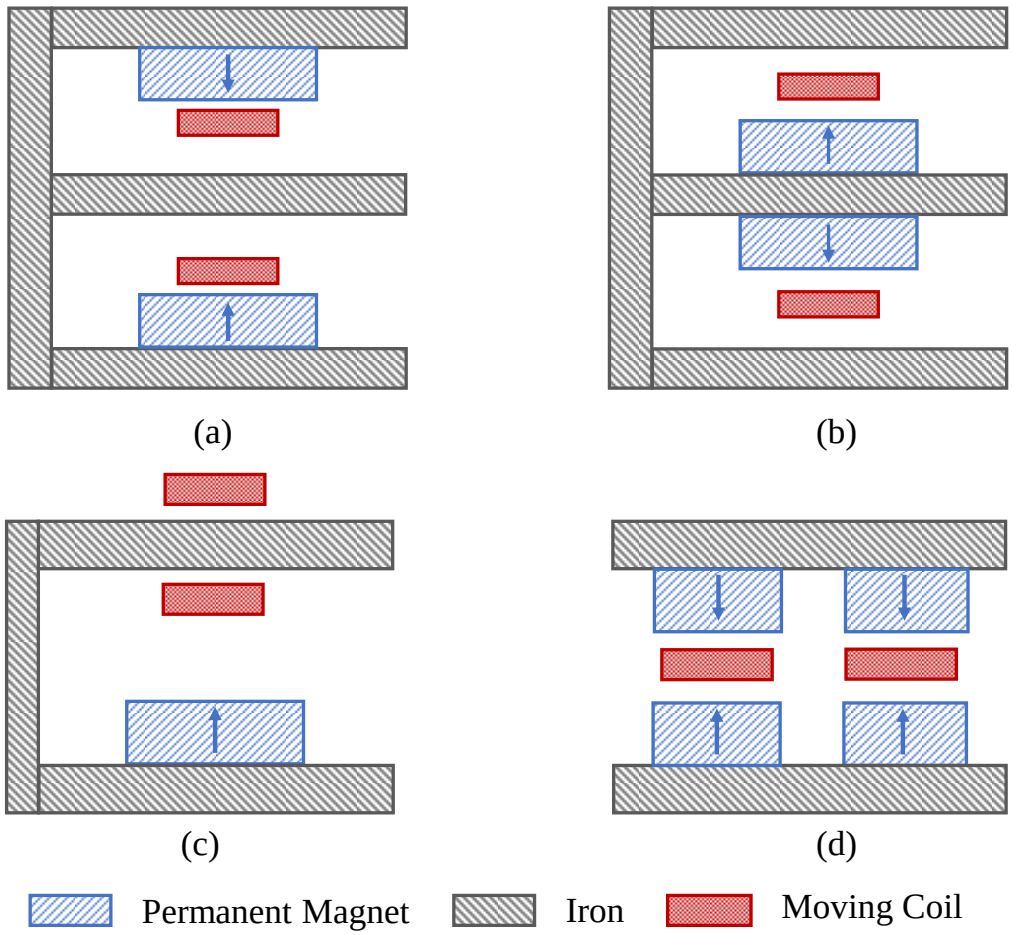

Fig. 1.16 Moving coil linear motor topologies **[69]**

Studies of moving coil linear motor focused on approaches to increase specific force capability were carried out. Comparative studies on tubular moving coil linear motor showed that axially magnetized designs have a higher specific thrust force capability than radically magnetized topologies at the expenses of more magnet volume **[74]**. Further improvement of the design was proposed **[75]**. Both the magnets and the associated pole-pieces are annular shaped and supported on a non-ferromagnetic rod to achieve higher specific force capability. Lee et al. **[76]** employed multi-segmented trapezoidal (MST) magnet arrays in a planner moving coil linear motor. Compared with the one with rectangular magnets, the design with proposed MST showed a higher specific force capability.

Moving coil linear motor has been widely used in Stirling-type pulse tube cryocoolers. It was reported that NGAS (Northrop Grumman Aerospace Systems) developed more than

sixteen space Stirling-type pulse tube cryocoolers, all of which are driven by moving-coil linear compressors **[77, 78]**. Two of them had already continuously operating in orbit for more than 15 years. Dang et al. **[72]** developed moving coil linear compressor for Stirling-type pulse tube cryocooler applications. The moving coil linear motor is shown in Fig. 1.17, the moving coil oscillates backwards and forwards within the air gap between the two return irons and permanent magnets. A micro moving coil linear motor was designed and developed for a linear compressor operating at 90–140 Hz, a three-dimensional theoretical model was built and experiments were conducted for validation. An average motor efficiency of 78.6% was achieved according to experimental results.

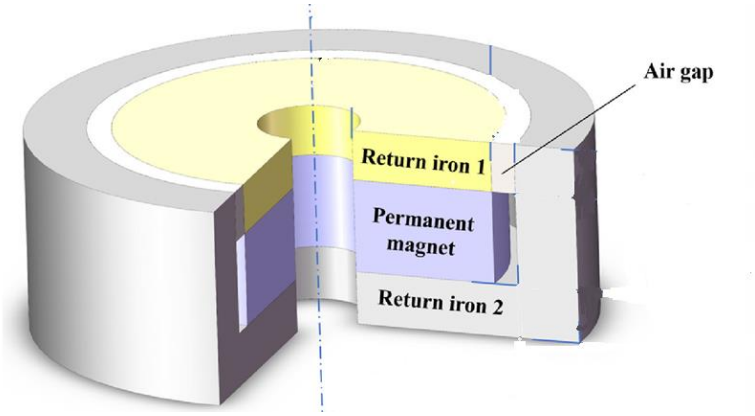

Fig. 1.17 Moving coil linear motor for a Stirling-type pulse tube cryocooler **[72]**

The disadvantages of moving coil linear motors were summarized **[51]** as below:

(1) Fragility of the connections and flying leads;

(2) Difficulty in heat dissipating from the coils;

(3) Limited access to moving coil;

(4) Limited stroke and thrust force capability;

(5) Coil winding burn out due to coil rubbing against the iron **[79]**

Based on the foregoing, a moving coil linear motor was not preferred for a for a low power refrigerator compressor system.

1.2.4 Moving Iron Linear Motors

A moving iron linear motor is composed of stator coils, stationary magnets and moving iron. Axial movement was generated based on magnetic reluctance principle in a moving iron linear motor. With moving iron reciprocating forwards and backwards, a flux linkage reversal occurs.

Boldea et al. **[80]** pointed out that both moving coil and moving magnet designs suffered from limited mover thermal capacity and mover fragility. A moving iron configuration was introduced **[80, 81]** as shown in Fig. 1.14 a. A moving iron design with two springs was introduced by Lequesne **[82]**. When the plunger was at one side, one of the springs was released while the other was compressed. The introduced design showed bad energy conversion performance. A key characteristic of the motor is that the part of energy needed for oscillation was stored in the springs. This also means the moving velocity was affected by the spring-mass system to some extent. The optimized moving iron linear motor design is shown in Fig. 13b.

Evan et al. **[83]** presented a tubular moving iron linear motor that can be employed for multi-purpose applications. The motor employed axially magnetised NdFeB magnets. Ibrahim et al. **[49]** further optimized the design using finite element analysis (FEA) method with respect to the depth, width of armature and the ratio of outer radius of armature to that of stator, for the application in reciprocating compressors.

Li. et al. **[84]** proposed a novel transversal-flux linear motor, with auxiliary low-cost radially magnetized ferrite magnets and additional back iron as shown in Fig. 1.18b. This design was evolved from an early moving iron linear motor proposed in **[80]** as shown in Fig. 1.18a. It was reported that, the evolved design showed much lower material costs and improved material utilization while achieving nearly the same performance without noticeable increase of fabrication cost. Therefore, the evolved design is more appropriate for applications in refrigeration compressors which requires high thrust density and low

cost.

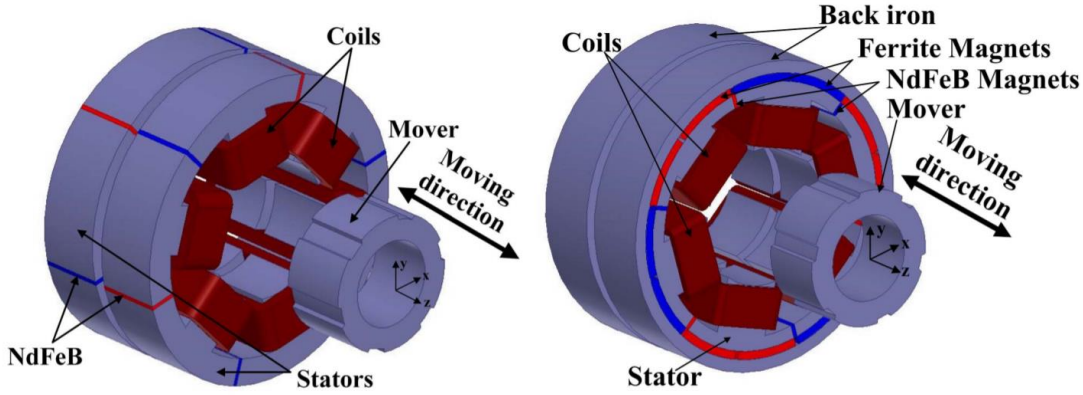

Fig. 1.18 Transversal-flux moving iron linear motor topologies **[84]** (a) original design (b) evolved design

However, even though moving iron linear motor topologies have some desired merits, such as low fabrication complexity and high structural robustness **[84]**, they tend to suffer from some disadvantages which restricts their application **[63]**:

(1) Heavy moving mass, which makes them too heavy for high-frequency actuation;

(2) A relatively low force capability due to low air-gap flux density, which also means high consumption of rare-earth magnetic material to achieve the same output with other topologies.

Based on the foregoing, moving iron topologies were not considered to be suitable candidates for use in low power linear reciprocating for vapour compressor systems.

1.3 Sensor-less Detection Techniques for Electric Machines

1.3.1 Sensor-less Control of Rotary Machines

Due to the facts that position sensors require space for installation and easy to fail in harsh environments, sensor-less technology, which means position control technology without using a position sensor, has been studied to improving the reliability of the drive system.

Permanent magnet synchronous motor (PMSM) has been extensively employed in various applications. Shahgholian et al. **[86]** introduced a sensor-less direct torque control technique for permanent magnet synchronous motors with model reference adaptive system. A novel observation and detection technique based on Kalman filter was proposed by Khalid and Nawaz **[87]**. Kalman filter is an algorithm that recursively deals with linear filtering problem for the discrete data by evaluating the non-measurable and measurable states. This filter can provide an estimation of the noisy states. In the research, the Kalman filter predicted the angular speed through taking the measurements of noisy current of the motor. The voltage input was adjusted by the controller to achieving the required change in the motor speed and motor position. It can be concluded that Kalman filter is robust against external disturbances, and is capable of estimating parameters and states that are difficult to measure through physical sensors. Some research have been performed for the sensor-less vector control algorithm of the PMSM **[88-90]** and many algorithms are applied to practical use for high reliability and low cost. There are a great variety of rotor speed estimation techniques in the literature. They can be classified into two main categories: (a) signal injection method and (b) state-observer methods. The first category suffers from computational complexity and the requirement of external hardware for signal injection. Those in the second category are based on mathematical models of the IM and are simple and robust against disturbances **[91]**. These techniques include open-loop estimators, the Kalman filter, the Luenberger observer, and Model Reference Adaptive System **[92, 93]**. Fukumoto et al. proposed the position sensor-less vector control method using an armature current flux adaptive observer **[88, 94]** The proposed method consists of an adaptive observer, a position error estimator, and a position and speed estimator. The performance of the position sensor-less vector control method was further improved by online motor parameter error compensation and the practical dead-time compensation.

Although the control of rotary motors is not exactly the same as linear motors, large similarities exist between two types of motors. The research on the sensor-less control of

rotary motors can provide guidance for the development of sensor-less control of linear motors.

1.3.2 Sensor-less Stroke Detection Techniques for Linear Machines

Piston stroke can be varied to modulate cooling capacity in a linear compressor. Top dead centre, which is determined by piston stroke and piston offset can also be controlled to avoid collision with cylinder head. Advancements in digital electronics and improvements in the hardware performance of controllers have given rise to many sensor-less observations of the piston position in free-piston machines. Sensor-less detection is a technique of using a model of the motor's behaviour of the compressor as a linear position sensor for the piston displacement estimation. Compared to the systems with separate position sensor, sensor-less detection has the merits of simplicity, lower cost, and robustness **[95]**. Different from a rotary compressor in which piston stroke is constrained and defined by the diameter of crankshaft, linear compressor is a free piston machine which allows the stroke to be variable. This facilitates the modulation of the compressor output. It also means that gas force, motor force and mechanical spring force are free to affect the piston's motion, which adds complexity in the stroke control of a linear compressor. Piston may collide into cylinder head without accurate knowledge of piston position, which demonstrates another reason why piston position sensing and control is critical. In most cases, closed loop stroke control was achieved with commercial displacement sensors, e.g. Hall Effect position sensor. However, using an extra displacement sensor raises some concerns about the seal fabrication complexity, and cost of a linear compressor. Extreme environment in a linear compressor for household refrigerator, i.e. refrigerant and oil, it is not cost-efficient to install a delicate sensor inside the compressor. The shell is hermetically sealed and if a sensor is to be used, at least two additional wires are required to penetrate the shell, which may not be acceptable in production **[96]**. Therefore, it is of vital importance to develop sensor-less piston position detection techniques.

An approach to estimate piston displacement is to integrate back emf (electromotive force) of the linear motor with measured current and voltage **[97]**:

$$x = \frac{1}{\alpha}\int (v(t) - L\frac{di(t)}{dt} - R\, i(t))dt \tag{1.1}$$

where x is piston displacement, α is the motor constant (the ratio of motor force over current), L is self-inductance, R is coil resistance, v and i represents voltage and current as a function of time t.

A key problem involved in the integration is unavoidable biases/DC offset in the measured voltage and current. In order to solve this problem, some algorithms have been proposed in **[98-101]**. Xu and Novotny **[98]** mentioned that one way to avoid using a shaft sensor is to estimate flux, which can be either rotor flux, air gap flux, or stator flux, directly from voltage and current measurements. A direct stator flux orientation system was presented, parameter identification, flux estimation, and rotor speed estimation are incorporated in the implementation. Hu and Wu **[99]** proposed an algorithm that can compensate the flux automatically using adaptive control to eliminate DC offset. In **[100]**, a software programmable cascaded low-pass filter has been investigated for flux vector synthesis of a stator flux-oriented direct vector-controlled induction motor drive. The integrator has been studied in detail with the drive system in wide frequency range by simulation and performance was found to be excellent. These algorithms have their own weaknesses in the piston stroke detection due to requirement of complex calculation **[98, 99]** and an unneglectable time delay in the results **[100]**. In **[102]**, the integrated velocity signal was passed through a high-pass filter capable of DC bias removal to avoid this problem. However, the accuracy was influenced by the inverter frequency. Efforts in this area also include sensor-less stroke detection methods based on systematic modelling of linear compressor **[103-106]**. Zhang et al. **[103]** built an equivalent mathematical model of a linear motor to express mover position. A maximum steady-state error of 0.45 mm was shown between estimated strokes and experimental results. Tang et al. **[104]** presented a stroke estimation method based on energy method. The estimated stroke

results are verified with the measured stroke, and the errors would be achieved within 5%. Latham et al. **[105, 106]** proposed a novel system level controller to simultaneously achieve resonance tracking and stroke control objectives utilizing a pair of nonlinear observers to obtain the necessary information as shown in Fig. 1.19. Top dead centre position was estimated with observed velocity and acceleration signals. For most of the methods mentioned above, mechanical model that describes acting forces and piston dynamics and electrical model that describes the electromagnetic behaviour were coupled, which means complex model and parameters identification are required.

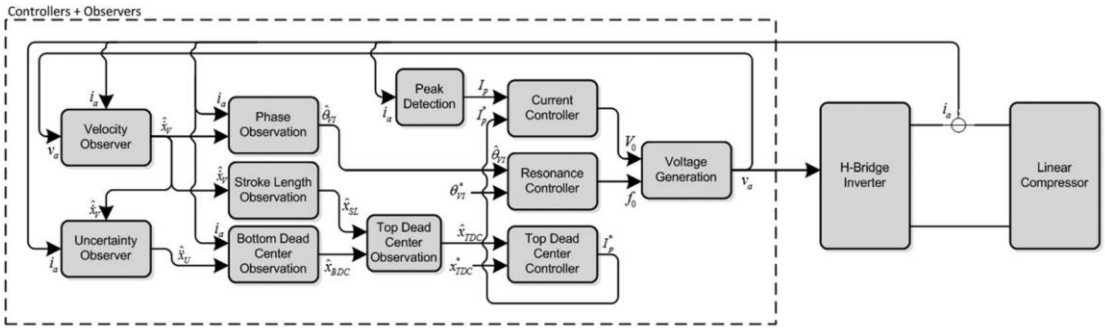

Fig. 1.19 Observers and controllers for the sensor-less control of linear compressor **[105]**

One major problem remains in these two categories of sensor-less control is that parameters were taken as constant during parameters identification process. Influence of parameters fluctuation such as force constant, equivalent inductance on the stroke estimation were reported **[101]**. Sung et al. **[107]** identified motor parameters as a function of the motor current and piston position. The identified parameters were stored in a Read Only Memory (ROM) table and were used later for the stroke sensing. However, the parameters identification is time-consuming to achieve desired accuracy.

Based on the foregoing, existing sensor-less stroke detection have their own limits and weakness. Developing a low-cost, simple and robust sensor-less stroke detection technique facilitates the commercialization of linear compressor and also extends the applications of linear compressor into systems of smaller size.

1.4 A Novel Moving Magnet Linear Compressor for Refrigeration

1.4.1 Linear Compressor Configuration

A prototype moving magnet linear compressor was developed initially for computer cooling **[108]** as shown in Fig. 1.20, which can also be adopted for domestic refrigerators. The compressor consists of a moving magnet linear motor, the piston-cylinder assembly and a flexure spring suspension system. The linear compressor has a maximum stroke of 14 mm, piston diameter of 19 mm, axially length of 31 mm, and maximum shaft power output of 100 W. A radical clearance of 10 μm exists between the piston and cylinder wall to reduce frictional loss, avoid wear and ensure low gas leakage loss from the cylinder side to the motor side. A rectangular non-ferromagnetic tube was positioned within the gap between magnets and cores to enclose the moving magnet assembly, and thereby achieving pressure containment. The piston is directly coupled with the moving magnet assembly and the cylinder is fixed on the right side of the linear motor as shown in Fig. 1.20.

The suspension system includes two sets of flexure springs which allow axial movements, but have high radial stiffness and therefore restricting radial movement. Axial spring stiffness is 16.3 kN/mm. The two spring assemblies are attached to the ends of the compressor body. A beam contained in the rectangular tube makes the inner connection between the two spring assemblies, which also houses the magnets.

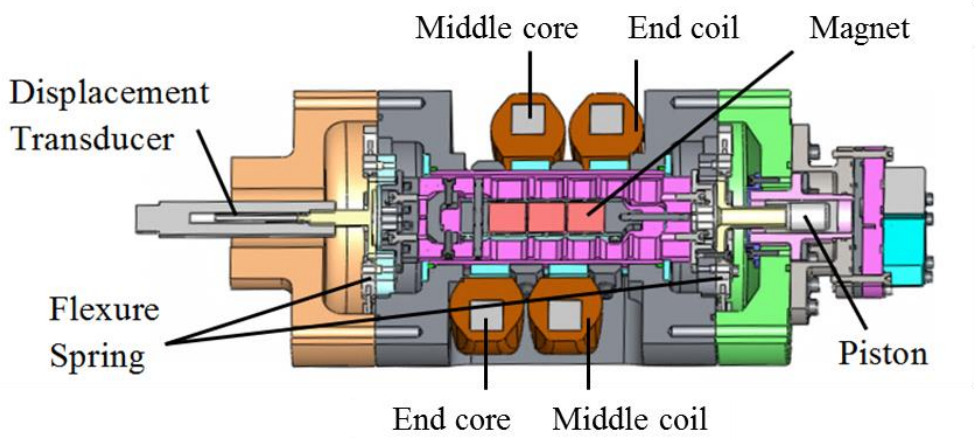

(a)

(b)

Fig. 1.20 The configuration of the prototyped moving magnet linear compressor; (a) Cross section of the linear compressor and motor (b) The prototype linear compressor **[109]**

By adding valves, refrigerant can be driven through a refrigeration system, enabling cyclic heat absorption at evaporator to achieve cooling in refrigerators, which is also the major distinction from Stirling and pulse tube cryocoolers. Two reed valves are included in the linear compressor, the low-pressure suction valve at inlet and the high-pressure discharge valve at outlet. The two reed valves for this linear compressor are mounted on a circular valve-plate and face the top of the piston.

1.4.2 Linear Motor Design

The linear motor consists of three evenly spaced rectangular moving magnets and four laminated cores wounded around with a number turns of coils as shown in Fig. 1.21. Transverse flux paths exist between the moving part and the static part. The static part of the motor is composed of laminated cores and windings. The slotted cores are positioned and evenly spaced. Air gap is defined between the slotted core and magnets. All the cores and magnets are aligned along the motor axis. Neighbouring cores are positioned at opposite sides

of the axial axis so that the coils do not obstruct each other. Three rectangular NdFeB (alloy of neodymium, iron and boron) magnets arranged along axial axis were included in the moving part, and magnets were positioned within the air gap defined by the static assembly. The polarisation of the magnets alternates and is arranged so as to induce fields that circulate around the adjacent cores. The magnet assembly in particular is very simple and robust, but nonetheless, the magnet utilisation is good, the moving mass is low, and high efficiencies are readily attained. The slotting of cores forms an air gap where magnets are placed. Two adjacent cores are arranged on the different side of the magnets. The two cores on the same side, wound with the concentrated windings, are axially aligned. Coils on the one side of magnets are in series, and in parallel with coils on the other side. Table 1.1 gives the design configuration of the linear motor.

When direct current is supplied into the motor, opposite polarity poles are shown along the axial direction. Three permanent magnets are parallelly magnetized with alternating polarity and are uniformly mounted on a non-ferromagnetic beam contained in the rectangular tube. When it works as an oscillatory motor, a single-phase sinusoidal current is fed into the coils from external power circuit. The alternating magnetic field produced by conductors carry currents interacts with the magnetic field created by permanent magnets, and thus producing the shaft force that drives the oscillatory motion of the mover. The linear motor, the flexure spring and the piston construct a resonant system, driving the piston oscillate in the cylinder chamber to compress refrigerant.

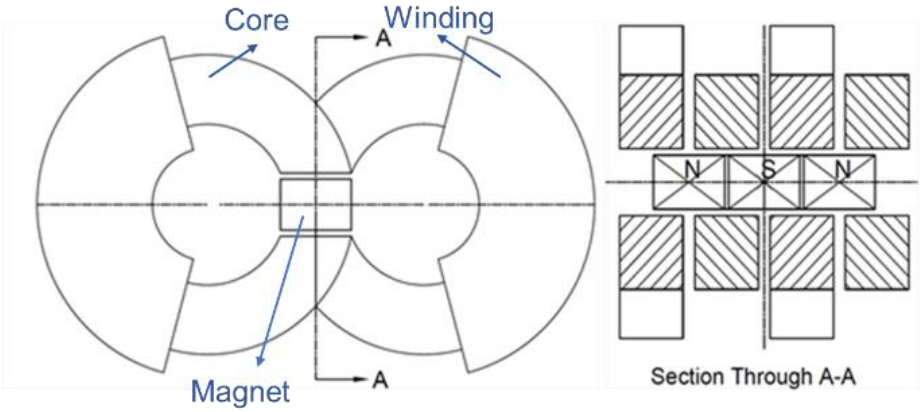

Fig. 1.21 Moving magnet linear motor configuration

Table 1.1 Linear motor design configuration

Total mass of moving assembly (kg)	0.66
Magnet material	NdFeB
Number of magnets	3
Dimension for each magnet (mm)	18×18×12.7
Number of cores	4
Number of turns for each coil	620
Resistance of total motor coil (Ω)	3.5
Maximum stroke (mm)	14

1.5 Research Objectives

The free piston in a linear compressor allows achieving cooling capacity modulation via adjusting piston stroke. Although it makes cooling capacity modulation more flexible than conventional compressors, it makes the control of a linear compressor more difficult. Piston position sensing is vital for both safety consideration and piston stroke control. Using piston position senor inevitably increases the cost. The installation of a piston position sensor demands some space on the other hand, which is not desirable for a compact design. The main aims of this work are to investigate the characteristics of a

novel moving magnet linear motor for linear refrigeration compressor and to develop novel sensor-less stroke detection techniques for the linear compressor.

This study targets the following objectives in order to achieve the above mentioned aims:

- Providing a FEA (Finite Element Analysis) model of the linear motor for the analysis of the characteristics of the linear motor.
- Performing well-designed experiments on an instrumented linear refrigeration compressor with various axial clearance volumes, and evaluating the system performance with clearance operation scheme.
- Collecting sufficient data including motor inputs (current, voltage) and piston stroke of the compressor, and building a machine learning model to achieving stroke prediction.
- Developing a stroke detection technique that is based on a physical parameter variation related to magnet/piston position, e.g. flux linkage.

1.6 Thesis Structure

The thesis is arranged in following sequence:

(1) In Chapter 1, the research backgrounds and research objectives of the thesis are presented, in which a comprehensive literature review is included.

(2) In Chapter 2, a test rig built for the evaluation of system performance and data collection for the investigation of motor/compressor performance, and the development of sensor-less stroke detection techniques is introduced.

(3) In Chapter 3, the characteristics of the linear motor are investigated with FEA method . Both magneto-static and transient solvers were employed for simulations. Simulation results were compared with results from measurements..

(4) In Chapter 4, a number of tests were conducted with small axial clearance operation to investigate how minimizing clearance volume affects system performance. The refrigeration performance of the linear compressor using R1234yf among using various clearance volumes and using an offset of 0 mm were compared with a fixed condenser outlet temperature.

(5) In chapter 5, sensor-less stroke detection using ANN (artificial neural network) is investigated to achieve active axial clearance control. A number of experimental tests were conducted in the rig to sample and record voltage, current and displacement.

(6) In Chapter 6, a novel stroke detection technique using low-cost inductive coil wound around a core is presented. A magnetic equivalent circuit (MEC) model is introduced for flux linkage prediction.

(7) In Chapter 7, the conclusions of the research and future work are presented.

Chapter 2 Instrumentation of the Linear Refrigeration Compressor

2.1 Test Rig Configuration

An experimental test facility was developed to investigate the oil-free linear compressor performance, and to carry out measurements for developing and validating sensor-less stroke detection techniques. The schematic of the test rig and associated instrumentation for the linear compressor experiments are shown in Fig. 2.1. The facility is a vapour compressor refrigeration system which consists of a linear compressor, a condenser and an evaporator with an electric heater and a throttling/expansion valve installed between the condenser and evaporator, which was used for pressure ratio adjustment. Various working fluids, e.g. nitrogen, helium, R134a and R1234yf can be used in the test rig.

The red line in Fig. 2.1 shows the power flow, which includes the main power supply for the linear compressor and the power supply for the bleed flow loop, in which the solenoid valve was electrically driven to achieve mean piston position adjustment. For the main power flow, voltage signals generated through the output channel of the NI (National Instrument) USB-6341 Multifunction I/O (Input/Output) device were amplified by a power amplifier before being applied to the linear compressor. The drive frequency was adjusted manually so that the resonance can be identified and applied to the linear motor, while the amplitude of the voltage signal determines the stroke of the piston.

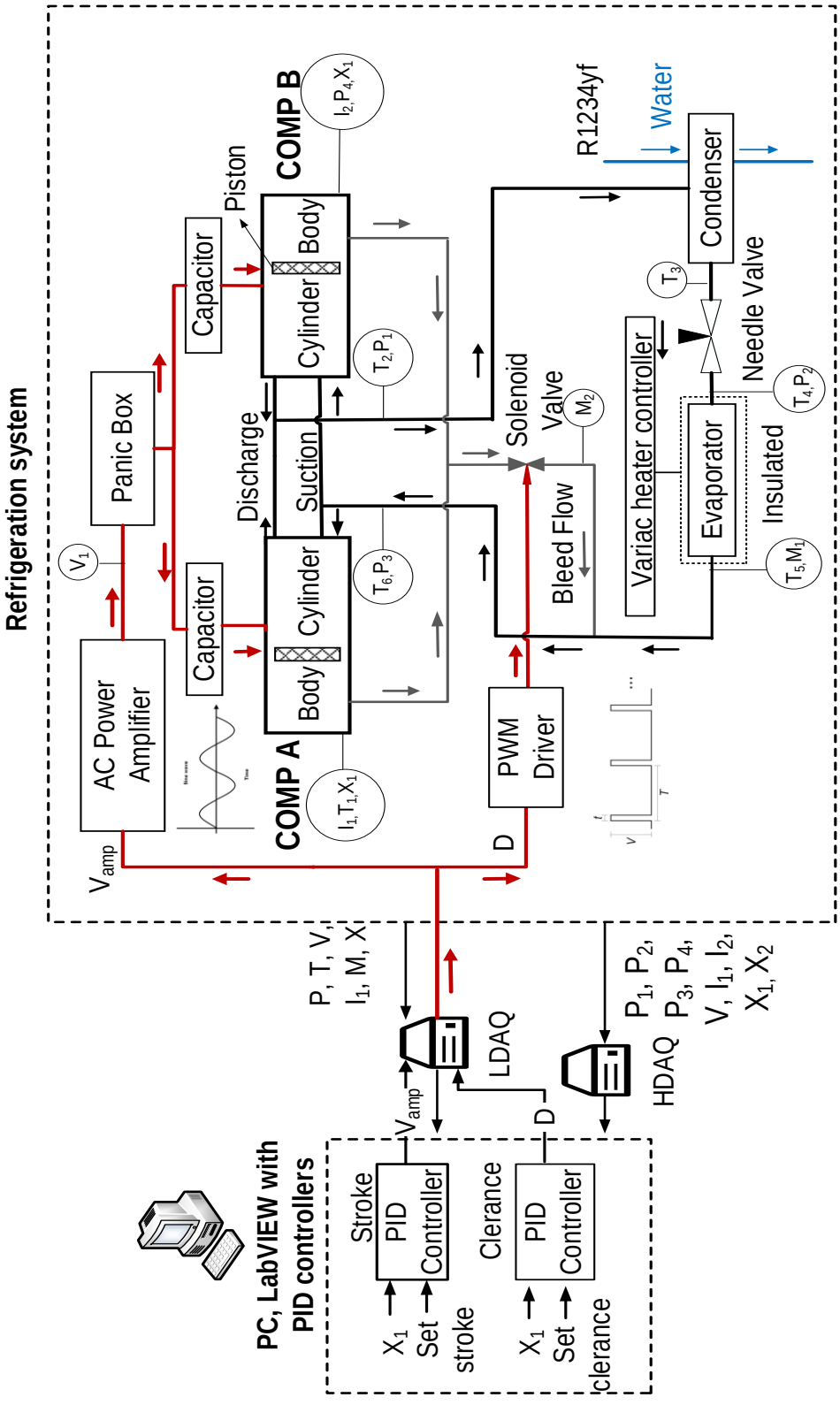

Fig. 2.1 Schematic of the test rig of the linear compressor in the refrigeration system and instrumentation (P: pressure transducer, T: thermocouple, M: mass flow meter, V: voltage sensor, I: current transducer, X: linear variable differential transducer, D: duty cycle)

Apart from the main flow loop, between the compressor discharge port and suction port of the linear compressor, a bleed flow loop which connects the compressor body side to the suction line of the main flow loop was developed. The bleed flow loop consists of a solenoid valve, a refrigerant return line, and a proportional-integral-derivative (PID) controller. The refrigerant flows from the compressor body to the suction to keep the mean piston position at datum. A PWM (Pulse Width Modulation) signal was generated to drive the solenoid valve. The duty cycle of the digital pulse signal determined the fraction of time that solenoid valve was open. A 12 V power supplier was used to drive the solenoid valve.

Three oscilloscopes were used, one for monitoring the current and voltage of the linear compressor, one to display displacement signals from two LVDTs and the other for the visualization of outputted sinusoidal voltage and duty cycle of solenoid valve. The complete experimental apparatus is shown in Fig. 2.2.

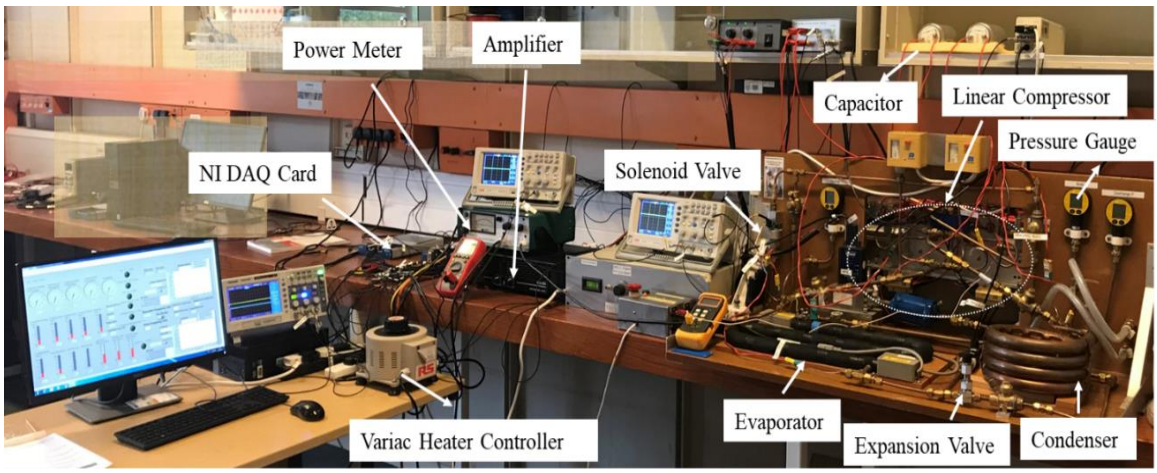

Fig. 2.2 Complete experimental apparatus for the oil-free linear compressor

2.2 VCR System Components

Table 2.1 gives the specification of key components of the VCR system. Two linear compressors were mounted back-to-back with shared discharge and suction lines to deliver hot and pressurized refrigerant gas. Delivered refrigerant releases heat and absorbs heat to achieve phase transition from an off-the-shelf water-cooled coaxial condenser (as

shown in Fig. 2.3) to an annular evaporator with an electric heater in the middle respectively. The evaporator was covered by insulation to prevent the heat transfer from the evaporator to ambient. A variac was used to adjust the heating load of the electric heater to allow the refrigerant fully evaporated to achieve the maximum cooling capacity. Fig. 2.4 shows the annular evaporator with an electric heater in the middle.

Table 2.1 Specification of the key components for the VCR system

Components	Specifications
Compressor	Two identical oil-free linear compressors working in opposite to reduce vibration, piston diameter of 19 mm, maximum compressor stroke of 14 mm, rated power of 100 W for each
Condenser	Coaxial water-cooled, copper, off-the-shelf, coolant connection diameter of 12.7 mm, refrigerant connection diameter of 16 mm
Evaporator	Copper, electric heater (resistance of 50 Ω), length of 128 cm, inner diameter of 7.9 mm, outer diameter of 12.7 mm
Expansion valve	Needle valve, stainless steel medium flow high pressure

Fig. 2.3 Water-cooled coaxial condenser

Fig. 2.4 Evaporator with electric heater

2.3 List of Instruments

Two NI I/O multifunction devices with maximum sampling rate of 500 kHz were used to collect real time data for a low-speed data acquisition system (LDAQ) and a high-speed data acquisition system (HDAQ). The NI I/O multifunction device has 16 analogue input channels, 2 analogue output channels and 24 digital channels. A sinusoidal waveform voltage signal and a PWM signal were generated by LabVIEW through an analogue output channel and a digital channel of LDAQ card respectively. The voltage signal was then amplified by an AC power amplifier to drive the linear motor.

Two linear variable differential transformers (LVDTs) were used to measure the piston positions of two linear compressors, each along with an ATA-101 analogue transducer amplifier and an ATC-101 analogue transducer controller. Both LVDTs were calibrated to obtain the sensitivity factor. Table 2.2 lists the main instruments for the test rig.

Table 2.2 List of instruments for the measurements of the linear compressor

Instruments	Model	Quantity	Accuracy (percentage related to full scale)
Multifunction I/O Device	NI USB-6341	2	N/A
Current transducer	LA LEM 25-NP	2	± 0.5 %
Voltage attenuator	Fylde 261HVA HV	1	± 0.5 %
Isolation amplifier	Fylde 4600A	1	± 0.5 %
LVDT	Lucas Schaevitz	2	± 0.025 mm
LVDT signal conditioner	ATA-101	2	N/A
Pressure transducer	DRUCK PMP1400	4	±0.15 %
AC power amplifier	Vonyx VXA-2000	1	Signal to noise ratio >90 dB
Thermocouple	K-type	8	± 1.5 °C
Main mass flow meter	Hastings HFM-201	1	± 1 %
Bleed flow meter	Tylan FM-360	1	± 1 %
Power meter (heater)	Electronic Wattmeter EW604	1	< 2.5% (50Hz, unity power factor, 25 °C)
Oscilloscope	RS Pro IDS1000 Series IDS1072AU	3	N/A
Capacitor	EPCOS B32361	2	± 5 %

Electrical output produced by an LVDT is proportional to the displacement of a separate free-moving core. It is composed of a primary coil and two secondary coils symmetrically spaced on a cylindrical form as shown in Fig. 2.5. A moveable magnetic core in a rod shape provides a path for the magnetic flux that links the coils to flow through. When the primary coil is supplied with an external AC source, voltages are generated across the two

secondary coils. Secondary coils are wired in series opposing to make the polarities of two voltages opposite. Therefore, the electrical output of the transducer is the difference between two induced voltages, which is zero when the magnetic core is at the central position. When the core is moved from the central position, the generated voltage across the coil toward which the core is moved rises, while the voltage in the other coil reduces. A differential voltage output that shows linear variation with the change in core position is produced. The phase of this output voltage changes abruptly by 180 degrees as the core is moved from one side of central position to the other.

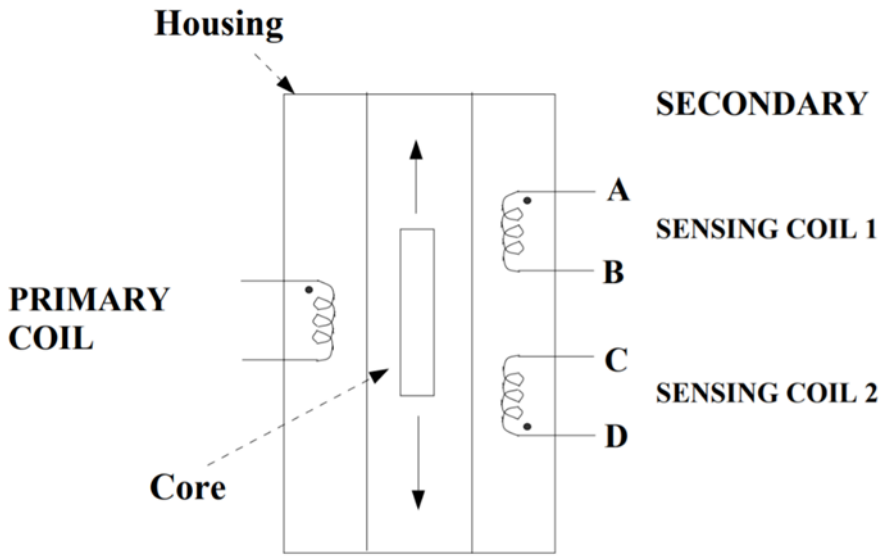

Fig. 2.5 Schematic of a Lucas-Schaevitz LVDT Transducer **[110]**

Mass flow meters were used to measure mass flow rates in both the main and bleed flow loops (Hastings HFM-201 for the main flow and Tylan FM-360 for the bleed flow). The output voltage of the mass flow meters ranges from 0 to 5 V. As mass flow meters are thermal-type and sensible to thermal properties, calibrations were conducted for different refrigerants. The gas calibration factor for the two mass flow meters were calculated according to MKS Instruments **[111, 112]** and Hastings Instruments **[113]**.

Two capacitors were employed for the power factor correction, which reduced the voltage required to power the linear compressor. Fig. 2.6 shows the electric circuit of the linear motor. When it is operated at resonant frequency, the voltage of the impedance associated

with motor force will be in phase with current as displacement leads current 90°, so the circuit then becomes a typical RLC (Resistor, inductor, and capacitor) circuit.

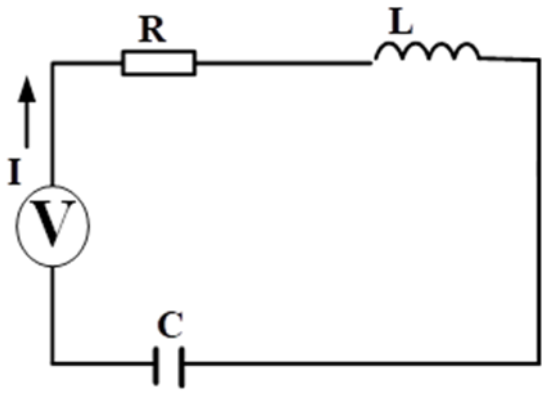

Fig. 2.6 Electric circuit diagram of the linear motor

2.3 LabVIEW and Control System

2.3.1 LabVIEW and Data Logging System

The National Instruments LabVIEW is a graphical programming software which is used to communicate with the data acquisition card, as well as to process and display the data, and to record the sampled data. VI (virtual instrument) is the basic building block of graphical programming. A VI includes three main parts, front panel for user to interacts with the VI, block diagram containing the source code, and connector that enables the connection between a VI to the other VIs. For the purpose of implementing stroke and piston offset control, facilitating experimental data recording and key parameters monitoring, a robust software setup was developed in the LabVIEW. Fig. 2.7 shows a screenshot for the front panel of the complete LabVIEW programme.

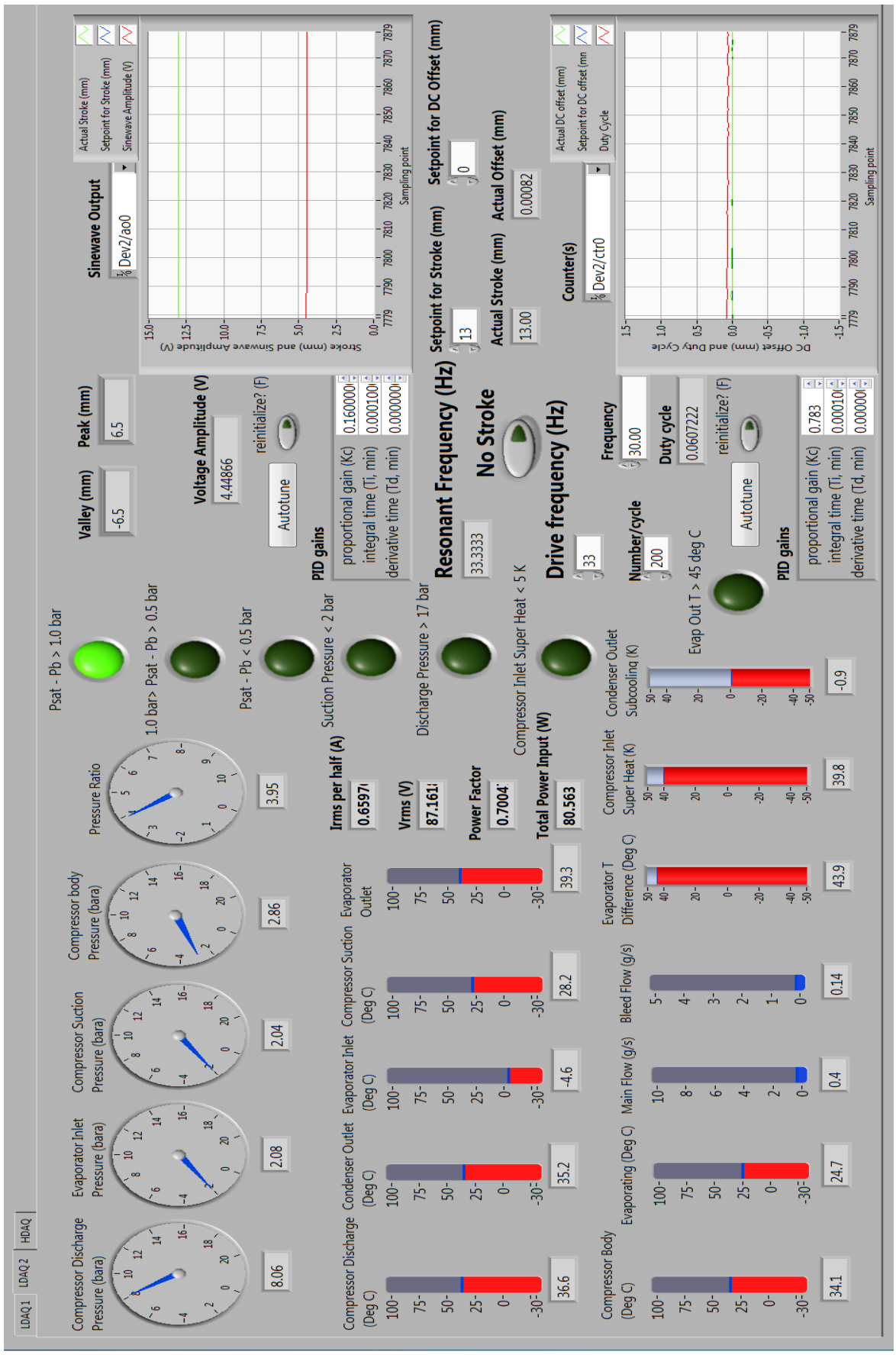

Fig. 2.7 Screenshot for the front panel of the complete LabVIEW programme

LabVIEW-based data acquisition (DAQ) has been employed extensively to acquire data from various sensors (e.g. pressure, temperature, current) installed on a rig. Acquired data are then usually filtered and/or processed before being displayed and/or recorded for further analysis. A data acquisition system includes various types of sensors, DAQ Device and a computer with DAQ software. Each sensor, converts a physical phenomenon (e.g., pressure or temperature), into a measurable electrical signal. The signal is then passed through a DAQ device which works as the interface between a computer and analogue signals via digitizing them to be computer readable. Figure 2.8 shows the flow path of a signal in a LabVIEW-based data acquisition system.

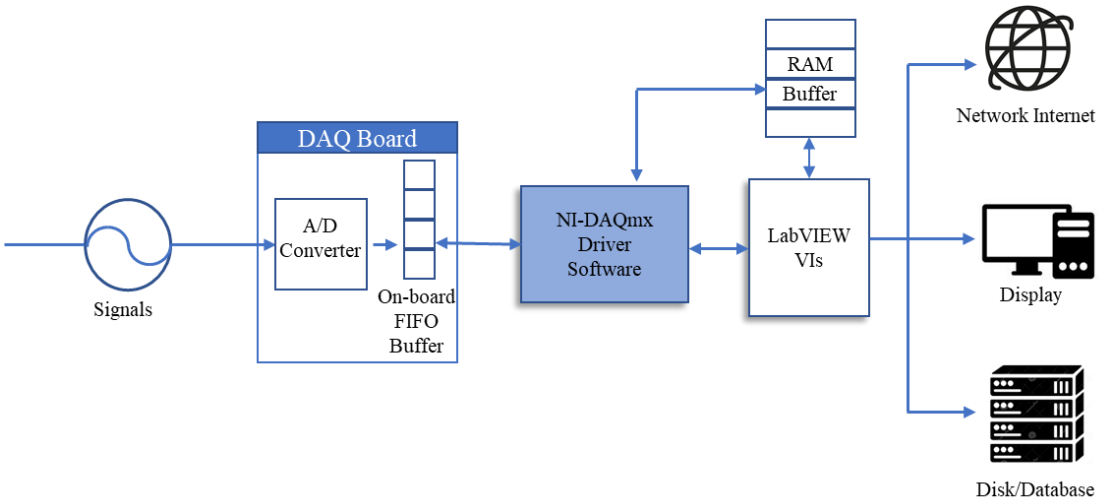

Fig. 2.8 The path of a signal in a LabVIEW DAQ application

The data acquisition systems for the linear compressor measurements consists of a low-speed DAQ (LDAQ) system and a high-speed DAQ (HDAQ) system. Two NI USB-6341 data acquisition cards with 16 analogue input channels and 2 analogue output channels are employed in the LDAQ and HDAQ systems as shown in Fig. 2.9. The maximum sampling rate of each channel is up to 50 kHz with a resolution of 16 bits.

Fig. 2.9 NI USB-6341 I/O multifunction devices

The LDAQ display the parameters that do not change much over cycles for each test condition. Table 2.3 gives the parameters collected from the LDAQ system and HDAQ system. The sensors in the LDAQ system include 6 thermocouples, 4 pressure transducers, and 2 mass flow meters, used for relatively stable parameters measurements. The raw data from measurements were converted to actual values with the corresponding calibration factors in the LabVIEW program. The sampling rate of the LDAQ system was set to be 2 kHz. The data acquired through the HDAQ system includes the current of each linear compressor, the voltage across the linear compressors, and piston displacements measured by LVDTs of each linear compressor, all of which were sinusoidal signals. The default sampling rate of the HDAQ system was 5 kHz. Data recording can be easily completed with the LabVIEW program and corresponding data files were saved to predefined directories.

Table 2.3 Parameters for the LDAQ system and HDAQ system

	Parameters
LDAQ	Pressures (suction, discharge, body, evaporator inlet), temperatures (suction, discharge, condenser, evaporator inlet/outlet, body), mass flow rates (main flow, bleed flow)
HDAQ	Currents and piston displacements of each linear compressor, voltage across the two compressors in parallel

2.3.2 Stroke Control

Stroke is not pre-constrained in the linear compressor as the piston is free. A LabVIEW-based stroke control system was developed for the active control of piston stroke. Fig. 2.10 shows the control block diagram of the linear compressor. The stroke to be operated with can be set in the LabVIEW front panel. With measured actual displacement by the LVDT, the actual stroke was given by the peak-to-peak displacement. A PID controller was implemented in LabVIEW for the stroke control. The output of the PID controller is the amplitude of voltage that was generated though an analogue output channel of the NI I/O device (USB-6341). The amplitude of voltage determined by the auto-tuned parameters and the error stroke, i.e., the difference between the set stroke and the actual stroke. The outputted amplitude of voltage was then amplified by an AC amplifier as the amplitude of the output voltage through the output channel is limited within 5 V. The amplified voltage was applied to the linear motor that drove the piston oscillating backwards and forwards.

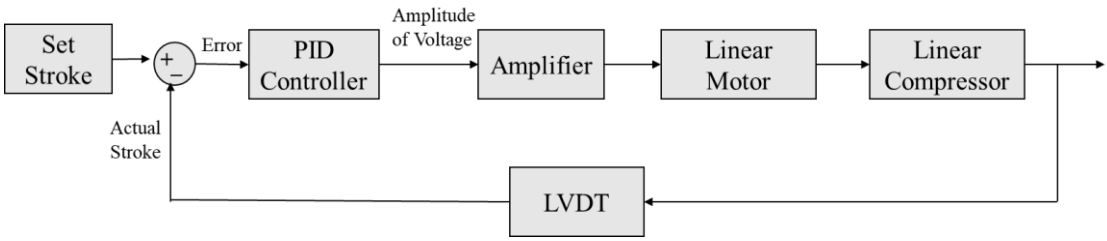

Fig. 2.10 Block diagram of the closed loop stroke control of the linear compressor

The PID control is the most common control algorithm used in industry and has been universally accepted in industrial control. Three basic coefficients are contained in PID algorithm: proportional, integral and derivative, which were auto-tuned in LabVIEW to present an optimal system performance. The proportional term was proportional to the error between the set stroke and the actual stroke given by peak-to-peak displacement measured by LVDT. The integral term was produced through the integration of the stroke error. Derivative term estimated the trend of the stroke error based on the change rate of error.

The process dynamics are complicated and multiple disturbances exist during operation, it is difficult to tune the coefficients of PID controller. An auto-tuning PID VI including the auto tuning Wizard in addition to the basic PID algorithm was used in the closed loop control of the stroke, which automatically evaluated the control system to give optimum coefficients. The principle of auto tuning is to automatically adjust the set point stepwise, and to evaluate the controller parameters from the response of the system. The Ziegler and Nichols method was used in LabVIEW PID Toolkit to determine the PID control parameters. During tuning, the process remains under closed-loop PID control. However, an initial set of PID parameters which produce a stable control of the system was required. Fig. 2.11 show an example of the stroke control with a target stroke of 10 mm using nitrogen as refrigerant. The amplitude of the voltage applied to the linear motors was adjusted to gradually increase the stroke from 0 to 10 mm.

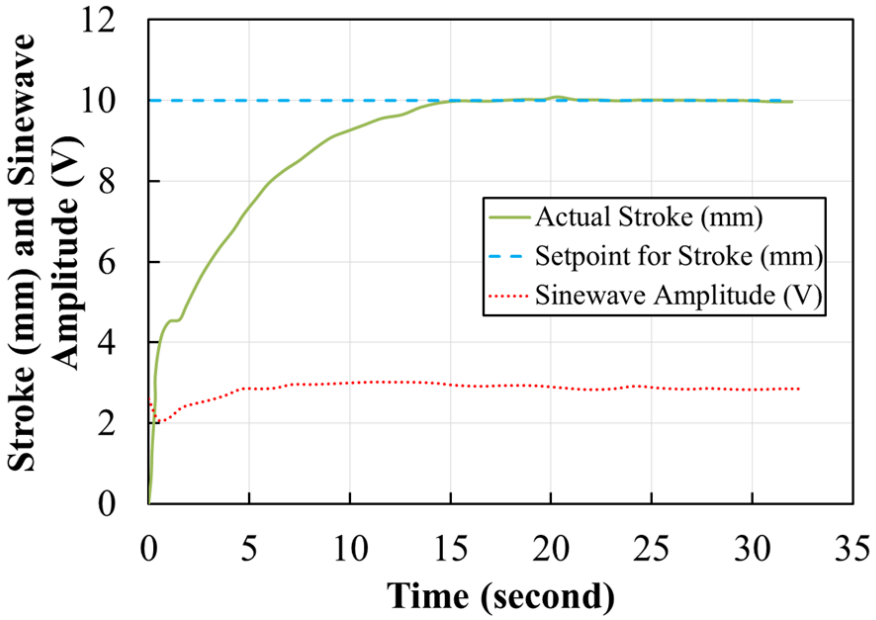

Fig. 2.11 Stroke variations in response to the PID controller with a set point step change from 0 to 10 mm **[5]**

2.3.3 Piston Offset Control

Piston offset refers to the distance between mean oscillating position of piston and the datum central position of the cylinder. Fig. 2.12 shows an example of displacement signal from the LVDT displacement transducer with a stroke of 11 mm and an offset of -0.84 mm. The problem of piston offset is due to the pressure difference generated across a radial clearance seal with a fluctuating pressure on the cylinder side and a constant pressure on the body side. On the body side of the seal, the pressure is relatively stable, whereas the cylinder side of the seal experiences a fluctuating pressure. A bleed flow loop that circulates the refrigerant in the cylinder to the compressor body was introduced before. The main objective of the piston offset control is to adjust the mean oscillating position by adjusting the opening and closing time of the bleed flow loop.

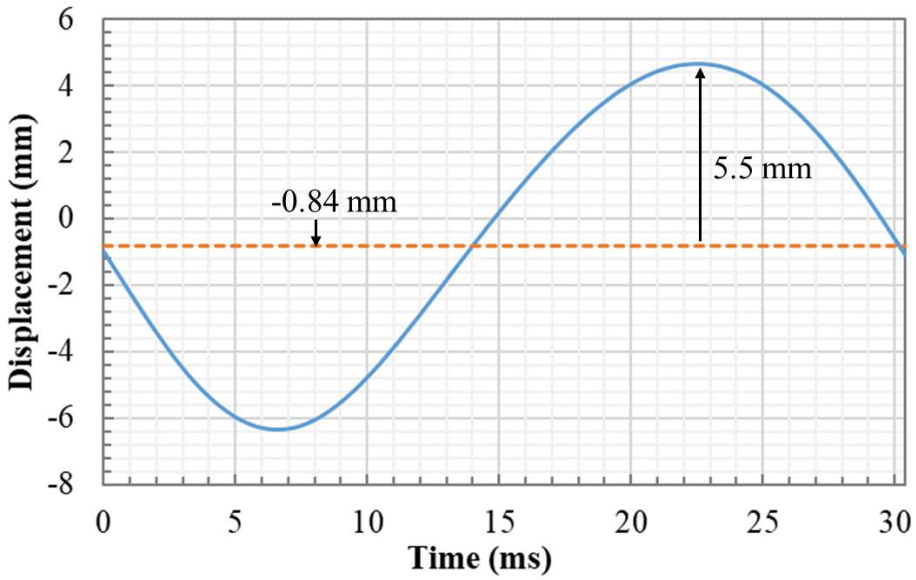

Fig. 2.12 Displacement signal with a stroke of 11 mm and an offset of -0.84 mm

Fig. 2.13 shows the schematic of the closed loop piston offset control system. A solenoid operated fuel injector which was adopted from a gasoline engine was utilized for the bleed gas flow control, so as to eliminate the piston offset or to maintain the mean oscillating piston position at a certain position. The injector was installed in the bleed flow loop in series with the mass flow meter. The two-port solenoid valve was energised by an electrical current through a solenoid to achieve the on and off switch of gas flow, working as the actuator of the piston offset control system. For better illustration of the piston offset, negative displacement is defined as the displacement that is closer to the cylinder head of the compressor. When the stroke is increased, the piston offset tends to be more negative so the solenoid valve needs to be opened for longer time to allow more bleed flow. In contrast, when the stroke is decreased, the bleed valve needs to be closed because the body pressure will be less than the mean working pressure, which tends to move the piston toward the body side.

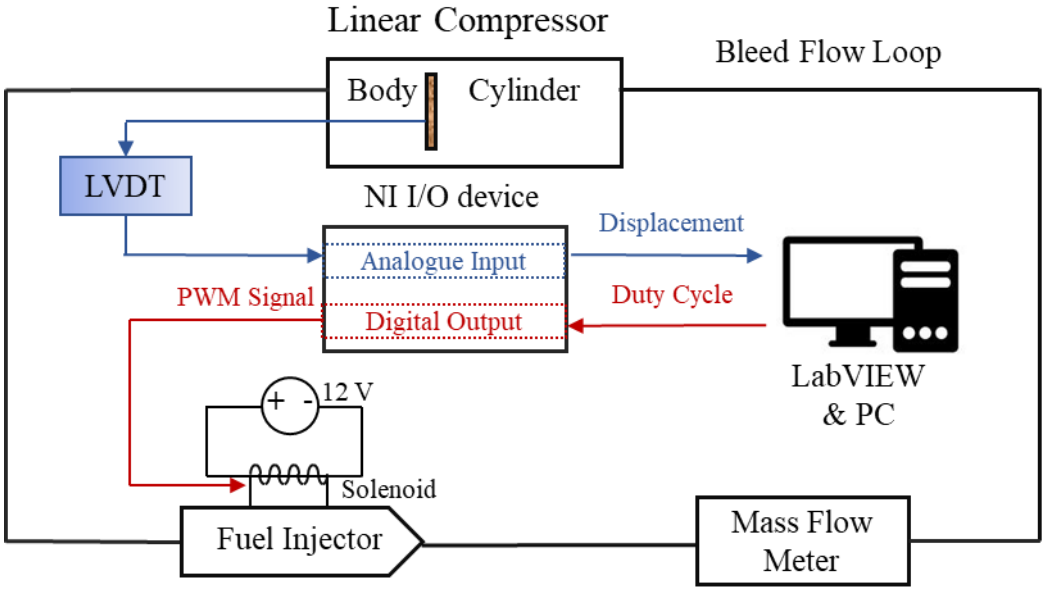

Fig. 2.13 Schematic of the LabVIEW-based piston offset control system

A LabVIEW-based PID control system was developed for the piston offset control, consisting of a PID controller in LabVIEW, a LVDT displacement transducer and a PWM controlled solenoid valve. The error was calculated as the difference between the actual value measured by the LVDT displacement transducer and the set point of piston offset. The error was attempted to be minimize by the duty cycle of the pulse and applies it to the solenoid, which drove the piston offset towards the set point by adjusting the body pressure via changing the bleed flow rate. Duty cycle is defined as the fraction of 'on' time to the period. A digital PWM signal of 50% duty cycle is shown in Fig. 2.14. The block diagram of the PID controller for the piston offset is shown in Fig. 2.15.

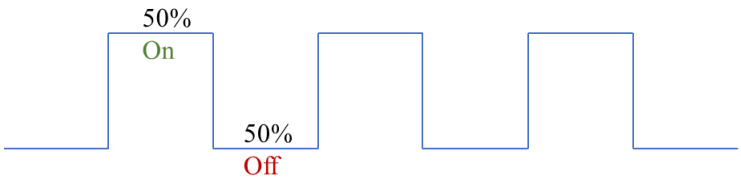

Fig. 2.14 Digital PWM signal of 50% duty cycle

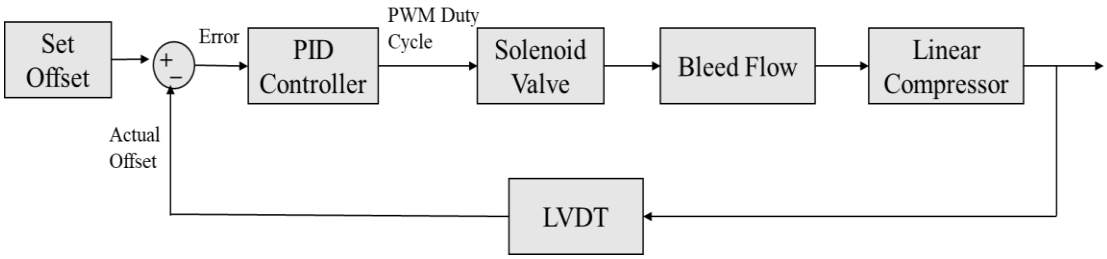

Fig. 2.15 Block diagram of the closed loop piston offset control

During operation, a series of pulses, with different duty cycles determined by the auto-tuned PID controller, were generated to switch on or off the solenoid valve to achieve an appropriate bleed flow reducing the body pressure. Therefore, the piston offset could be maintained at the set point.

2.3 Baseline Performance

2.3.1 Test Conditions

To experimentally evaluate the baseline performance of the linear compressor, a series of measurements were conducted at different pressure ratios, strokes and clearances using R1234yf which was readily available. R1234yf is also considered as alternative to R134a which is being phased out in the EU. Table 2.4 lists the test conditions for the baseline performance of the linear compressor. The driving frequency of the voltage signal was kept at the resonant frequency. The baseline performance was tested with a piston offset of 0 mm.

Table 2.4 Test conditions for baseline performance of the linear compressor

Working fluid	R1234yf
Charge (g)	250
Pressure ratio	2.0, 2.5, 3.0
Compressor stroke (mm)	9, 10, 11, 12
Condenser temperature (°C)	40
Operating frequency (Hz)	28-41
Suction temperature (°C)	33-38
Ambient temperature (°C)	22

2.3.2 *P-V* Diagram

Fig. 4.6 shows the measured pressure-volume (*P-V*) diagram for a stroke of 12 mm and a pressure ratio of 2.0 using R1234yf in which the suction and discharge pressures are also plotted. Four processes (suction, compression, discharge, and expansion) are clearly illustrated. There is significant pressure drop across the reed valves when they open. This will account for the overall efficiency of the linear compressor. The thermodynamic power calculated according to the area of the enclosed *P-V* loop for this condition is 23 W. This is lower than the shaft power (product of shaft force and piston velocity) 35 W. The difference between the two is due to the gas leakage across the 10 radial clearance gap and heat transfer through the cylinder wall. It can also be seen from Fig. 4.6 that the gas force looks very linear for the low pressure ratio.

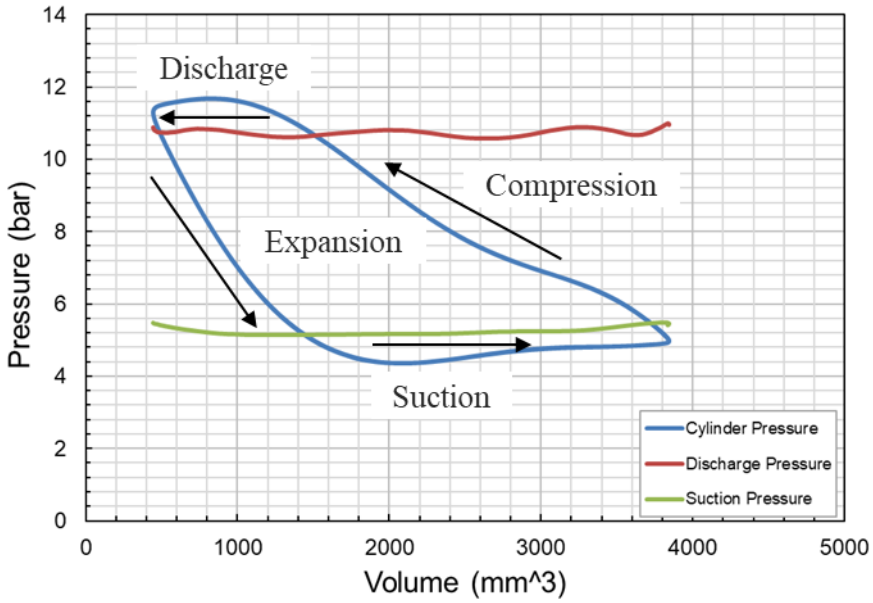

Fig. 2.16 *P-V* diagram of the linear compressor for a stroke of 12 mm and a pressure ratio of 2.0 using R1234yf

2.3.3 Mass Flow Rate and Power Input

Fig. 2.17 shows the mass flow rate against stroke for pressure ratios of 2.0, 2.5 and 3.0 using R1234yf as working fluid. When stroke is fixed, the mass flow rate decreases with the pressure ratio. Mass flow rate is higher for a larger stroke with a fixed pressure ratio. It can be seen that the mass flow rate of R1234yf is 0.92 g/s at a stroke of 12 mm and a pressure ratio of 3.0.

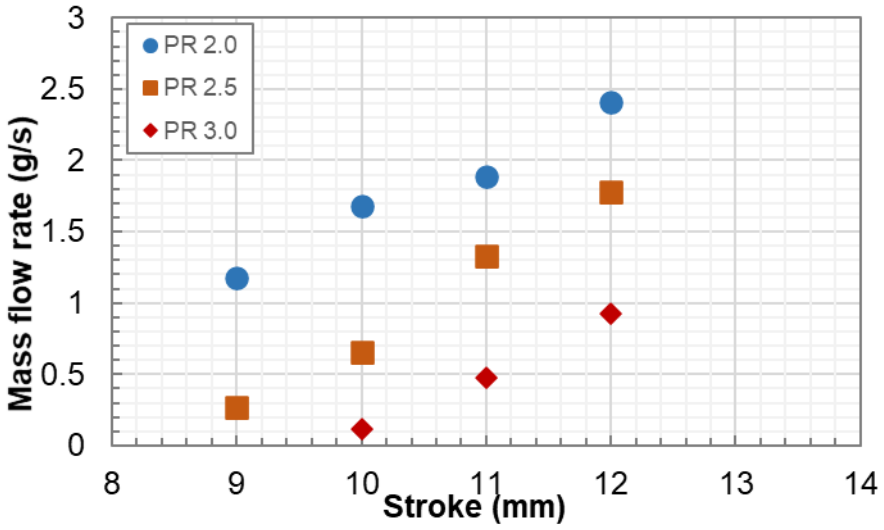

Fig. 2.17 Mass flow rate against stroke for various pressure ratios using R1234yf

Fig. 2.18 plots the power input to the compressor against stroke for various pressure ratios using R1234yf. It can be seen that the power input increases with stroke and the slope of power input against stroke also shows an increasing trend with the increase of pressure ratio. At a stroke 12 mm and a pressure ratio of 3.0, the power input into the linear compressor is 59 W. For a fixed stroke of 12 mm, power input decreased by 34% when the pressure ratio increases from 2.0 to 3.0.

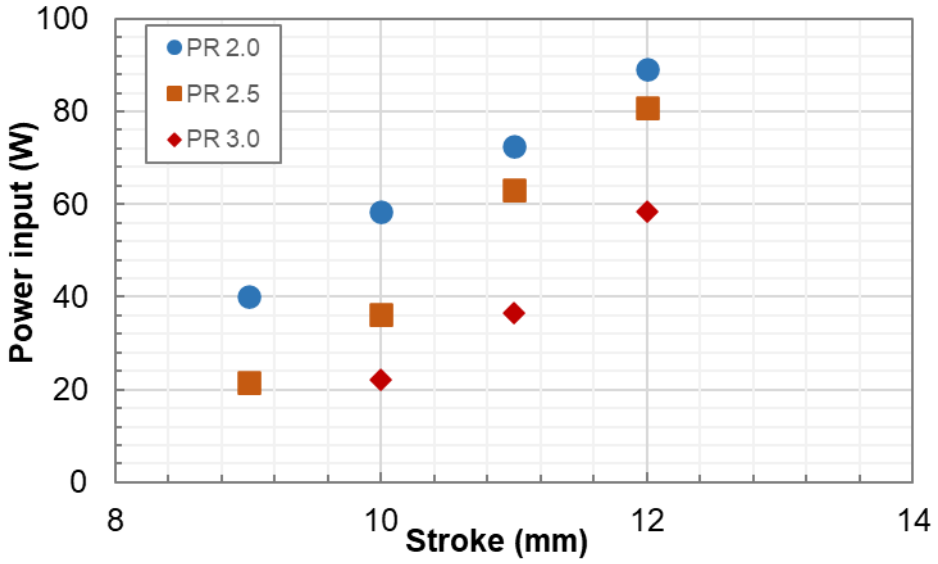

Fig. 2.18 Power input against stroke for various pressure ratios using R1234yf

2.3.4 Overall Efficiency and CoP

For an adiabatic process with an ideal gas, the theoretical power can be rewritten as a function of the suction temperature Tsuc (typically 22°C in operation), mass flow rate $\dot{m}$ and pressure ratio **[114]**

$$\dot{W}_{\mathrm{adb}} = \frac{\gamma}{\gamma-1}\dot{m}R_{\mathrm{g}}T_{\mathrm{suc}}\left[\left(\frac{P_{\mathrm{dis}}}{P_{\mathrm{suc}}}\right)^{\frac{\gamma-1}{\gamma}} - 1\right] \tag{2.1}$$

where γ is the adiabatic index, $\dot{m}$ is mass flow rate, T_{suc} is suction temperature, P_{dis} and P_{suc} are discharge and suction pressure respectively.

In contrast, for an isothermal process, the theoretical power $\dot{W}_{\mathrm{iso}}$ is

$$\dot{W}_{\mathrm{iso}} = \dot{m} R_{\mathrm{g}} T_{\mathrm{suc}} \ln\left(\frac{P_{dis}}{P_{suc}}\right) \tag{2.2}$$

However, due to the heat transfer and leakage, the actual thermodynamic power will be between the two calculated values above. Given that the linear compressor operated at a relatively high speed, and that the cylinder was not attached to a heat sink, the compressor tends to operate closer to the adiabatic than to the isothermal case.

Adiabatic efficiency $\eta_{\mathrm{o,adb}}$ and isothermal efficiency $\eta_{\mathrm{o,iso}}$ for the linear compressor are defined as

$$\eta_{\mathrm{o,adb}} = \frac{\dot{W}_{\mathrm{adb}}}{P_{\mathrm{in}}} \tag{2.3}$$

$$\eta_{\mathrm{o,iso}} = \frac{\dot{W}_{\mathrm{iso}}}{P_{\mathrm{in}}} \tag{2.4}$$

where P_{in} is power input which can be calculated with current and voltage supplied into the linear compressor.

Fig. 2.19 shows the adiabatic and isothermal efficiencies varying with the stroke for different pressure ratios using R1234yf. For the pressure ratio of 2.5, the average adiabatic efficiency is about 47% and the average isothermal efficiency is about 36%. The maximum adiabatic efficiency is 55% when the stroke is 9 mm and the pressure ratio is 2.0. Considering the losses associated with seal leakage, DC offset and heat transfer, these two efficiencies are plausible values for the linear compressor performance.

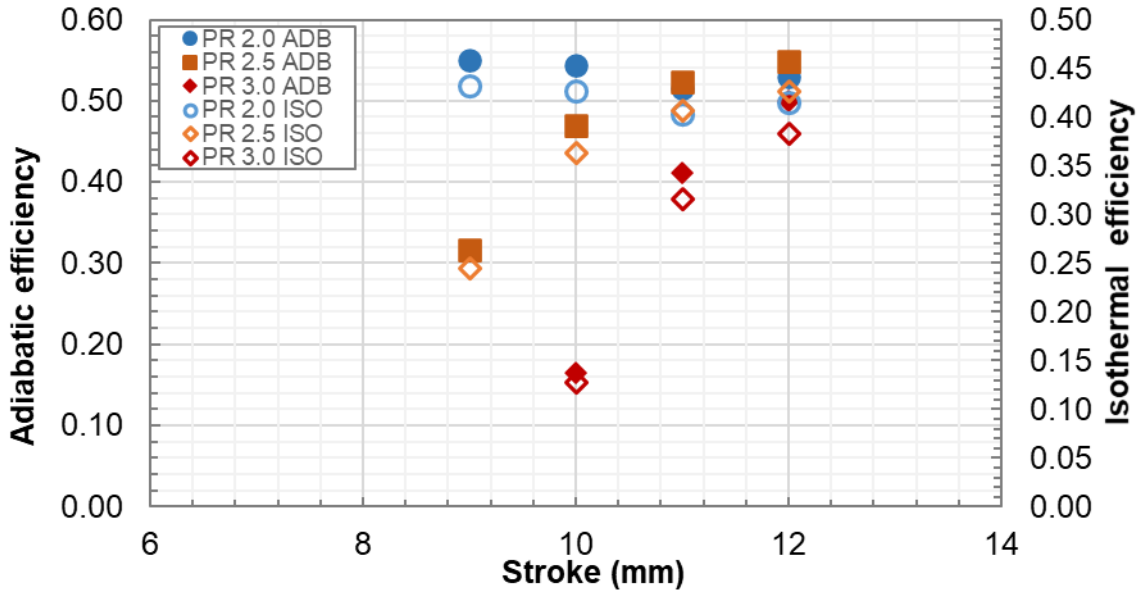

Fig. 2.19 Adiabatic and isothermal efficiencies against stroke for various pressure ratios using R1234yf

The refrigeration system cooling capacity $\dot{Q}$ can be calculated as follow

$$\dot{Q} = \dot{m}(h_s - h_{eva}) \tag{2.5}$$

where h_s is enthalpy of suction state and h_{eva} is enthalpy of evaporator inlet state.

The refrigeration system coefficient of performance (CoP) is defined as follow

$$CoP = \frac{\dot{Q}}{P_{in}} \tag{2.6}$$

With the measured pressure and temperature for suction and evaporator inlet temperature, the corresponding enthalpies can be estimated by using the Ethermo Thermodynamic & Transport Properties Calculation Platform and Thermo-physical Properties of Fluid Systems **[115]**. Cooling capacity can be calculated accordingly.

Cooling capacity for strokes of 9 mm to 12 mm at pressure ratios (PRs) of 2.0, 2.5 and 3.0 with R1234yf as refrigerant is shown in Fig. 2.20. At a fixed stroke, cooling capacity decreases with pressure ratio. However, the opposite trend can be observed for stroke when pressure ratio is fixed. Cooling capacity increases 209 W when stroke increases from 9 mm to 12 mm with a pressure ratio of 2.0.

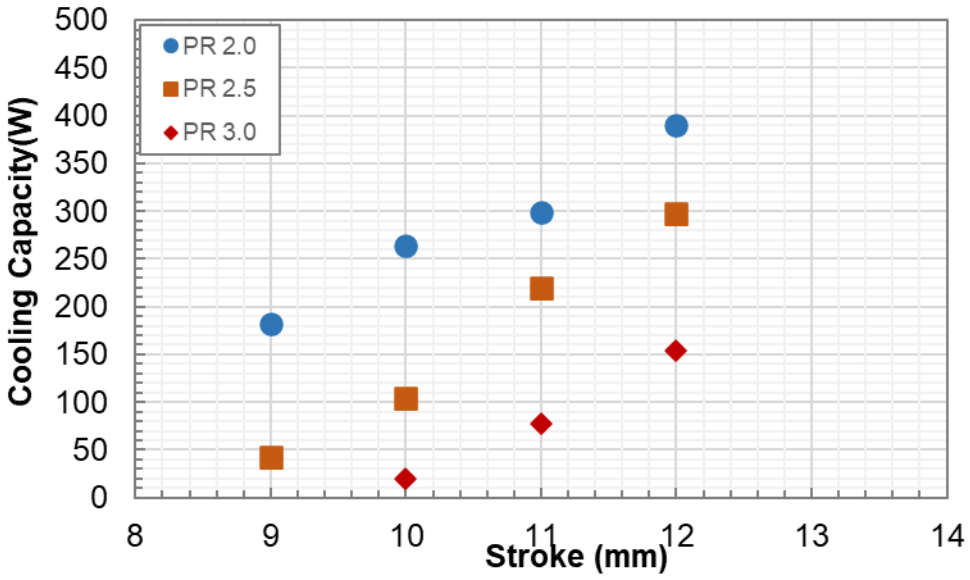

Fig. 2.20 Cooling Capacity against stroke for various pressure ratio (PRs) using R1234yf

Fig. 2.21 shows CoP against stroke for pressure ratios of 2.0, 2.5 and 3.0 using R1234yf as refrigerant. CoP decreases with pressure ratio due to the decrease in mass flow rate. For pressure ratios of 2.5 and 3.0, CoP increases with stroke. When operated at a pressure ratio of 2.0 and a stroke of 12 mm, the CoP is 3.5.

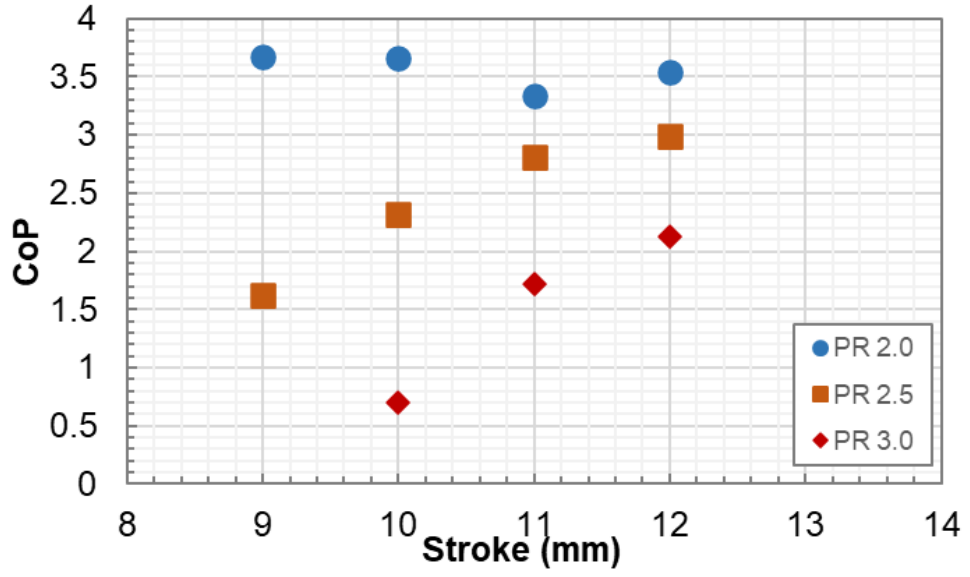

Fig. 2.21 CoP against stroke for various pressure ratios using R1234yf

It can be seen that the linear compressor can achieve cooling capacity modulation by adjusting compressor stroke. The A higher stroke is desired for a higher load condition. Compared with the on-off control strategy for modulating cooling capacity, the cycling loss is significantly improved. To improve the CoP of the system, lots of aspects can be considered such as improving motor efficiency, reducing leakage and heat losses, and improve the efficiency of heat exchangers.

2.4 Conclusions

This chapter introduces the test rig and instrumentations that can be used for the system performance evaluation and data collections. The experimental test facility consists of a linear compressor, a condenser and an evaporator with an electric heater and a throttling/expansion valve installed between the condenser and evaporator, which enables pressure ratio adjustment. A LabVIEW program was introduced for data logging, key parameters monitoring and implementing control system. The data acquisition systems for the linear compressor measurements consists of a low-speed DAQ (LDAQ) system and a high-speed DAQ (HDAQ) system. Processed data can be recorded with the LabVIEW program and data files were saved to predefined directories.

The LabVIEW program includes two controllers, both of which are PID controllers. One is used for stroke control, which controls the stroke of compressor by adjusting the amplitude of output voltage. The amplitude of voltage was determined by the stroke error and PID parameters. The other is used for piston offset control consisting of a PID controller, a LVDT displacement transducer and a PWM controlled solenoid valve. By adjusting the duty cycle of the pulse that determines the fractions of on/off time of the solenoid valve, the bleed flow rate and pressure difference between cylinder side and body side can be regulated, so the set point of piston offset can be achieved.

A number of tests were conducted in the rig to experimentally evaluate the performance of the linear compressor with an offset of 0 mm using R1234yf as refrigerant. Mss flow

rate and power input increase with piston stroke, but decrease with pressure ratio. Overall efficiency including adiabatic efficiency and isothermal efficiency were also presented. When operated at a pressure ratio of 2.0 and a stroke of 12 mm, the CoP is 3.5.

It can be concluded that the prototype linear compressor is capable of capacity modulation by tuning compressor stroke, no on/off loss and high efficiency. In next chapter, the details of linear motor including motor force characteristics, motor losses and motor efficiency will be investigated so that further improvement on the compressor efficiency can be recommended. The test rig in this chapter will also be used to validate the linear motor model in Chapter 3, to investigate the minimum clearance effect in Chapter 4, to provide data points for the ANN model in Chapter 5 and to validate the sensor-less stroke detection technique in Chapter 6.

Chapter 3 Modelling of the Moving Magnet Linear Motor

3.1 Finite Element Analysis Model

To analyse the performances and electromagnetic characteristics of linear motors, the distribution of magnetic field is needed. Numerical and analytical methods can be used for the evaluation of magnetic field distribution. Finite Element Analysis (FEA), as a numerical solution, presents advantage of considering the nonlinear magnetic saturation of cores and the real geometry of the motor design. By solving the governing equations issued from Maxwell's equations, the magnetic field can be evaluated **[116, 117]**. Static shaft forces for various armature positions of moving magnet linear motor were calculated using FEA **[118, 119]**. Li et al. **[120]** compared some key performance indexes between a novel moving iron and a moving magnet linear motor. FEA has been employed to optimize the design of linear motors. A tubular moving-magnet linear magnet motor was optimized by Abdalla et al. **[121]** to improve efficiency and reduce losses. The application of FEA also includes quantification of eddy current loss in linear permanent magnet motor as presented by Ko et al. **[122]** and Abdalla et al. **[123]**.

Static analysis can give the motor constant of the linear motor, and transient analysis is capable of simulating parameters varying with time. To simulate the static and dynamic characteristics of the novel linear motor, a three-dimensional FEA model was built in ANSYS Maxwell 19.2. The simulation was carried out with the following assumptions:

(1) The influence of the strut used to place and support three magnets on the flux distribution can be neglected so that the model can be simplified;

(2) Coils are wounded uniformly around cores, and current distributes uniformly at each conductor.

Fig. 3.1 shows the FEA mesh of the proposed linear motor. Maxwell adopts an adaptive iterative process to produce optimal mesh in which the mesh in high error density is

refined. It can be seen that the mesh is very dense in the air gap between magnets and cores. Relatively fine mesh was also used in the magnets region where the shaft force is integrated. Length-based mesh refinement inside objects was applied to cores, magnets and air gap between them. Desired calculation accuracy was ensured when the maximum element length for cores, magnets and gaps were restricted smaller than 0.1 mm, 0.05 mm and 0.01 mm respectively.

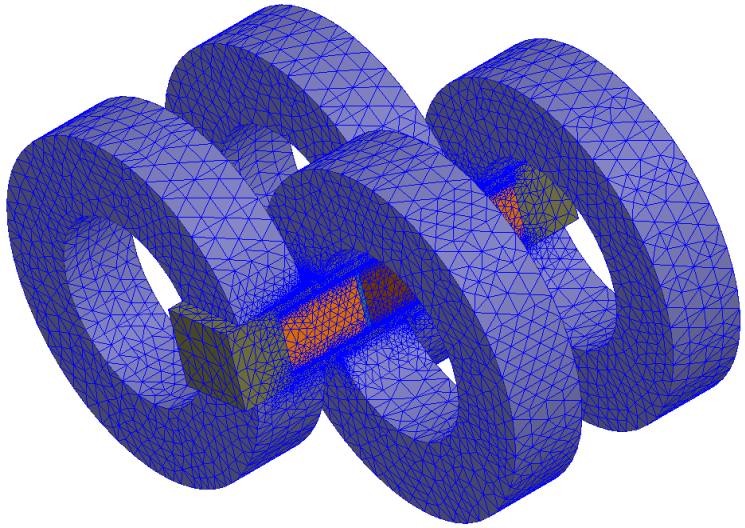

Fig. 3.1 FEA model of the moving magnet linear motor in ANSYS Maxwell

Current multiplied by the number of coil turns was applied to each winding through a section perpendicular to its flow path. The direction of current was opposite for windings at each side of magnets. Two types of default boundary conditions were defined: natural boundary condition and Neumann boundary condition. Magnetic field is continuous across object interfaces according to natural boundary condition. For Neumann boundary condition, magnetic field is tangential to the outer boundary and flux cannot cross it. Insulating boundary conditions was set between the surfaces of windings and cores as there was insulating cover for each coil. The nonlinear residual error, which defines how precisely the nonlinear solution must define the B-H nonlinear operating points was set to be 0.001 for the 3D Magneto-static solver.

3.2 Static Analysis

3.2.1 Computational Method

In a magneto-static solution, the magnetic field is produced by DC currents flowing in coils and by permanent magnets. There is no time variation effect included in a magneto-static solution, and objects are considered to be stationary. The Maxwell 3D Magneto-static module is capable of solving static electromagnetic problem for stationary objects when the magnetic field is produced by permanent magnets and by DC current flowing in conductors.

Maxwell's equations consist of four equations including Gauss's law, Gauss's law for magnetism, Faraday's law and Ampere's law with Maxwell addition. Four coupled equations form a complete description of the production and interrelation of electric and magnetic fields. Two Maxwell's equations are solved with the 3D Magneto-static solver, one is derived from Ampere's law with Maxwell's addition, which is

$$\nabla \times \vec{H} = \vec{J} \tag{3.1}$$

where H is the magnetic field density, B is flux density, and J represents current density.

The other equation is Gauss's law for magnetism

$$\nabla \cdot \vec{B} = 0 \tag{3.2}$$

where B is flux density.

The linear constitutive relation in a magnetic medium is:

$$\vec{B} = \mu_r \mu_0 \vec{H} + \mu_0 \overrightarrow{M_p} \tag{3.3}$$

where μ_0 is the permeability of vacuum and μ_r is the relative permeability, $\overrightarrow{M_p}$ is the

permanent magnetization.

For nonlinear material, ANSYS Maxwell provides an advanced setup option allowing a solution based on a previously computed demagnetization operating point

$$\vec{B} = \overrightarrow{B_0} + [\tilde{\mu}](\vec{H} - \overrightarrow{H_0}) \tag{3.4}$$

$$[\tilde{\mu}] = \frac{\partial}{\partial \vec{H}}\vec{B} = [\Delta\tilde{\mu}] + [\mu] \tag{3.5}$$

Where $\overrightarrow{B_0}$ and $\overrightarrow{H_0}$ are the previous field solution, $[\Delta\tilde{\mu}]$ is a general full tensor, $[\mu]$ is magnetic permeability matrix.

In Maxwell 3D Magneto-static solver, magnetic field $\vec{H}$ is considered to be composed of the following components:

$$\vec{H} = \overrightarrow{H_s} + \nabla\varphi + \overrightarrow{H_p} \tag{3.6}$$

where φ is the magnetic scalar potential, $\overrightarrow{H_s}$ is a particular solution constructed by assigning values to all the edges in the mesh in such a way that Ampere's law holds on all contours of all tetrahedral faces in the mesh, $\overrightarrow{H_p}$ accounts for the permanent magnets.

Once the magnetic scalar potential is obtained, Maxwell's equations and the constitutive relationship are then used to obtain the magnetic field and magnetic flux density. The advantages of this formulation over other existing ones includes saving considerably computational resources, the absence of a gauge due to excellent numerical stability, and lowing cancellation errors **[124]**.

3.2.2 Static Force Simulation

Fig. 3.2 shows the flux density distribution of the linear motor when 1.5 A was applied to each coil at armature position 0 mm. As can be seen, flux density distribution in three cores is similar while the flux density in the other core is very mall. This is because this core and its winding coil form a magnetic circuit with large space air, whose magnetic

reluctance is large. All of the other three coils form the magnetic circuit with one magnet and small air gap. Large flux density is shown at the slotting corners of cores that are close to the magnet in its circuit, while very small flux density can be found at the slotting corners on the other side.

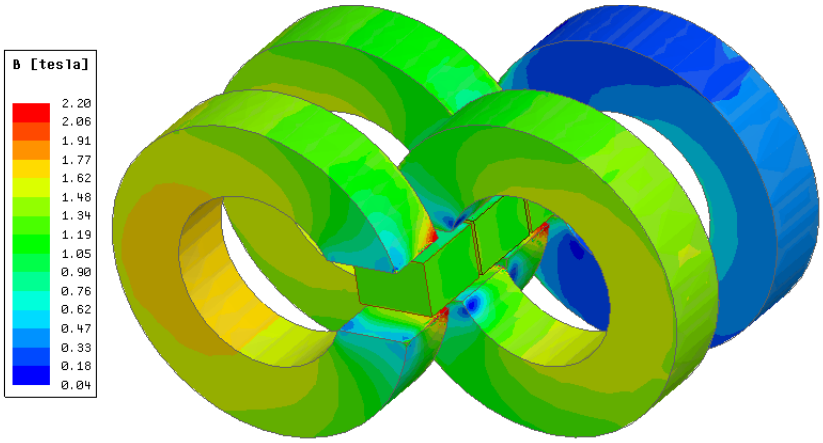

Fig. 3.2 Magnetic flux density distribution of the linear motor with a current of 1.5 A at armature position of 0 mm

Even when no current is applied to coils, there is magnetic force (shaft force) applied on magnets. The effect of magnetic force can be equivalent to a spring, the piston-magnets moving assembly can be regarded as a mass-spring-damper system. The position-dependable interaction of permanent magnets and cores when zero current is applied to the motor can be referred as magnet spring **[125]**. The induced magnetic spring affects the resonant frequency of the mass-spring-damper system. A general equation of the resonant frequency in a mass-spring-damper system is:

$$f = \frac{1}{2\pi}\sqrt{\frac{k}{m}} \tag{3.7}$$

where f is the resonant frequency, m is moving mass (magnet and piston assembly), and k is the total spring stiffness.

FEA simulations were carried out at different armature positions to investigate the magnet spring force. The shaft force at different positions varying from -8mm to 8mm is shown

in Fig. 3.3. It can be seen that when armature is at its central position, the shaft force applied on magnets equals to zero. However, with the increase of the displacement, the shaft force also increases. The shaft forces when zero current excitation are also defined as magnetic spring force, which corresponds to magnetic spring stiffness when calculate the system resonance as presented in section 4.3. The direction of the magnet spring force is the same as its displacement direction, which means the magnet spring force tends to move the armature further from its central position if the motion is not constrained. The magnet force is distributed symmetrically along the central position of armature. When the armature position is 8 mm, the magnet spring force is 9.9 N. Magnetic spring stiffness is defined as the ratio of magnetic spring force to displacement. This corresponds to a magnet spring rate magnitude of 1.24 N/mm.

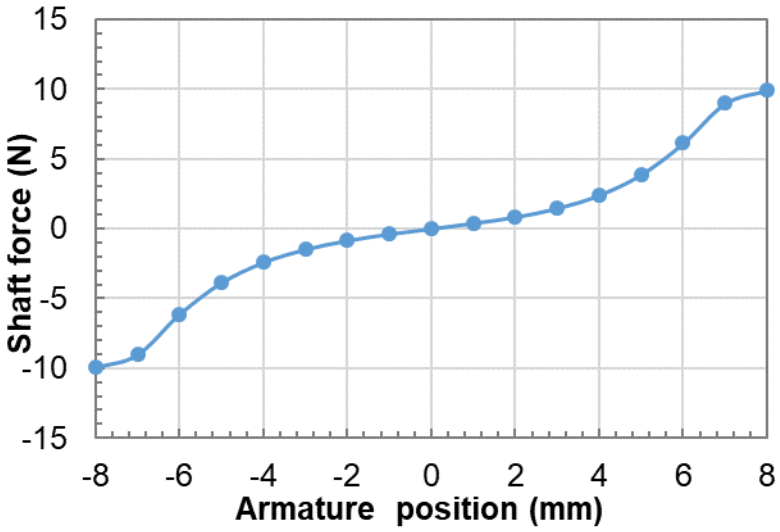

Fig. 3.3 Shaft force variation with armature position without excitation current

3.2.3 Static Force Measurement

Static motor force measurements were conducted at different armature/piston positions and different excitation currents. Fig. 3.4 shows the schematic diagram of static motor force measurement. There is a 10 μm clearance between piston and cylinder wall to reduce the friction loss and to have least gas leakage. The four coils were connected in series, and a DC current through a power amplifier was supplied to the linear motor. A

Hall Effect current transducer was utilized to measure the DC current. A linear variable differential transformer (LVDT) displacement transducer was used to measure the armature/piston position. Helium gas was charged into the linear compressor to maintain a certain armature position through the suction port or the body port, depending on the direction of the DC current flow. A pressure gauge was used to measure the gas pressure when the armature/piston position was settled.

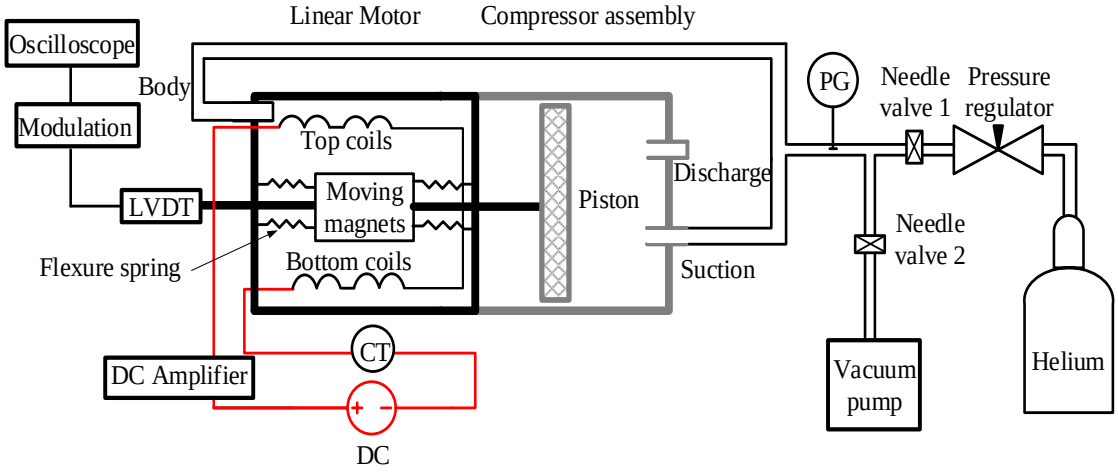

Fig. 3.4 Schematic diagram of static motor force measurement (PG: pressure gauge, CT: current transducer, c: radial clearance, LVDT: linear variable differential transformer)

The armature/piston position for testing ranges from -7 mm to 7 mm in a step of 1 mm. For each armature/piston position, the DC current was changed from -1.8 A to 1.8 A in a step of 0.2 A. For each operating condition (excitation current), the pressure regulator was adjusted manually to keep the armature/piston at its desired position. Note that the force measured is a resultant force of axial mechanical spring force and static motor force. The static motor force F_{m} can be estimated according to

$$F_{\mathrm{m}} = P * A - k_{\mathrm{m}} * x \tag{3.8}$$

where P is the gauge pressure (either body pressure or suction pressure), k_{m} is mechanical spring stiffness, and x is displacement measured by the LVDT displacement sensor.

Instruments for the measurement of static motor force are listed in Table 2.

Table 3.1 List of instruments for static motor force measurements

Instruments	Model	Accuracy
Current transducer	LA LEM 25-NP	±0.5 %
LVDT	Lucas Schaevitz	± 0.025 mm
LVDT modulator	ATA-101	Phase shift： 5 degrees for 50 Hz
Pressure gauge	DRUCK 1400	±0.15 %
Capacitor	EPCOS B32361	±5 %
DC Power amplifier	22AH370 /00 /15 /29	Not applicable
Helium gas	BOC	Not applicable
Vacuum pump	Gardner Denver–WZ-79204-05	Max Vacuum (mbar) 132.9

3.2.4 Interpolation of Dynamic Motor Force

During the linear compressor operation, the motor force varied continuously with the armature/piston position and instantaneous excitation current. Measuring the dynamic motor force directly was difficult. Interpolating dynamic motor force was conducted to reveal the dynamic motor force characteristic. The measurements of static motor forces at different armature position with various excitation current provides a force-current-displacement 3-D map which can be used for the interpolation. Fig. 3.5 gives the linear motor Force-Current-Displacement 3-D map according to the static motor force measurement. The shaft force at different armature positions with various excitation current can be interpolated accordingly.

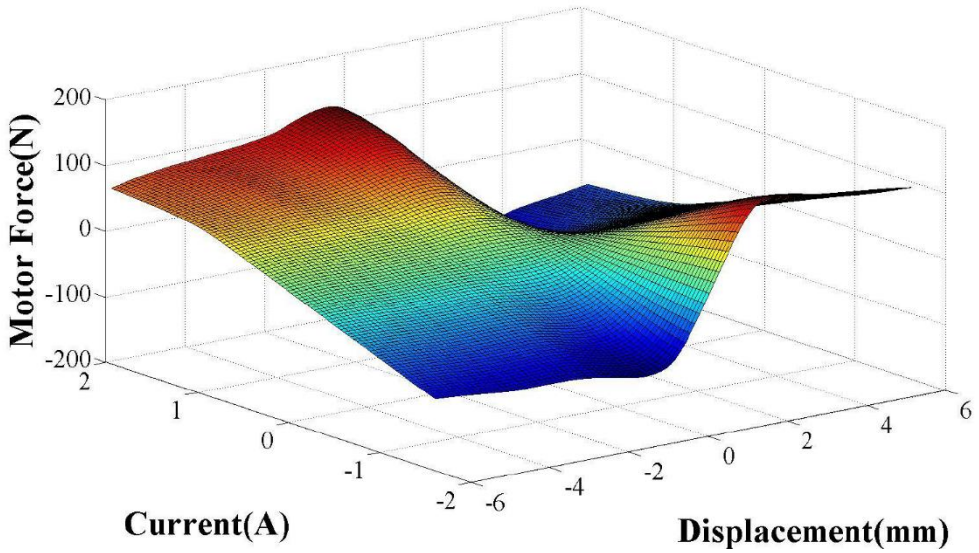

Fig. 3.5 Linear motor Force-Current-Displacement 3-D map from the static motor force measurement

Fig. 3.6a shows the measured voltage and current in one cycle for a pressure ratio of 2.0, a stroke of 6 mm, and a drive frequency of 31.5 Hz. It can be seen that there is a phase difference between the voltage and current. The voltage signal leads the current signal about 40º phase angle, which means that the inductance in linear motor has not been balanced by the capacitor. This is due to the limited range of capacitance box. The amplitude of voltage is 85 V, and the amplitude of current is about 2.1 A. Note that the measured current is for two linear motors in parallel, so that the real power consumed by each linear motor is about 68 W. A 23% voltage input can be reduced if a matched capacitor is used.

Fig. 3.6b shows the measured displacement and the interpolated motor force in one cycle for this particular test condition. The interpolated motor force is shown to vary as a sinusoidal function over a cycle. As can been seen, phase angle difference between displacement and shaft force is about 70º. It indicates that the drive frequency is lower than the resonant frequency of linear compressor because Chun et al. **[126]** reported that the angle between displacement and current should be smaller than 90º when drive frequency is lower than resonant frequency. It can be seen from Fig. 6 that the drive frequency is 31.5 Hz. The amplitude of interpolated shaft force is 73 N. The shaft force

leads the displacement about 90º as expected. This is because shaft force should be in phase with velocity according to Faraday law of induction.

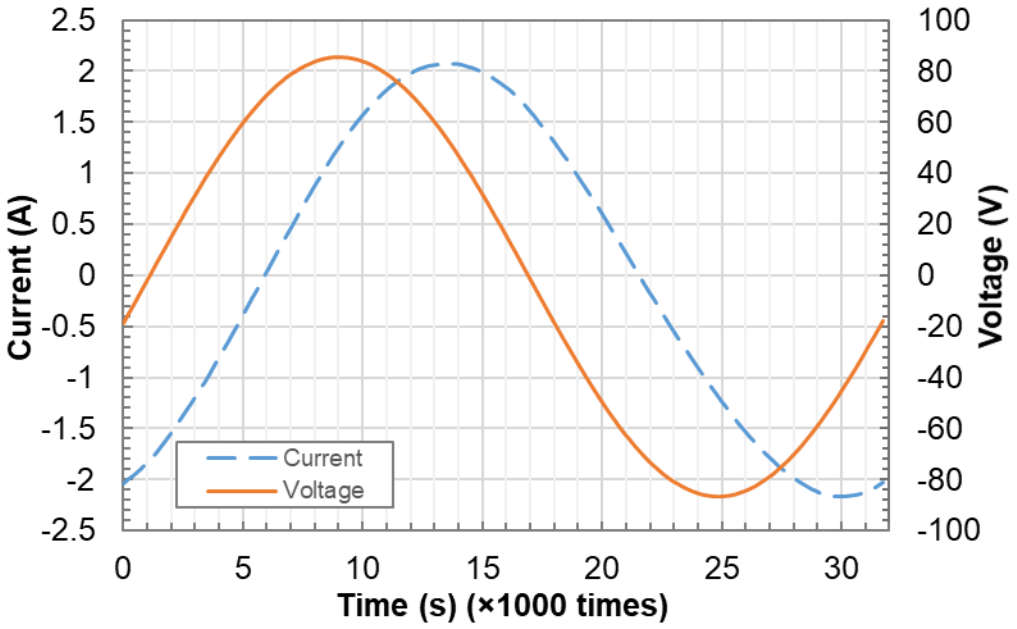

(a)

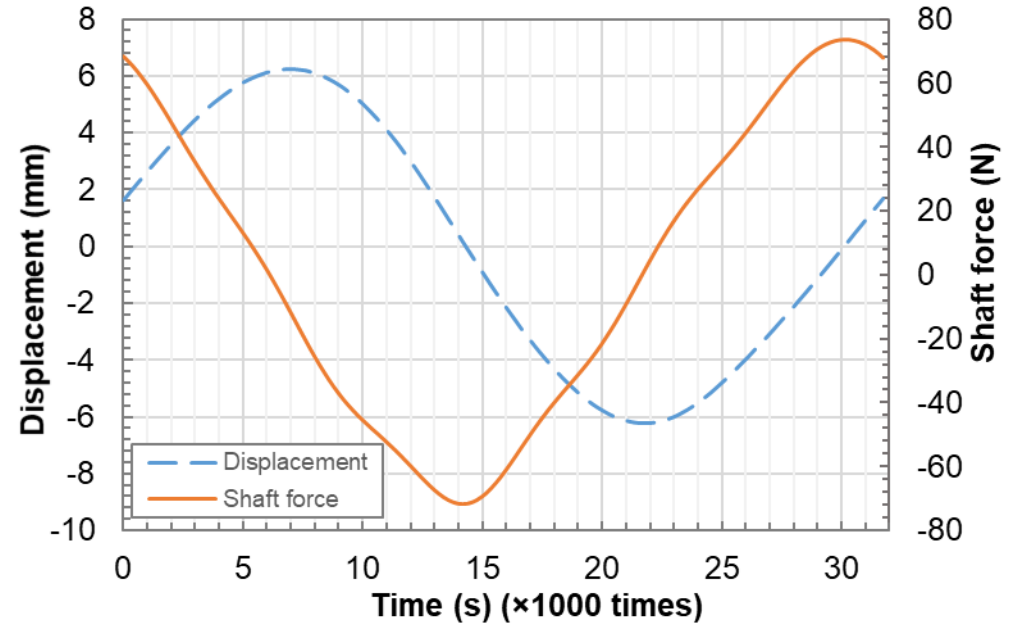

(b)

Fig. 3.6 Measured voltage, current, displacement and interpolated shaft force in one cycle for a pressure ratio of 2.0, a stroke of 12 mm and a drive frequency of 31.5 Hz; (a) measured current and voltage (b) measured displacement and interpolated shaft force

3.2.5 Comparison of Static Motor Force between FEA Simulation and Measurement

Fig. 3.7 shows the comparison of static motor force varying with excitation current at armature position of -2 mm and -4 mm between the FEA simulation and measurement. Note that negative displacement means moving towards the cylinder head. Generally, the FEA simulation results are in very good agreement with the measured results. It can be seen that motor force increases as current increases. The variation of motor force with current at a fixed armature/piston position includes linear part and nonlinear part. The difference between the FEA simulation and the measurements in linear part can be ignored. In the linear part, the slope of force variation is the force constant of this motor. As shown in Fig. 3.7 the force constant for the position -2 mm is about 31.5 N/A while the force constant for the position -4 mm is about 31 N/A. The force constant decreases to 60 N/A when the armature position is 6 mm away from the centre. At the maximum position (±7 mm), the force constant is 25 N/A.

With the increase of the excitation current after 1.2 A for the armature position of -2 mm, saturation of motor force occurs, which is due to the nonlinear permittivity of the core. The positive saturation current is smaller than the negative saturation current. In Fig. 3.7a, the measured positive saturation occurs at a current of 1.2 A, while motor force does not saturate even when negative current reaches -1.8 A. It can also be seen that the more distance that the moving assembly moves away from the datum position, the earlier saturation will occur. The difference between the FEA simulation and the measurements in non-linear part is caused by the hysteresis characteristic of core, which has not been considered in the FEA simulation. As the hysteresis loop of soft material is very narrow, its influence on the linear part is small while the influence on saturation analysis is more obvious. Consider that the linear motor is operated in the linear part in most cases, the largest difference of nonlinear part is about 18%, FEA results are acceptable.

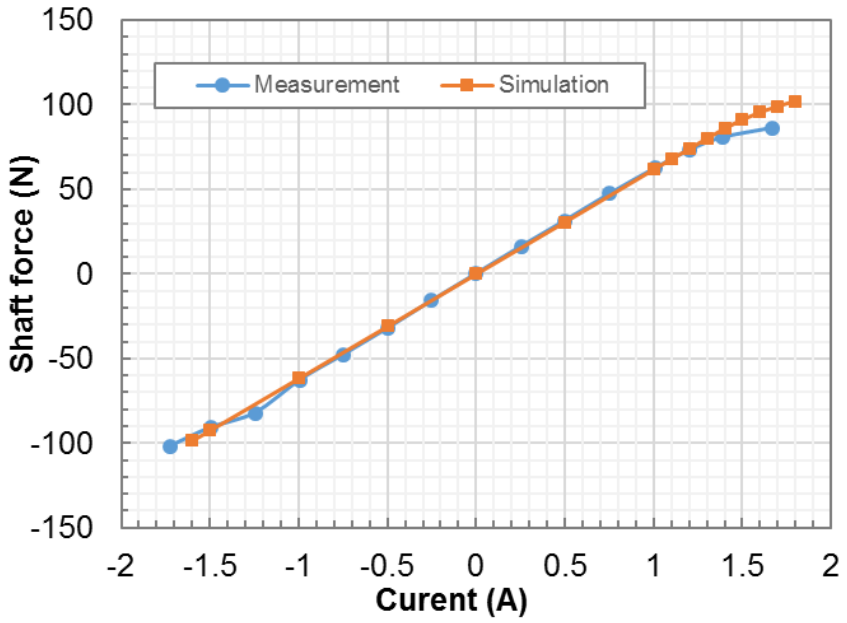

(a)

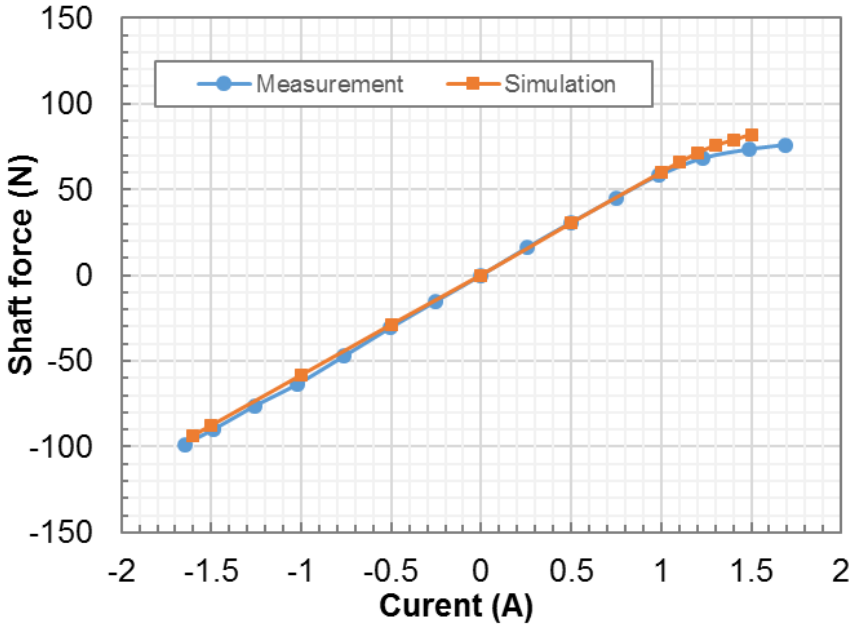

(b)

Fig. 3.7 Shaft force varying with current at different armature positions; (a) -2mm (b) -4 mm

3.3 Transient Characteristics

3.3.1 Transient Solver

During operation, current and piston displacement vary with time, transient analysis can be carried out to simulate motor force and losses as a function of time. In a time-domain transient solution, the instantaneous magnetic field at each time step was solved step by step. In the FEA model, boundary conditions, motor geometry and all materials properties were defined. Faraday's Law of induction, Gauss's Law for magnetism, Ampere's Law, and Gauss's Law for electricity were included in the Maxwell's equations. Low-frequency forms of Maxwell's equations are employed in ANSYS Maxwell 3D Transient Solver **[124]**:

$$\nabla \times \frac{1}{\sigma}(\nabla \times H) + \frac{\partial B}{\partial t} = 0 \tag{3.9}$$

$$\nabla \cdot B = 0 \tag{3.10}$$

$$-\nabla \cdot \left(\varepsilon \nabla \frac{\partial \Phi}{\partial t}\right) - \nabla.(\sigma \nabla \Phi) = 0 \tag{3.11}$$

where B is the magnetic flux density, H is the magnetic field strength, Φ is the magnetic flux, σ and ε are the conductivity and permittivity of the material respectively.

To obtain a closed system, the constitutive relations describing the macroscopic properties of the medium, are also included. The electric and magnetic flux density D, B are related to field intensities E, H via the constitutive relations. In magneto-static solver, Maxwell adopts an adaptive iterative process to refine the mesh until required accuracy is met or maximum number of passes is reached. However, transient solver is not capable of improving initial mesh automatically. Current from measurement was applied to each winding and measured displacement was also defined in the motion setup to include translational motion effects. The nonlinear residual error for the transient solver was set to be 0.001.

3.3.2 Flux Density

Fig. 3.8 shows the current and displacement signals in one cycle from measurements when the linear motor drives the linear compressor with an operating frequency of 34 Hz

and a stroke of 11 mm. Both the current and displacement signals are sine waves. The amplitude of current is 1.6 A, and the current lags the displacement by 86 degree. This results from the combined impact of the equivalent reluctance of gas load, electrical inductance, and capacitance.

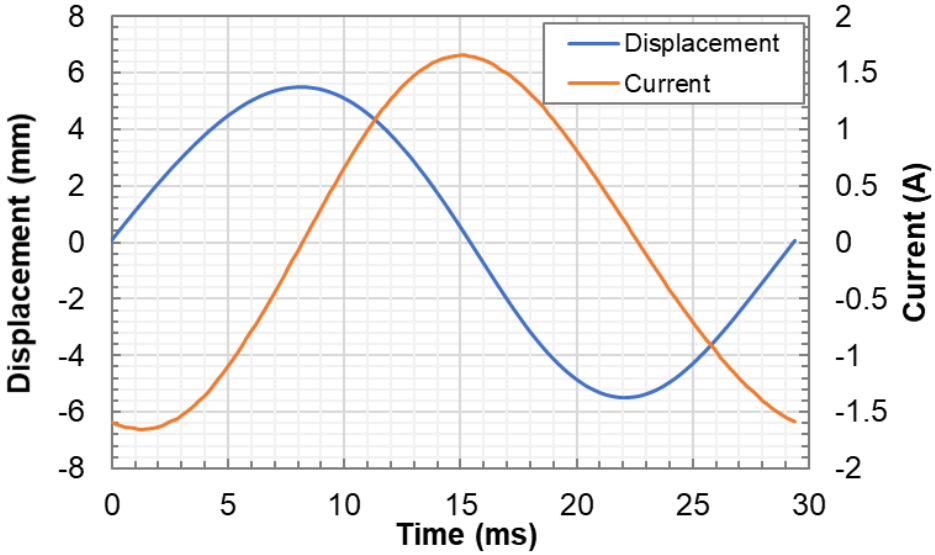

Fig. 3.8 Measured displacement and current in one cycle at a stroke of 11 mm and a frequency of 34 Hz

Fig. 3.9 shows the flux density distribution when a sinusoidal RMS 1.2 A current was supplied to drive a motion of a stroke of 10 mm. As can be seen from Fig. 3.9a and Fig. 3.9b, the magnetic flux density in three cores is similar while the flux density in the other core is much smaller.

As the armature moves from 0 mm to 5.5 mm, instantaneous current varies from -1.6 A to 0 A, the core of the smallest flux density changes from the one at most negative side to the most positive side (the positive direction pointing out of the page). Magnetic field in one core is created by electrified windings and permanent magnets. With the variation of permanent position, the air reluctance between each magnet and core changes and the magnetic flux density induced by permanent magnets changes accordingly. As shown in Fig. 3.9b, the core at most negative side is the farthest from magnets so that the large magnetic reluctance of air results in the very small flux density in that core.

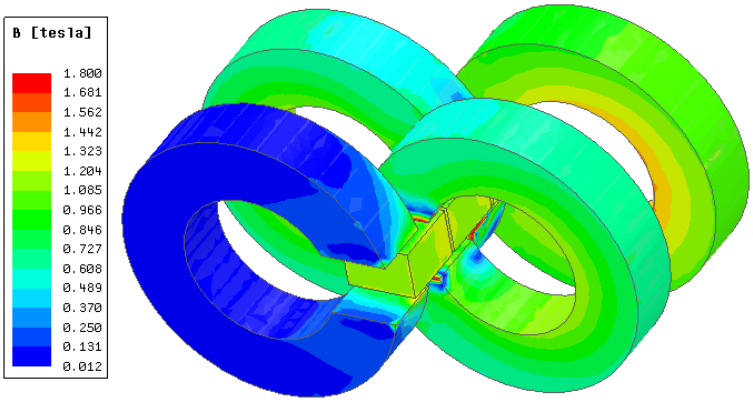

(a)

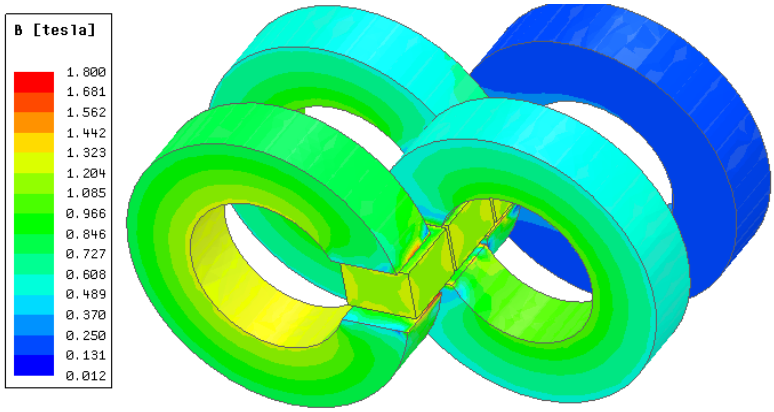

(b)

Fig. 3.9 The distribution of magnetic flux density at a stroke of 11 mm and with a sinusoidal RMS 1.2 A current supply (a) at displacement of 5.5 mm (b) at displacement of 0 mm

3.3.3 Transient Motor Force

Comparison of transient motor (shaft) force between the results from the FEA model and static measurements are shown as Fig. 3.10. The AC current and the motion of magnets were described with harmonic terms that were determined using FFT (Fast Fourier Transform) analysis, and were defined in the FEA model. To verify the simulation results, interpolations were made with the Force-Current-Displacement 3-D map from the static motor force measurements as shown in Fig. 3.5. It can be seen from that simulated shaft force from the FEA model is consistent with that of 3-D map interpolation. The motor

force varies sinusoidally in one cycle with a peak and a trough at 0.9 ms and 14.1 ms as shown in Fig 3.10a, which corresponds to displacement of 0.9 mm and 1.0 mm respectively. The amplitude of shaft force is 35 N at a stroke of 9 mm and 51 N at a stroke of 11 mm as shown in Fig. 3.10a and Fig. 3.10b. The maximum error between the motor force calculated from the FEA model and interpolation from the static force measurements is 6% and 9% respectively at peak values.

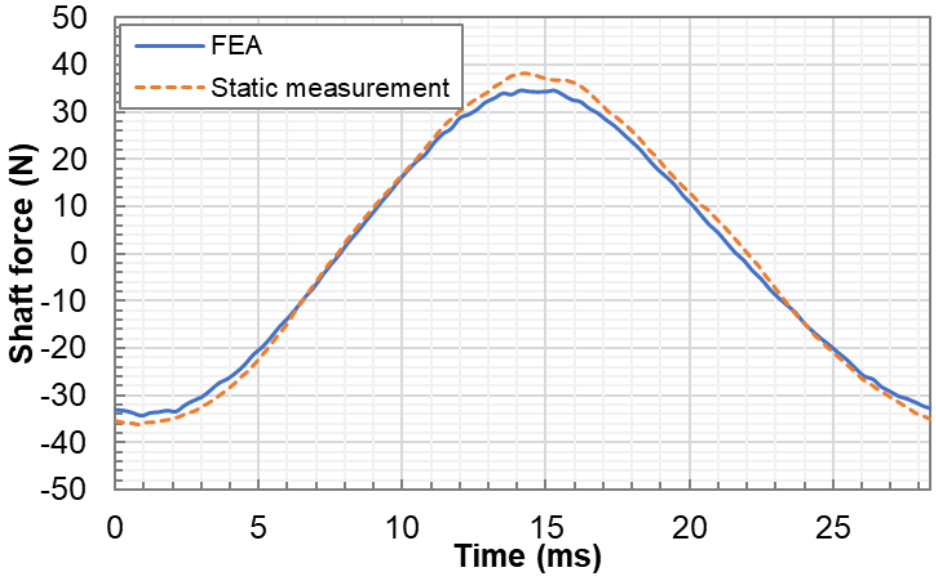

(a)

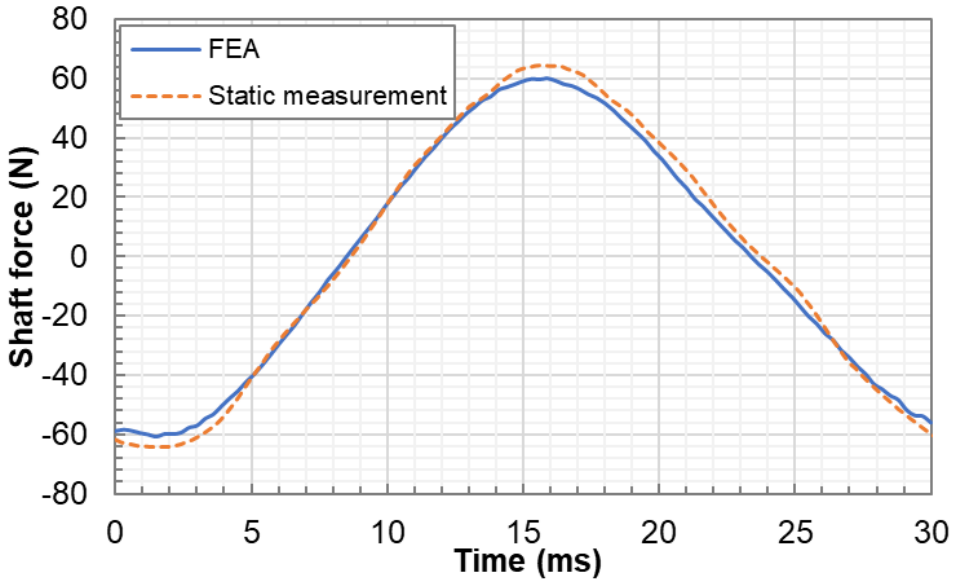

(b)

Fig. 3.10 Transient motor force in one cycle from the FEA model and 3-D map

interpolation (a) a stroke of 9mm (b) a stroke of 11 mm for the moving magnet linear motor

3.3.4 Losses Analysis

Some of the input power into the linear motor that would ideally be converted into shaft power is lost in the core. The specific total loss of the against peak magnetic polarization for the core material was tested and provided by the manufacturer. The specific core loss curve (B-H curve) was defined in the simulation environment and the core losses are calculated for a specific frequency of 50 Hz. The Steinmetz model is often used to estimate iron loss. The total core loss includes eddy current loss and hysteresis loss **[127]**. It can be expressed as follows:

$$P_{\text{core}} = P_{\text{h}} + P_{\text{e}} = K_{\text{h}} f B^{\alpha} + K_{\text{e}} f^2 B^2 \tag{3.12}$$

where K_{h}, K_{e} and α are hysteresis and eddy loss coefficients respectively, which are coefficients that depend on lamination, material thickness, conductivity and other factors, B denotes the amplitude of the flux density, f represents the electrical frequency.

Additional eddy current loss exists in the permanent magnets and windings. The resistive losses of induced eddy currents inside the linear motor can be expressed as follows:

$$P_{ae} = \frac{1}{\sigma} \int J^2 \cdot dV \tag{3.13}$$

where V is the volume of the body, J is density of the eddy current.

Based on the FEA model, core loss and additional eddy current loss of coils and magnets in one cycle were calculated as shown in Fig. 3.11. It can be seen that two peak values of core loss and eddy current loss appear in one cycle. It also can be found that the times at which the core loss and eddy current loss reach maximum are close. To calculate the average core loss and additional current loss in one cycle, instantaneous loss was integrated over time and the value was then divided by the period. The average core loss

is 0.25 W and the average additional eddy current loss is 0.04 W at a stroke of 11 mm.

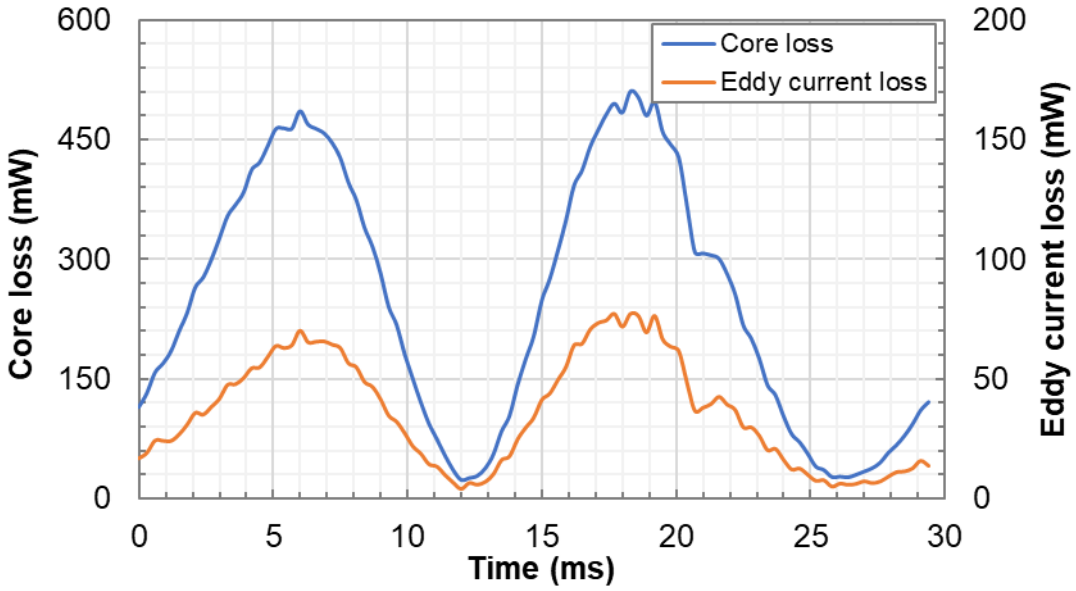

Fig. 3.11 Core loss and additional eddy current loss of coils and magnets in one cycle from the FEA model with a stroke of 11 mm

Copper losses P_{cu} can be easily calculated from the ohmic losses as follows:

$$P_{\mathrm{cu}} = I^2 \cdot R \tag{3.14}$$

where I is the RMS value of current and R is the total resistance of windings.

The pie charts in Fig. 3.12a and Fig. 3.12b shows the shaft power and losses breakdown of the moving magnet linear motor at a stroke of 9 mm and 11 mm respectively. At a stroke of 11 mm, shaft power accounts for 84.7% of the input power, the copper loss percentage is 13.5% while the sum of the rest losses is 0.99%. The majority of loss occurs at windings and transfer into heat dissipated into ambient. It can be seen that the increase of the proportion of copper loss is the main reason for the motor efficiency decrease.

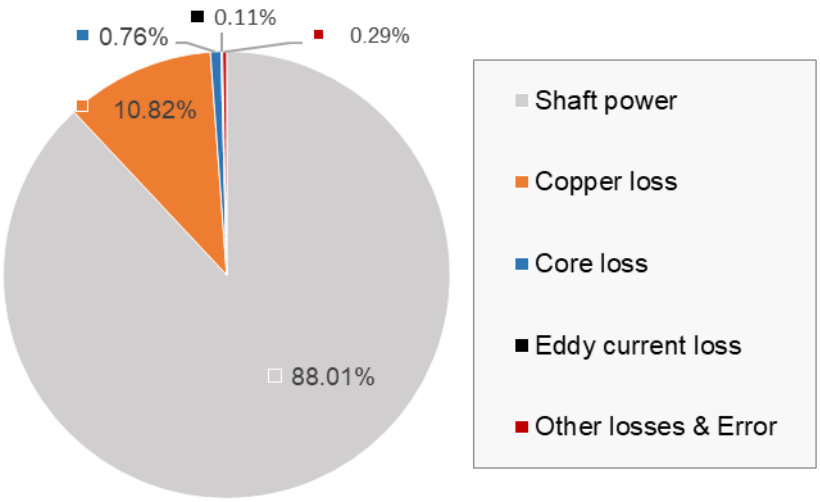

(a)

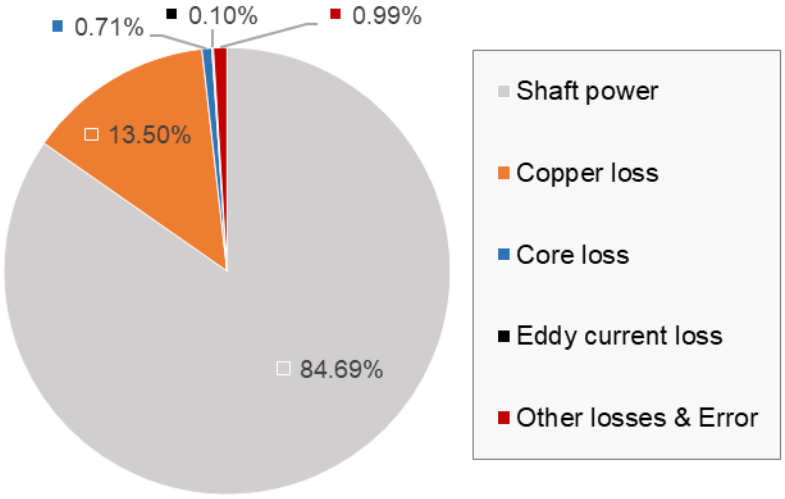

(b)

Fig. 3.12 Shaft power and losses for the moving magnet linear motor with a fixed pressure ratio of 2.0 (a) a stroke of 9 mm (b) a stroke of 11 mm

3.4 Motor Efficiency

Motor efficiency can be calculated as follows:

$$\eta = \frac{P_s}{P_i} = \frac{\int F dv}{P_i} \tag{3.15}$$

where P_s and P_i are shaft power and input power, F denotes shaft force, and v represents velocity of motion.

Motor efficiencies at various strokes are shown in Fig. 3.13. With the increase of stroke, the motor efficiency shows decrease trend. When the stroke varies from 9 mm to 12mm, the motor efficiency decreases from 0.88 to 0.83 with a fixed pressure ratio of 2.0. The input power is 19.3 W at a stroke of 9 mm, 28.0 W at a stroke of 10 mm, 35.1 W at a stroke of 11 mm, and 43.5 W at a stroke of 13 mm. The power input increases with stroke as more power is required to drive the piston through a larger stroke, leading to a larger current input and thus higher copper loss. It can also be expected that when the heat load is low, lower stroke is only needed so that the motor efficiency is higher than at full capacity.

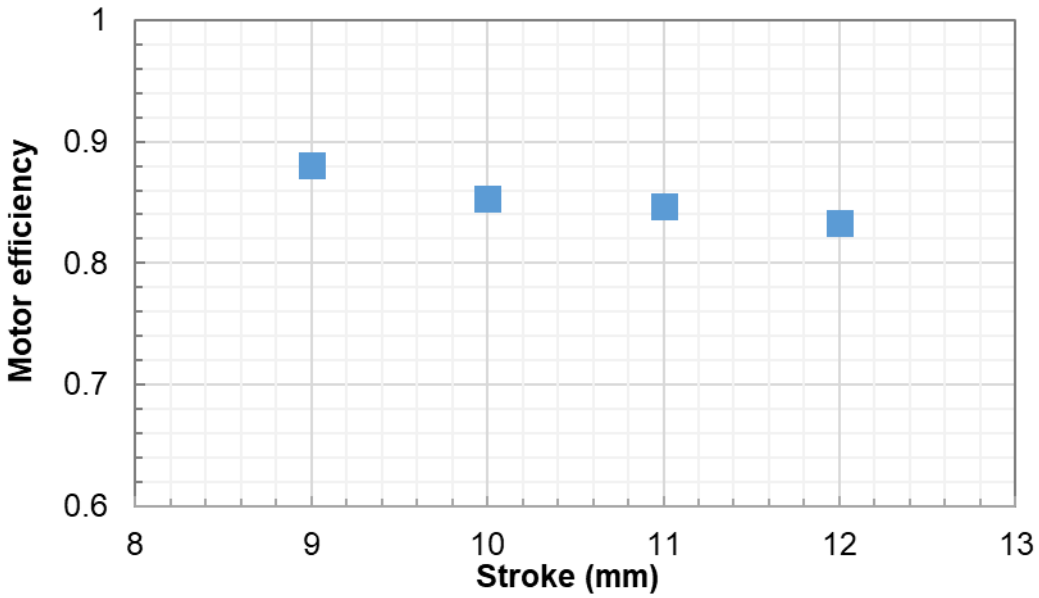

Fig. 3.13 Motor efficiency versus stroke with a fixed pressure ratio of 2.0 for the moving magnet linear motor/compressor

3.5 Comparisons with Other Linear Motors

3.5.1 Comparisons with Moving Coil Linear Motor

Comparisons were made between the moving magnet design and moving coil linear motor presented in **[71]** as shown in Table 1. The moving mass of the moving coil linear

motor is only half of the moving magnet linear motor. A low mover mass suggests high frequency oscillation conditions. To make fair comparisons between the two motors, performance of the motors with the same input power of 40 W and sine waveform driving voltage are listed in the table. The THDs of the two motors are similar. The proportions of copper loss for the moving magnet and moving coil linear motor are 14% and 18% respectively. Note that the motor efficiency of the moving coil linear motor reported in **[71]** was calculated with consideration of copper loss only. The actual motor efficiency should be smaller than the reported value with other losses taken into account. The moving magnet design shows a higher motor efficiency than the moving coil design.

Table 3.2 Comparisons between the moving magnet and moving coil design in **[71]**

	Moving magnet	Moving coil
Moving mass (kg)	0.66	0.313
Resistance of motor coil (Ω)	3.5	2.62
Stroke (mm)	11.5	8
THD of current (%)	>50	5.2
Copper loss (W)	5.6	7.1
Motor efficiency (%)	84	82 (only considered copper)
Motor constant (N/A)	31	28.5
CoP	3.56	3.22
Input power (W)	40	40

Dang et al. optimized the parameters of a moving coil motor for linear compressor. The manufactured linear compressor was tested and a maximum motor efficiency of 79.48% was reported **[72]**. It was also reported that the mean motor efficiency for some typical compressors developed for space Stirling-type pulse tube cryocoolers ranges between 74.2% and 83.6% **[73]**. Compared with moving magnet motors, moving coil designs usually needs larger permanent magnets. Moreover, for the effective current transmission

from external supply system to the moving coils, required components increase the cost and complexity. Moving magnet outperform moving coil motors for the application into larger compressors as motor efficiency and moving mass becomes more important. To achieve high motor efficiency, copper loss in particular needs to be decreased. One approach is to use coils of larger diameter, thus enabling smaller resistance. The moving mass and resonant frequency of a moving magnet was hardly affected, however increasing the size of coils results in the larger moving mass. Larger moving mass is undesirable for the design of a linear motor, especially when high frequency operation is favoured.

3.5.2 Comparisons with Other Moving Magnet Linear Motors

The most widely used tubular design of moving magnet linear motor is shown as Figure 1c. The tubular moving magnet linear motor is composed of an inner stator, an outer stator with coils placed inside, and moving magnet. LG Electronics who licensed the technology from Sunpower stated that the motor efficiency exceeds 90 %, and the LG linear compressor using the tubular moving magnet linear motor is 20-30% more efficient than the conventional compressors **[73]**. Due to its radial magnetic field, both the laminations of the inner and outer stators should be stacked radially to reduce core loss, which brings manufacturing challenges. The motor characteristics have not been reported in details. To align he piston within the cylinder, the LG linear compressor adopted the tubular moving magnet design and large amounts of coil springs. The overall design appears to be bulky. Wang et al. **[64]** designed a tubular low-stroke moving magnet linear motor for linear compressor with quasi-Halbach magnetized sintered NdFeB magnets. Maximum motor efficiency of 93% was reported when operated at a stroke of 10 mm at 44.5 Hz, and the motor efficiency decreased to 89% with frequency increased to 46 Hz. However, part load results have not been reported that could be compared to the present rectangular design. A moving magnet design was also proposed by Bijanzad et al. **[29, 30]**, who demonstrated that the motor efficiency approached 89% when operated under low load condition using

nitrogen as working fluid. However, motor efficiency decreased from 0.79 to 0.7 with input power increasing from 30 to 50 W using R600 as working fluid.

The present moving magnet design provides fair motor efficiency over wide range of strokes, particularly at part load. The magnet assembly in particular is very simple and robust, but nonetheless, the magnet utilisation is good with a 0.66 kg magnet and a designed maximum power of 100 W, and efficiency over 85% is readily attained. The motor presented in this work has three magnets and four cores but other combinations are possible as long as the number of cores is one greater than the number of magnets.

3.6 Conclusions

In this chapter, the finite element analysis model of the moving magnet linear motor was presented. The static results show that saturation occurs with the increase of current, the saturation current reduces as absolute armature displacement increases. A force constant of 31N/mm was obtained at a displacement of ±4mm. The comparisons were made between static motor force from simulation and from measurement. The average error is below 10%.

Transient motor force, motor loss and motor efficiency were also computed in the finite element analysis model. The transient motor force in one cycle is in sinusoidal waveform, and the shaft force peaks at zero displacement. Motor efficiency decrease with the increase of stroke, as a higher input power is required to drive the piston through a full cycle. A larger power input leads to larger loss due to saturation. From the comparisons between the moving magnet and moving coil linear motors, the moving magnet type is suggested for scaling up in terms of motor efficiency and superior heat dissipation for coils. Overall, motor efficiency above 85% is readily attained for the moving magnet linear motor. Moreover, motor efficiency above 90 % can be easily obtained at part load which is very attractive for refrigeration systems which are mostly operated at part load. The design of the linear motor could be optimized further for compactness and higher

efficiency.

Conventional linear motor has moving assembly oscillate about the datum position which means the axial clearance and dead volume vary with compressor stroke. However, in order to deliver more mass flow rate and thus cooling capacity of the refrigeration system with higher volumetric efficiency, it is suggested to keep the axial clearance and dead volume at minimum. Keeping axial clearance volume at low values will have effect on the motor performance (efficiency and saturation point etc.) and also compressor efficiency which will be presented in next chapter.

Chapter 4 Performance of the Linear Compressor with Small Clearance Volumes

4.1 Piston Offset and Clearance

The time-averaged mass flow through radial clearance seals between piston and cylinder leads to offset from the datum piston position, which will reach a certain value for a specified operating condition as piston offset is constrained by mechanical spring and magnetic spring. Early investigations carried out by Cadman and Cohen **[10]** showed that free piston operation of a linear compressor resulted in piston drifting from its datum position, which posed a challenge to modelling efforts and limited the practical application particularly for high pressure ratios. Pollak et al. **[128]** investigated one-dimensional, nonlinear dynamics of the piston and electrical systems and confirmed such confounding effects. Spoor and Corey **[129]**derived simple expressions for the time-average mass flow through a clearance seal and predicted the piston offset by assuming that the piston was acting against enclosed volumes on either side. Bradshaw **[32]** studied the piston offset varying with clearance volume and stroke to diameter ratio, and the results indicated that piston offset decreased with the clearance volume and increased with the stroke to diameter ratio. Zou et al. **[130]** employed a formula (from Choe and Kim **[131]**) to calculate the piston offset and validated this method by experiments.

Controlling the pressure in the compressor body via bleed flow of refrigerant from compressor body is one of the most practical ways to control piston offset in linear compressors. Reed et al. **[132]** employed a manually adjusted needle valve to allow the gas being pumped into the body to return into cylinder to counteract piston offset. Liang et al. **[133]** developed a PID (Proportional–Integral–Derivative) control system for piston offset using a solenoid operated valve to adjust bleed flow from compressor body to suction line. Operation of the linear compressor using nitrogen with a fixed clearance of 0.8 mm was compared with a zero offset operation but no refrigeration performance was

reported.

Some work has been conducted to study the impact of clearance/dead volume on the performance of linear compressor. Lee et al. **[134]** modulated cooling capacity by changing the top dead centre (TDC) of linear compressor. It was concluded that neither experimental nor theoretical compression efficiency was dominated by the varied dead volume as both the generated cooling capacity and the electrical power input decrease at the same ratio. Bradshaw et al. **[25]** analysed the influence of dead volume on linear compressor performance. The results showed that the overall isentropic efficiency of the linear compressor remained relatively unaffected by an increase in dead volume up to a certain point. However, dead volume mentioned above was changed by adjusting stroke only without taking piston offset into account.

When linear compressor is operated with an offset of 0 mm, the axial clearance varies with the stroke of piston. For operation with a certain clearance, the piston offset needs to be varied with stroke. There were few studies carried out to study the influence of different operation scheme (operation with various clearances and an offset of 0 mm) on the refrigeration performance and motor efficiency. Fig. 4.1 shows the schematic of the linear compressor when mean oscillating position of the piston is different from the datum position. The distance between the mean oscillating position defines piston offset. A negative offset is shown in Fig. 4.1, where mean oscillating position is on the left of datum position. Piston in solid line represents piston at top dead centre and piston in dash line represents piston at bottom dead centre. Clearance is denoted by the distance between the top dead centre and the cylinder head.

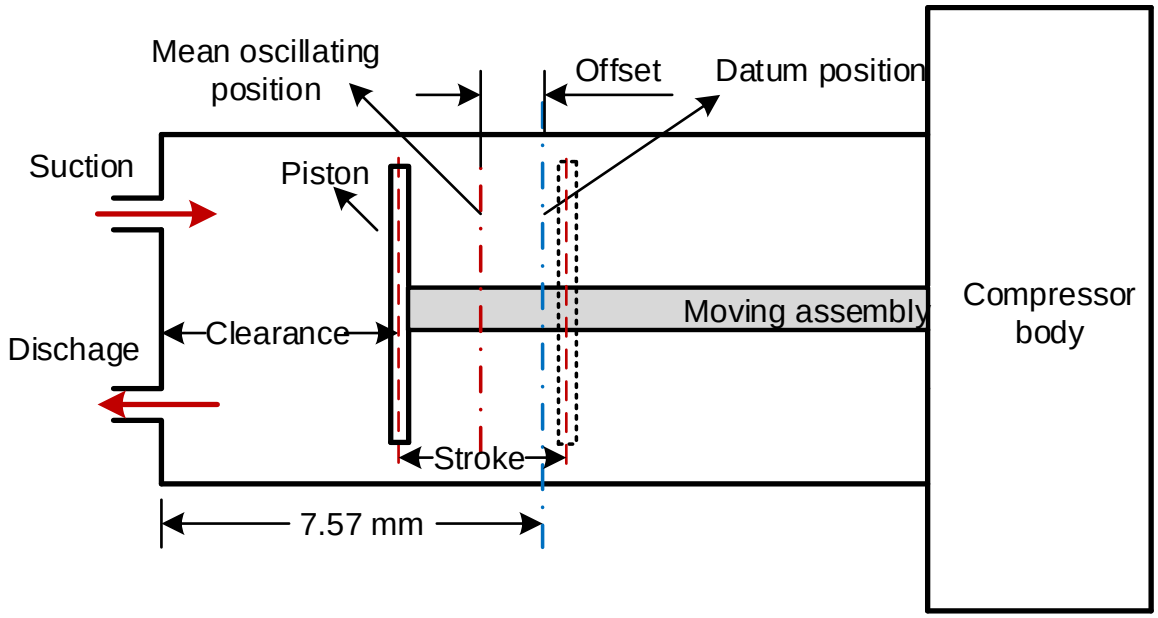

Fig. 4.1 The schematic of the linear compressor with a negative position offset

The clearance is defined as the distance between the top dead centre of piston and the cylinder head. Since a negative displacement means towards the cylinder head from the datum position, the clearance can be expressed as

$$c = 7.57 - \frac{s}{2} + d \tag{4.1}$$

where c is the clearance, s is the stroke and d is the piston offset from the datum position.

Fig. 4.2 shows the piston offset plotted against the clearance at a stroke of 12 mm, 12.5 mm and 13 mm. As clearance decreases, piston offset moves further away from datum position towards cylinder head. It is easier to achieve a smaller clearance with a higher pressure ratio and a larger stroke. To operate with a clearance of 0.7 mm, a piston offset of -0.87 mm, -0.62 mm and -0.37 mm need to be maintained for a stroke of 12 mm, 12.5 mm and 13 mm respectively.

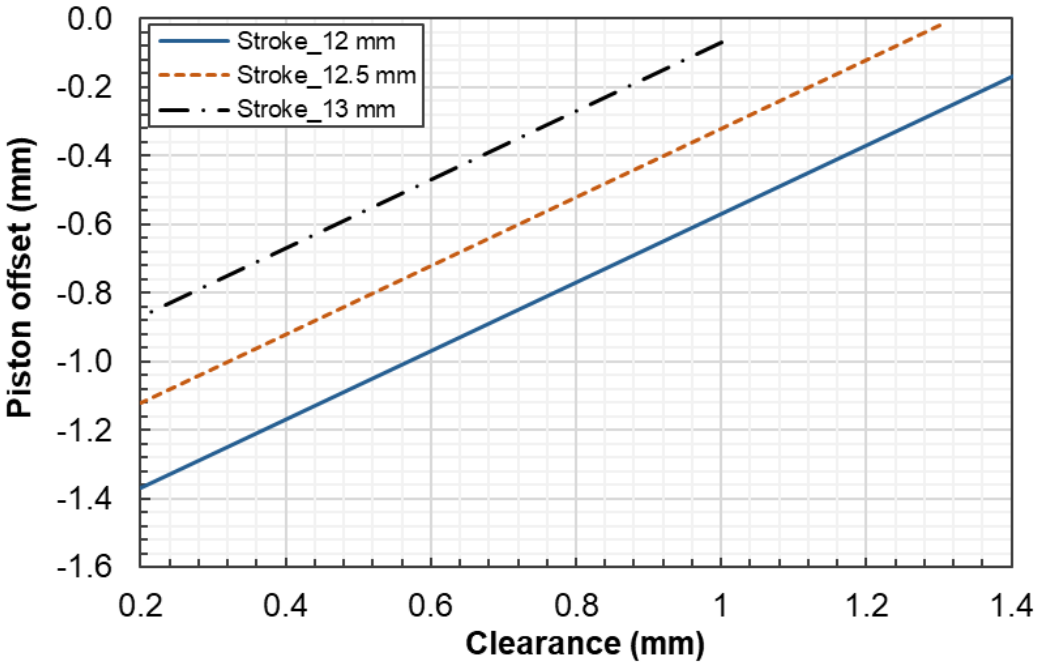

Fig. 4.2 Piston offset against clearance for various strokes

Fig. 4.3 shows the measured displacement with a stroke of 12 mm with a clearance of 0.8 mm and an offset of 0 mm. An offset of -0.77 mm can be observed from the sinusoidal displacement with a clearance of 0.8 mm.

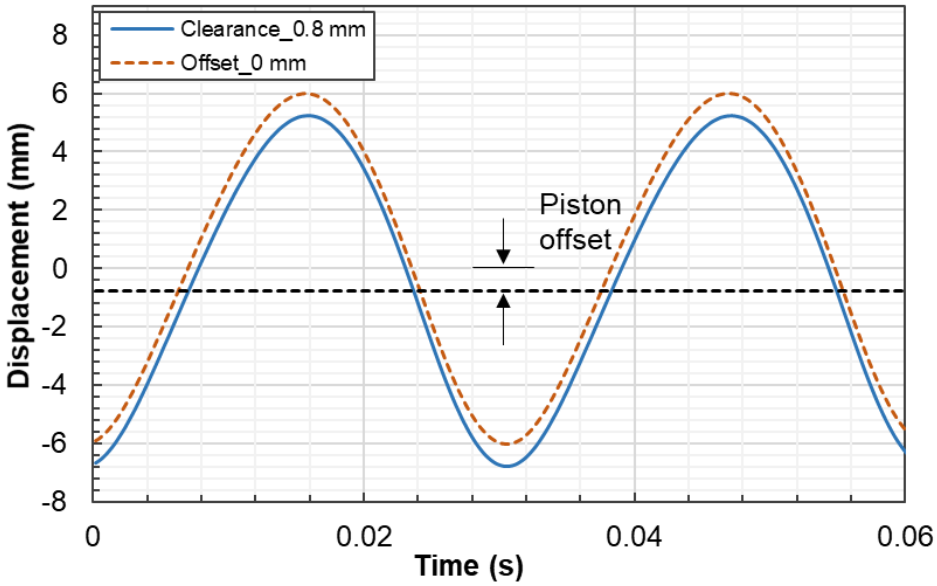

Fig. 4.3 Measured displacement with a stroke of 12 mm for a clearance of 0.8 mm and an offset of 0 mm

4.2 System Performance Experiments and Test conditions

4.2.1 Experimental Procedures

Performance tests were conducted with R1234yf as working fluid to show the performance of the linear compressor in a vapour refrigeration system. During all the tests, the linear compressor was operated at resonant frequency to give the least losses and highest efficiency. The resonance was calculated in the LabVIEW as presented in section 4.3 and result was displayed on the front panel. Operating frequency was then adjusted accordingly manually.

Before experiments, the compressor body was heated up to 45 °C to eliminate liquid refrigerant in the compressor. Multiple parameters were required to be monitored and adjusted during tests such as the stroke and piston offset of the linear compressor, operating frequency, pressure ratio, and condenser temperature. Refrigerant state at the evaporator outlet also needs to be checked to avoid liquid refrigerant flowing to compressor. Computer and LabVIEW program, oscilloscopes and DC power supply for the solenoid valve at fuel injector, and NI multifunction I/O devices were switched on. Meanwhile, Whether the displayed signals (compressor current, voltage, displacements, and control outputs) on LabVIEW front panel and oscilloscopes were zeros needs to be checked one by one. When all preparations were done, the green button on the panic box was switched on so the main power supply circuit was connected. The set point of the compressor stroke was gradually increased to target stroke with a step size of 0.2 mm. The small step increment was set for the safety consideration. The target piston offset was then set in LabVIEW. Both the compressor stroke and piston offset was adjusted automatically with PID controllers implemented in LabVIEW. However, due to the possible overshoots during adjustments, careful attention needs to be paid to real-time axial clearance (which is determined by compressor stroke and piston offset), especially for test conditions with large strokes. The compressor stroke needs to be decreased immediately if the axial clearance exceeds set value.

The pressure ratio and system temperatures also need to be adjusted when the target stroke and piston were reached. The pressure ratio was manually adjusted by varying the lift of the needle valve. As pressure ratio is dependent of other system conditions, the pressure ratio needs to be monitored and adjusted during operation. Temperature of the water-cooled condenser was controlled by the water flow rate from the tab. Power input of the electric heater placed in evaporator was varied to adjust the evaporator outlet temperature. When the system settled at the designed test conditions, data recording was completed after pressing the 'Write data?' button and data files were saved to predefined directory.

After data were collected and saved, the variac electric heater was shut down. The compressor stroke was gradually decreased below 1 mm. The 'No stroke' button was pressed to output zero power and the red button on the panic box was switched on to cut off the power supply circuit. Finally, other instruments were switched off one by one when all test were done.

4.2.2 Test Conditions

A series of measurements were conducted at different pressure ratios, strokes and clearances using R1234yf which was readily available. R1234yf is also considered as alternative to R134a which is being phased out in the EU. Table 4.1 lists the test conditions for the tests on the performance with small clearance operation. The driving frequency of the voltage signal was kept at the resonant frequency. For the performance tests with small clearance operation, linear compressor was operated at clearances of 0.4-0.8 mm and zero offset for various strokes. It is worth noting that strokes smaller than 11 mm were not considered for tests as low clearance could not be achieved when piston offset is small. Table 4.1 Test conditions for the linear compressor with various clearances

Refrigerant	R1234yf
Charge (g)	250
Pressure ratio	2.5, 3.0, 3.5
Compressor stroke (mm)	11, 11.5, 12, 12.5, 13
Compressor clearance/offset (mm)	clearance (0.4, 0.6, 0.8), offset (0)
Condenser temperature (°C)	45
Operating frequency (Hz)	32-38
Suction temperature (°C)	20-30
Ambient temperature (°C)	22

4.3 Resonant Frequency and Compensation Capacitance

4.3.1 Resonant Frequency

As presented in section 3.2.2, the piston- magnets moving assembly can be regarded as a mass-spring damper system. The total spring stiffness of the compressor consists of mechanical spring (flexure spring) k_{m}, gas spring k_{g} and magnet spring k_{ma} which

can be described as

$$k = k_{\mathrm{m}} + k_{\mathrm{g}} + k_{\mathrm{ma}} \tag{4.2}$$

As shown in Table 1, the total moving mass is 0.66 kg and the mechanical spring stiffness is 16.3 N/mm. As has been reported by Pollak et al. **[128]**, for low pressure ratio system, the linearized gas spring force was divided by the stroke of the compressor, which would yield estimated gas spring stiffness in the compression chamber.

$$k_{\mathrm{g}} = \frac{(P_{\mathrm{d}} - P_{\mathrm{s}})A}{S} \tag{4.3}$$

where P_{s} and P_{d} represent suction pressure and discharge pressure respectively, A represents piston area, and S is the stroke of linear compressor (peak-to-peak value of armature/piston displacement).

Magnetic spring force refers to magnetic force without any current excitation. FEA analysis was performed to simulate the magnetic spring force as introduced in section 3.2.2. The magnet spring stiffness can be calculated by the following formula:

$$k_{\mathrm{ma}} = -\frac{F_{\mathrm{ms}}}{x} \tag{4.4}$$

where F_{ms} represents magnet spring force shown in Fig. 3.3, and x represents the armature/piston displacement. Once magnets are away from the central point, magnetic spring force is produced and drives the magnets towards regions of higher flux.

To validate calculation, the resonant frequency for various pressure ratios and strokes was found experimentally. By manually adjusting the driving frequency of the voltage signal in LabVIEW, the frequency at which the simplified motor efficiency reached the maximum was considered to be the resonant frequency for the specific operating point. The simplified motor efficiency was calculated by:

$$\eta = \frac{P - I^2 R}{P} \tag{4.5}$$

where P is the electric power into to the linear motor measured by the power analyser, I is the current measured by the current transducer, R is the total resistance of the windings.

Fig. 4.4 shows the simplified motor efficiency varying with drive frequency at a pressure ratio of 2.0 using helium for various strokes. The resonant frequency for 13 mm, 10 mm, and 6 mm is 39 Hz, 34 Hz, and 32.5 Hz respectively. As the minimum step for adjusting the drive frequency is 0.5 Hz, there is error in resonant frequency from measurements. However, it can be seen that the motor efficiency curve is sufficiently flat for frequencies within 1 Hz difference from the resonant frequency. Therefore, the measured resonant frequency has sufficient accuracy, which can be used to validate the calculations.

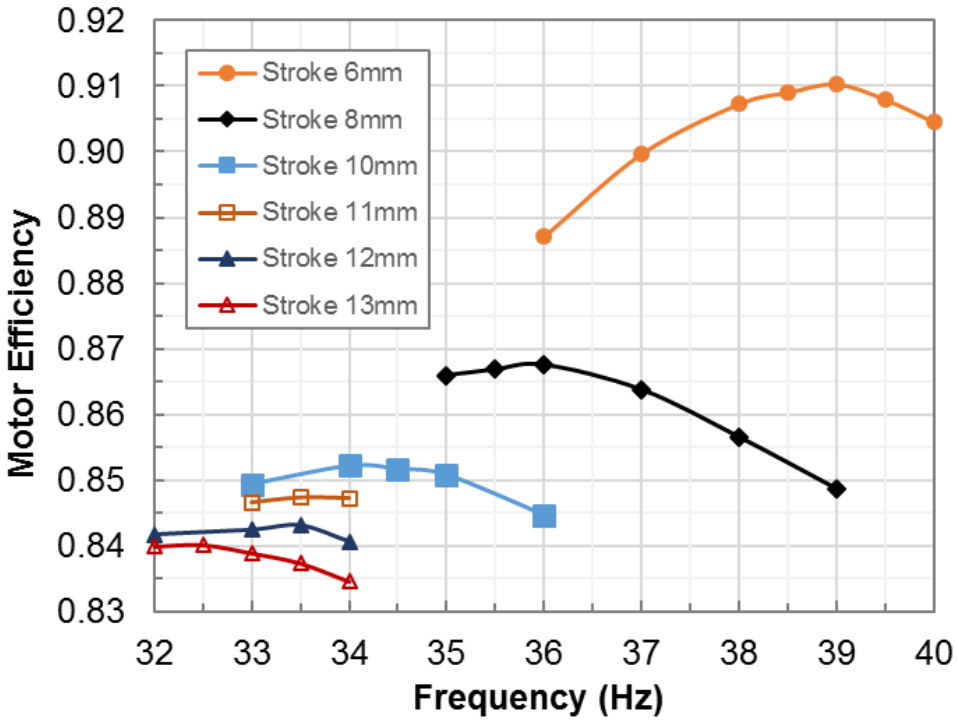

Fig. 4.4 Simplified motor efficiency varying with drive frequency at pressure ratio of 2.0 using helium

Fig. 4.5 shows the comparison of resonant frequency between calculation and measurement at various strokes and pressure ratios using helium. Close agreement has been achieved. The maximum error between the calculated and measured results is only 4.6%. As the drive frequency was adjusted by a minimum step of 0.5 Hz, an error lower

than 1 Hz is reasonable. The change of resonant frequency is mainly induced by the change of gas spring rate. For a fixed pressure ratio, with the increase of stroke, the resonant frequency decreases due to lower gas spring stiffness. The pressure ratio affects the resonant frequency greatly. Larger pressure ratio leads to higher resonant frequency due to higher gas spring stiffness according to Equation 4.2 and 4.4. When the stroke is fixed at 8 mm, resonant frequency increase by about 10% as pressure ratio varies from 1.5 to 3.0. Table 4.2 gives the calculated spring rate for various stroke at a pressure ratio of 3.0. For the design point (pressure ratio of 3.0 and stroke of 13 mm), the gas spring stiffness is 16.78 N/mm, mechanical spring stiffness is 16.3 N/mm, and magnet spring is -1.16 N/mm. Previous work by other researchers **[23]** adopted coil springs to achieve very high mechanical spring stiffness. This can have two effects: resonant frequency can be dominated by the mechanical spring so that the range of drive frequency is narrow; piston offset will be much smaller. However, this is not desirable with respect to size and weight.

Table 4.2 Spring stiffness for various stroke at a pressure ratio of 3.0

Stroke (mm)	Mechanical spring stiffness (N/mm)	Gas spring stiffness (N/mm)	Magnet spring stiffness (N/mm)
8	16.3	26.61	-0.60
9	16.3	23.78	-0.68
10	16.3	21.78	-0.78
11	16.3	19.85	-0.89
12	16.3	18.12	-0.98
13	16.3	16.78	-1.16

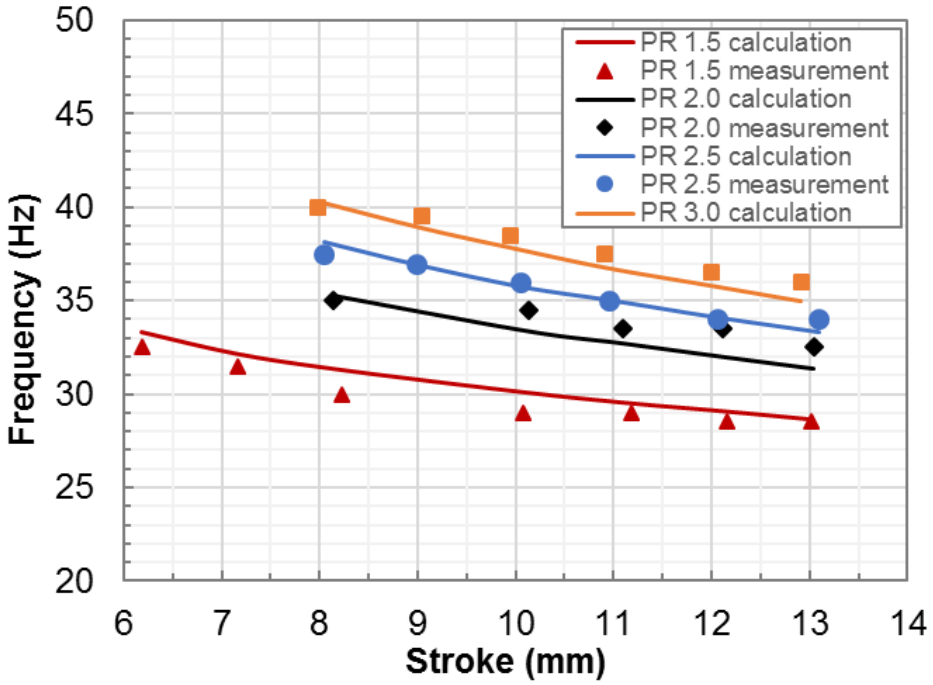

Fig. 4.5 Comparison of resonant frequency between calculation and measurement at different strokes and pressure ratios (PR) using helium

4.3.2 Compensation Capacitance

In order to correct power factor, a capacitor is usually employed in series with the linear motor. Fig. 2.6 shows the electric circuit of the linear motor. When it is operated at resonant frequency, the voltage of the impedance associated with motor force will be in phase with current as displacement leads current 90º, so the circuit then becomes a typical RLC circuit. The matching capacitance is dependent on the inductance and drive frequency as follow

$$C = \frac{1}{4\pi^2 f^2 \mathrm{L}} \tag{4.6}$$

The inductance of each linear motor is 0.141 H. However, as shown in Fig. 10, resonant frequency varies for different operation conditions.

Fig. 4.6 shows the matching capacitance for various strokes and pressure ratios. It can be seen that the trend of capacitance is opposite from that of resonant frequency. With the

increase of stroke or decrease of pressure ratio, the required matching capacitance increases. When a stroke of 12 mm is fixed, the required matching capacitance increases by 72 μF when pressure varies from 1.5 to 3. For a pressure ratio of 2.0, the matching capacitance varies from 144 μF to 182 μF. The capacitor needs to be adjustable for a large range if it is expected to reduce the voltage input under various test conditions particularly when the gain of the AC power amplifier is not sufficiently high.

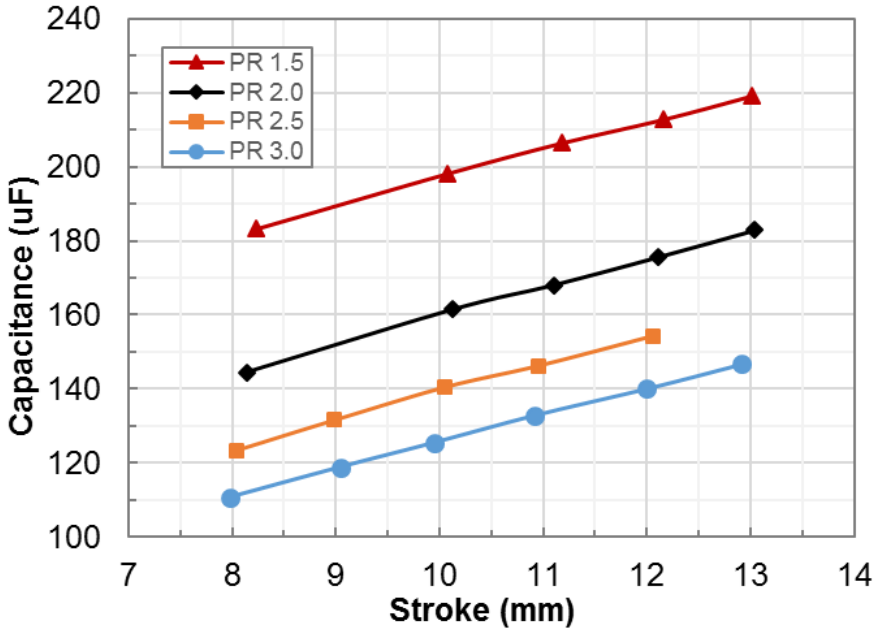

Fig. 4.6 Capacitance compensation varying with stroke at pressure ratios of 2.5 and 3.0 using helium

4.4 Performance with Clearance Operation

4.4.1 Mass Flow Rate and Evaporator Temperature

Fig. 4.7 shows the measured main mass flow rate for strokes of 10-13 mm and pressure ratios of 2.5-3.5 when operated at an offset of 0 mm and a clearance of 0.8 mm. Mass flow rate increases with stroke and decreases with pressure ratio. The mass flow rate of operation with a constant clearance is larger than the mass flow rate of operation with an offset of 0 mm. Generally clearance of 0.8 mm gives higher mass flow rate than offset of 0 mm. When the linear compressor is operated at a stroke of 12 mm and a pressure ratio of 2.5, the mass flow rate is about 22% higher than the operation with an offset of 0 mm.

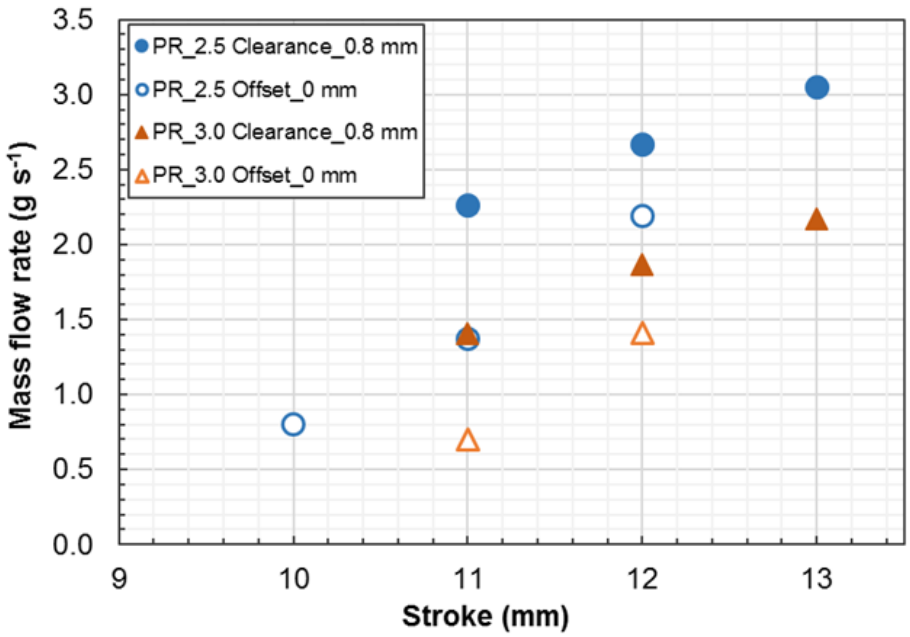

Fig. 4.7 Mass flow rate against various strokes and pressure ratios (PR) when operated at offset of 0 mm and a clearance of 0.8 mm

The evaporator temperature against the stroke with pressure ratios of 2.5-3.5 is plotted in Fig. 4.8. The difference of the evaporator temperature between operation with a clearance of 0.8 mm and offset of 0 mm is small. The maximum difference is only 1.4 °C when operated at a stroke of 11 mm and a pressure ratio of 3.0, which can be attributed to the thermocouple accuracy (1.5 °C). Therefore, the subsequent parameters can then be used for comparison between operation with various clearances and an offset of 0 mm.

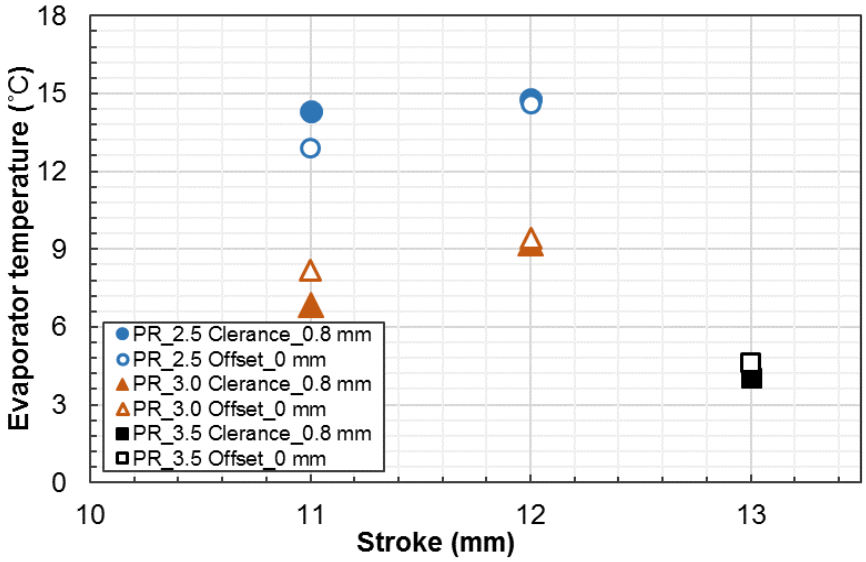

Fig. 4.8 Evaporator temperature for various strokes and pressure ratios when operated at an offset of 0 mm and a clearance of 0.8 mm

4.4.2 Volumetric Efficiency

The theoretical volumetric efficiency of positive displacement compressor is given by

$$\eta_{\mathrm{t}} = 1 - CL[\left(\frac{P_{\mathrm{d}}}{P_{\mathrm{s}}}\right)^{\frac{1}{\mathrm{n}}} - 1] \tag{4.7}$$

where P_{s} and P_{d} represent suction pressure and discharge pressure respectively, A represents piston area, n is polytropic index, and CL is clearance ratio which is the ratio of clearance volume V_{c} to swept volume V_{s} as follow

$$CL = \frac{V_{\mathrm{c}}}{V_{\mathrm{s}}} = \frac{7.57 - \frac{S}{2} + d}{S} \tag{4.8}$$

Heat transfer loss during suction, friction loss with wall, seal leakage and imperfect nurture of valve limit the actual mass flow rate. The experimental volumetric efficiency can be calculated as follow

$$\eta_{\mathrm{e}} = \frac{\dot{m}\mathrm{R}_{\mathrm{g}}T_{\mathrm{s}}}{S\mathrm{A}fP_{\mathrm{s}}} \tag{4.9}$$

Theoretical volumetric efficiency for an offset of 0 mm and various clearances (0.4 mm,

0.6 mm and 0.8 mm) at a pressure ratio of 3.5 is shown in Fig. 4.9. Theoretical volumetric efficiency for fixed clearance operation is much higher than operation with an offset of 0 mm. The smaller the clearance, the higher the theoretical volumetric efficiency is. The clearance ratio becomes smaller when operated with constant clearances. For operation with an offset of 0 mm, theoretical volumetric efficiency increases significantly with stroke while theoretical volumetric efficiency almost remains the same value when operated with fixed clearances. Reduction of clearance by 0.2 mm leads to an approximate 5% increase of theoretical volumetric efficiency when the pressure ratio is fixed at 3.5.

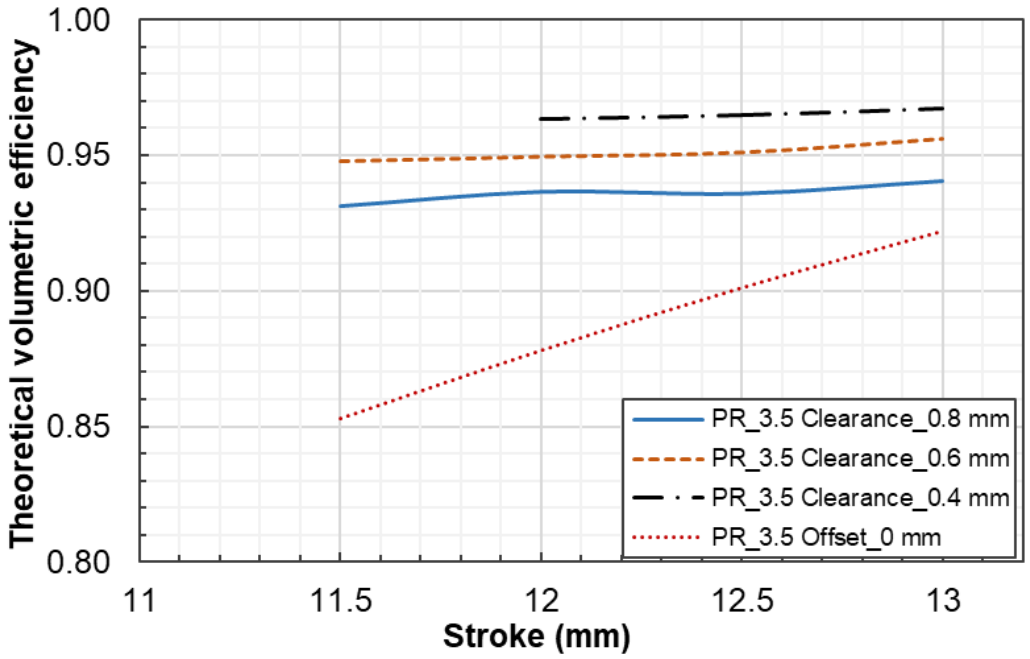

Fig. 4.9 Theoretical volumetric efficiency for a pressure ratio of 3.5 when operated with an offset of 0 mm and a fixed clearance of 0.8 mm, 0.6mm, 0.4 mm using R1234yf

A higher theoretical volumetric efficiency means a larger amount of refrigerant gas can be drawn into cylinder during suction process. The operating frequency is almost same for operation with a certain clearance and an offset of 0 mm when stroke and pressure ratio remain unchanged. The smaller the clearance, the larger the mass flow rate is.

Fig. 4.10 shows experimental volumetric efficiency for an offset of 0 mm and various clearances (0.4 mm, 0.6 mm and 0.8 mm) at a pressure ratio of 3.5. Experimental

volumetric efficiency for fixed clearance operations is higher than operations with an offset of 0 mm. With decreasing clearance, experimental volumetric efficiency increases. When clearance decreases from 0.8 mm to 0.6 mm, an average increase of 4% of experimental volumetric efficiency can be achieved.

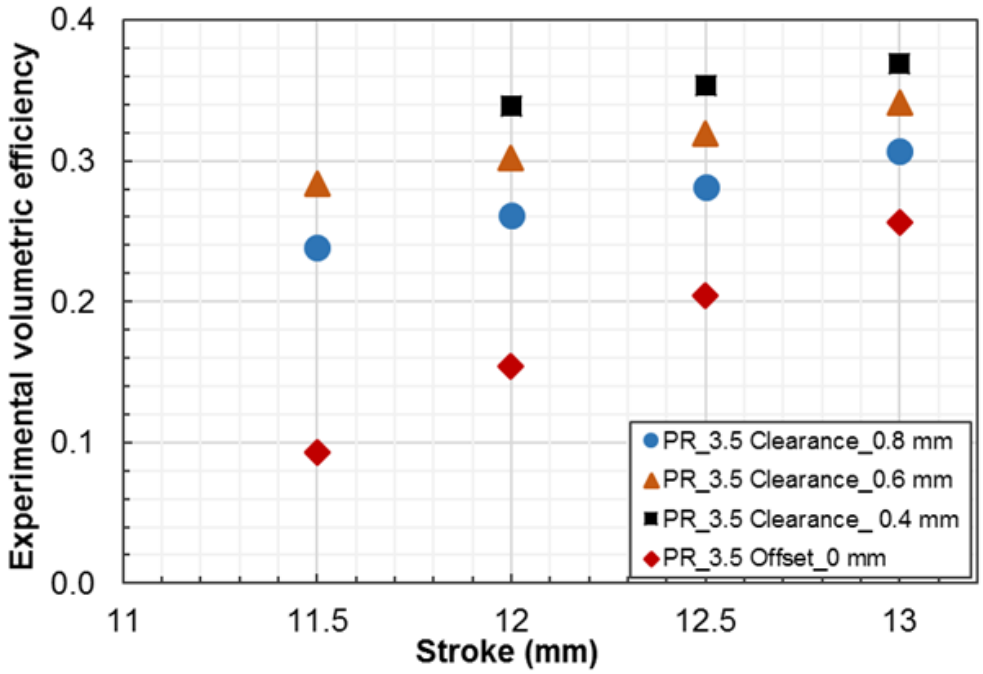

Fig. 4.10 Experimental volumetric efficiency for a pressure ratio of 3.5 when operated at an offset of 0 mm and a fixed clearance of 0.8 mm, 0.6mm, 0.4 mm using R1234yf

4.4.3 Motor Efficiency, Current and Shaft Force

Core loss and eddy current loss restrict the shaft power of the linear compressor. The mechanical frictional loss inside the linear compressor is very small as there is a clearance between piston and cylinder wall. The simplified motor efficiency can be calculated using Equation 4.5.

Fig. 4.11 plots the motor efficiency against stroke for clearances of 0.4-0.8 mm and an offset of 0 mm. Fig. 8 (a) and Fig. 8 (b) show the results for a pressure ratio of 3.0 and 3.5 respectively. It can be seen that motor efficiency when operated with a constant clearance (0.4 mm, 0.6 mm, and 0.8 mm) is significantly lower than operations with an offset of 0mm. With the decrease of clearance, the motor efficiency decreases as well.

This is because when the excitation current exceeds its saturation point, shaft force increases rapidly to achieve specific stroke. When the piston of linear compressor is further away from its datum position, the linear motor saturates earlier. Lower clearance leads to more distance away from datum position thus higher shaft force is required for same stroke. This phenomenon has not been previously reported by other researchers. It can be seen that although mass flow rate increases with decreasing clearance, motor efficiency is sacrificed. Generally with no piston offset, low stroke has higher motor efficiency due to lower copper loss.

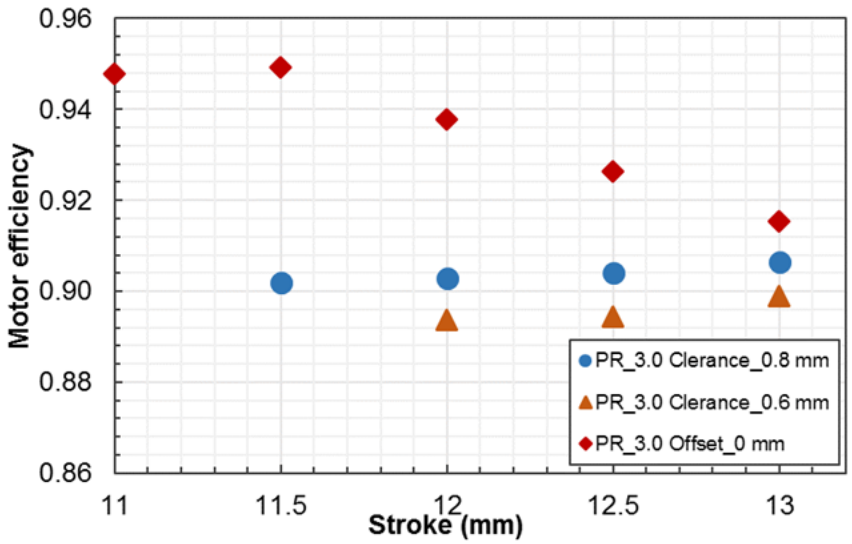

(a)

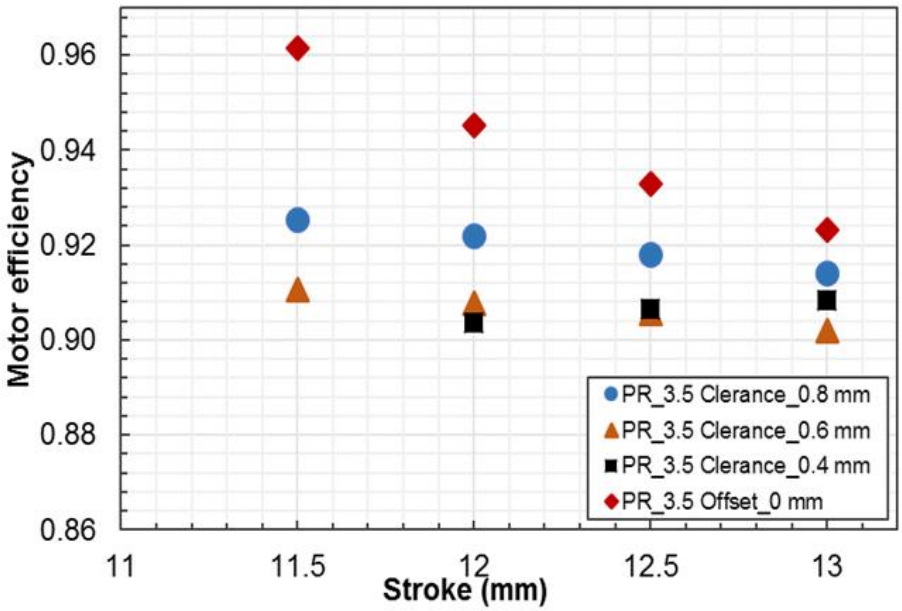

(b)

Fig. 4.11 Motor efficiency when operated at an offset of 0 mm and clearances of 0.8 mm, 0.6 mm, and 0.4 mm using R1234yf (a) pressure ratio 3.0; (b) pressure ratio 3.5

Fig. 4.12 shows the current and interpolated shaft force from the 3D current-displacement-force map shown in Fig. 3.5 for a clearance of 0.8 mm and an offset of 0 mm with a stroke of 12 mm and a pressure ratio of 3.0. Both shaft forces with a clearance of 0.8 mm and an offset of 0 mm are in phase with measured currents owing to resonant operation. The operating frequency for a clearance of 0.8 mm and an offset of 0 mm are 36 Hz and 37 Hz respectively. The excitation current with a clearance of 0.8 mm is much higher than an offset of 0 mm due to earlier saturation of core.

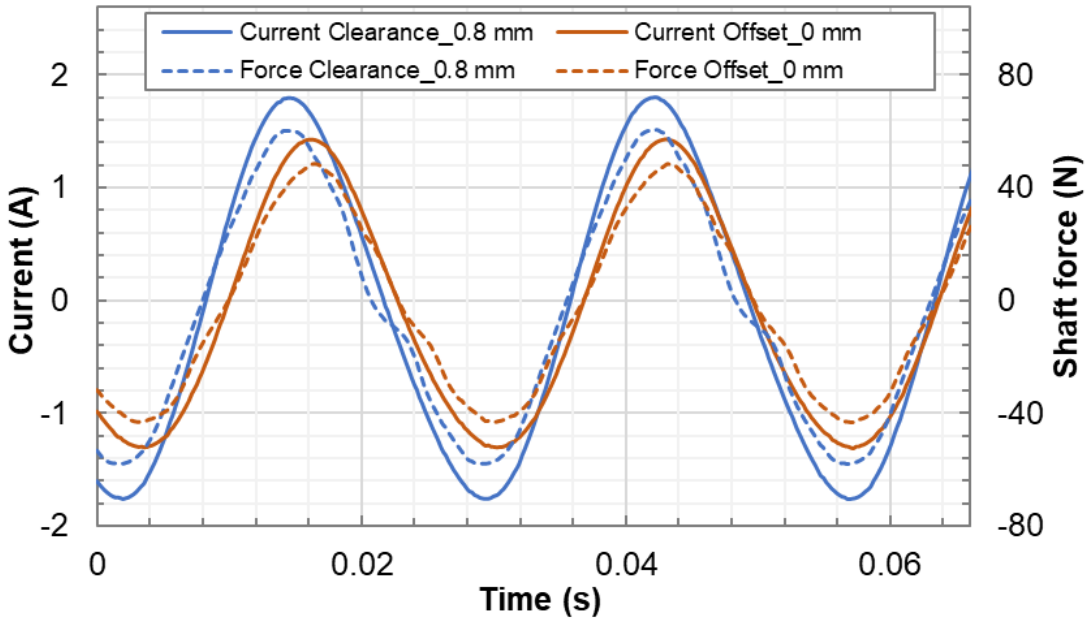

Fig. 4.12 Current and shaft force when operated at an offset of 0 mm and a fixed clearance of 0.8 mm for a stroke of 12 mm and a pressure ratio of 3.0

4.4.4 Cooling Capacity and CoP

Fig. 4.13 shows the cooling capacity plotted against clearance with strokes of 12.5 mm and 13 mm and condenser outlet temperature of 45 °C for various pressure ratios. For operation with an offset of 0 mm (clearance of 1.32 for a stroke of 12 mm, clearance of 1.07 for a stroke of 13 mm), cooling capacity decreases with pressure ratio when stroke

is fixed. This is because mass flow rate decreases with pressure ratio. When operated with an offset of 0 mm, with the increase of stroke from 12.5 mm to 13 mm, cooling capacity for a pressure ratio of 2.5 increases from 93 W to 120 W. With an offset of 0 mm, small clearance (axial) or high stroke will lead to small dead volume so that the volumetric efficiency is high thus high cooling capacity. The cooling capacity increases with decreasing clearance, due to increasing mass flow rate. As shown in Fig. 4.9 (b), when the clearance is reduced from 1.07 mm to 0.4 mm, the cooling capacity for a pressure ratio of 2.5 and a stroke of 13 mm increases from 270 W to 302 W.

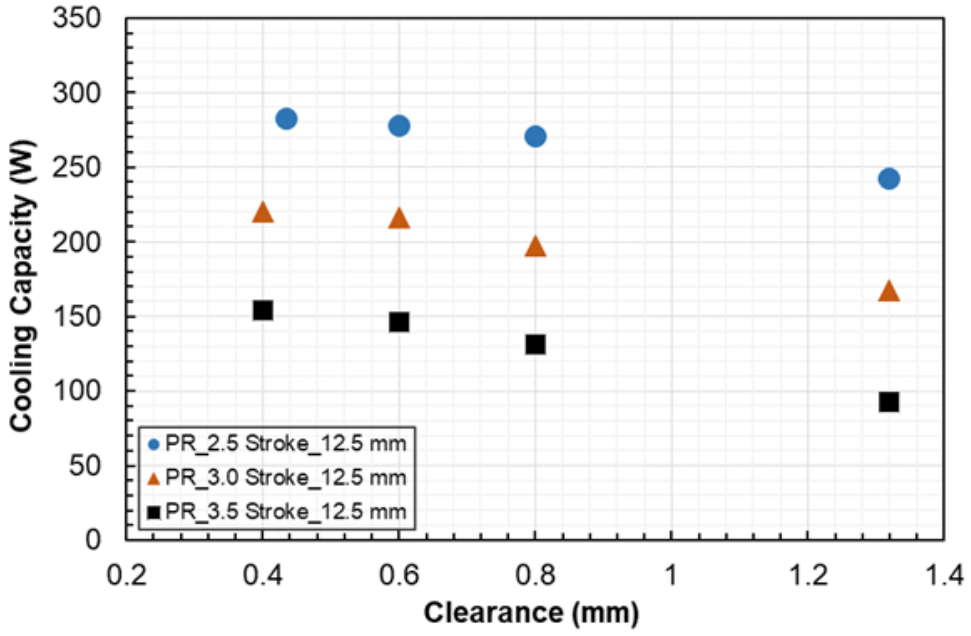

(a)

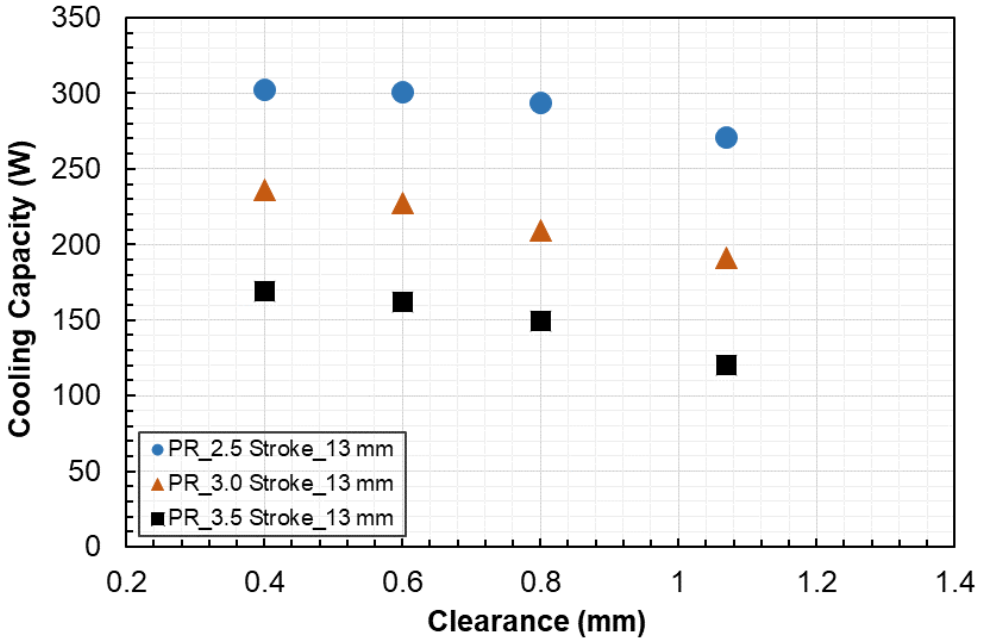

(b)

Fig. 4.13 Cooling capacity for pressure ratios of 2.5-3.5 using R1234yf at condenser outlet temperature of 45 ℃ (a) stroke 12.5 mm (b) stroke 13 mm

The CoP (shown in Equation 2.6) of the refrigeration system can also be re-arranged as:

$$CoP = \frac{h_s - h_{eva}}{h_d - h_s} \eta_m \eta_b \eta_c \tag{4.10}$$

where h_s, h_{eva}, h_d are the enthalpy of suction state, the enthalpy of evaporator inlet state, and the enthalpy of discharge state respectively. η_b and η_c are mechanical efficiency and thermodynamic efficiency respectively.

When the stroke and pressure ratio are fixed, suction and evaporator temperatures remain almost unchanged. Motor efficiency decreases with the decreases of axial clearance. The mechanical efficiency for smaller axial clearance tends to be higher because there is no pumping loss to keep the piston offset at zero. It is difficult to conclude from Eq. (8) how CoP varies with the decrease of axial clearance. For different operating conditions, the factor that dominates the variation of CoP differs.

Fig. 4.14 (a) and (b) show the CoP against clearance for various pressure ratios (2.5, 3.0

and 3.5) with a stroke of 12.5 mm and 13 mm respectively. The CoP increases by 15 % when clearance decreases from 1.32 mm to 0.4 mm with a pressure ratio of 3.5 and a stroke of 12.5 mm. The difference of CoP is smaller for lower pressure ratios and high strokes. At higher stroke, the clearance for operation with an offset of 0 mm is closer to the clearances of 0.4-0.8 mm with small clearance operation. Generally small clearance leads to high CoP for high pressure ratio. It can be concluded that minimizing the clearance will benefit the high pressure ratio operation using linear compressor. When linear compressor is adopted at pressure ratio of over 10 for freezer, minimum clearance operation is recommended. However, different linear motor design may have different motor saturation point. Minimizing the clearance will also require sufficient accuracy of piston position detection to avoid the collision between the piston and cylinder head.

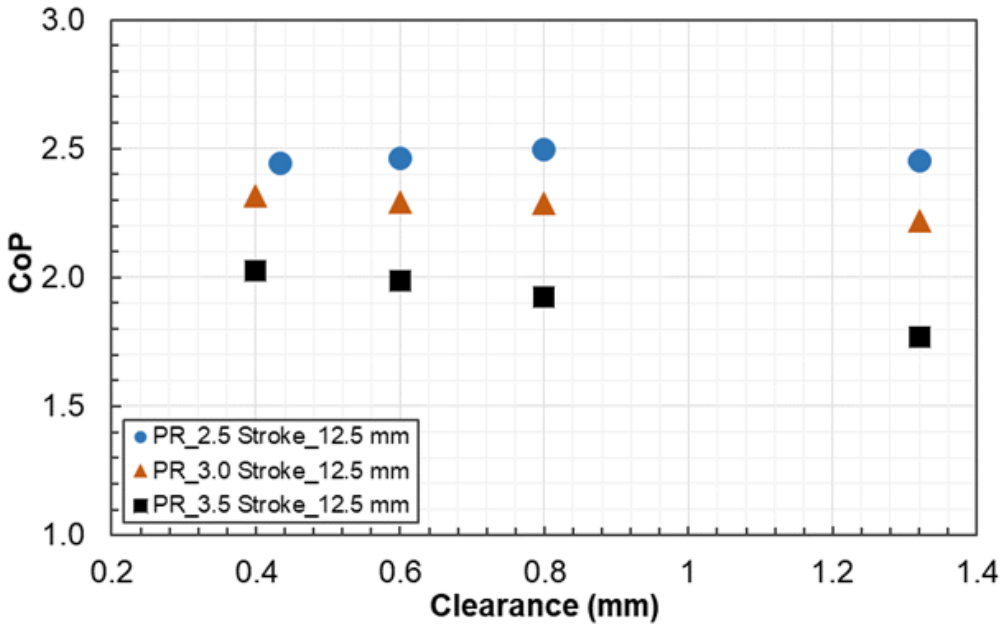

(a)

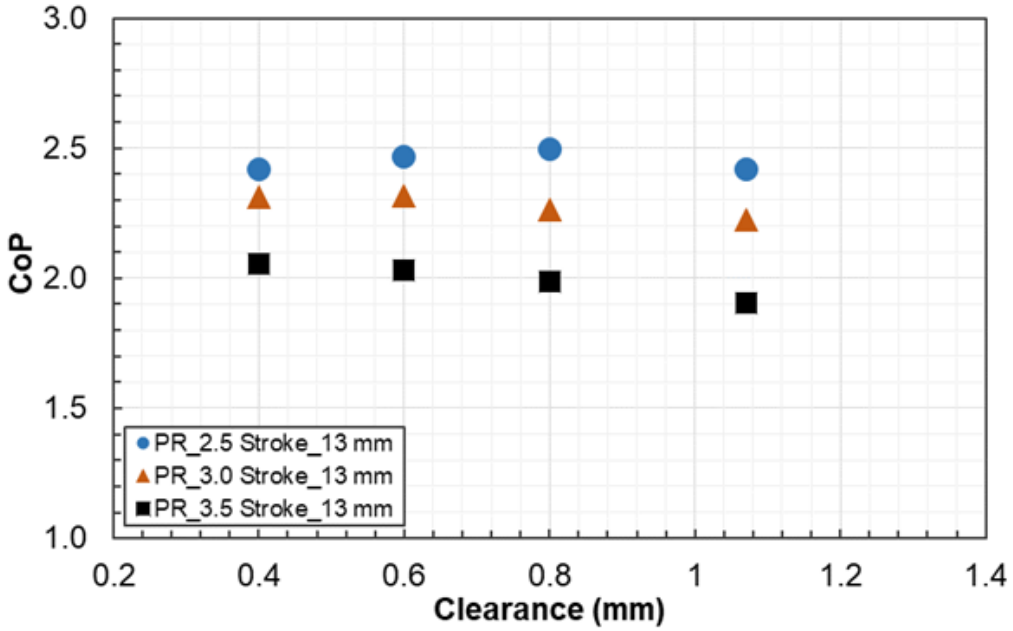

(b)

Fig. 4.14 CoP against clearance for various pressure ratios using R1234yf at condenser outlet temperature of 45 °C (a) stroke 12 mm; (b) stroke 13 mm

4.5 Conclusions

Resonant frequency varies with operating conditions. Linearized gas spring stiffness, magnetic spring stiffness and mechanical spring stiffness can be used for resonance calculation especially when pressure ratio is low. Resonance increases with pressure ratio, but decreases with stroke.

To compare the performance between clearance operation and zero offset operation, linear compressor was operated with various clearances of 0.4-0.8 mm and an offset of 0 mm using R1234yf as refrigerant. Experimental volumetric efficiency increases due to higher mass flow rate with the decrease of clearance. With clearance reduced from 0.8 mm to 0.6 mm, an averaged 4% increase of experimental volumetric efficiency was achieved.

With decreasing clearance, motor efficiency decreases as linear motor saturates earlier when piston is further distant from the datum position. Cooling capacity increases when

the clearance reduces. Cooling capacity increases by 12 % when clearance decreases from 1.07 mm to 0.4 mm with a pressure ratio of 2.5 and a stroke of 13 mm. The benefit of minimizing the clearance is significant for high pressure ratio operation. This is essential for refrigerator/freezer which has much higher pressure ratios.

As mentioned before, the axial clearance is determined simultaneously by piston stroke and piston offset which normally are measured by expensive displacement transducer. To facilitate mass production of linear motor/compressor, sensor-less piston position detection is required for both high efficiency operation and low cost. A sensor-less piston offset detection method was proposed by Liang **[135]**. The sensor-less stroke detection will be introduced in Chapter 5 and 6 using ANN and inductive coil respectively.

Chapter 5 Sensor-less Stroke Detection using Artificial Neural Network

5.1 Sensor-less Detection

For any free-piston engines, stroke is defined by the distance between maximum and minimum displacements. One of the key issues with free-piston machines is the piston position sensing. The motion of piston in a free piston machine is not predefined or constrained, which allows the stroke to be variable. An active control of piston motion is required in order to avoid collision between the piston and cylinder and modulate the power output.

The actual displacement of fast-moving objects in modern industry needs to be sensed without the use of any mechanical contact **[136]**.However, these sensors are very expensive. Existing non-contact displacement sensors are listed as below **[137, 138]**:

(1) Optical sensors, such as interferometers and encoders, provide the best accuracy. However, they are expensive, mechanically fragile, and susceptible to noise as well as demanding large space **[138]**.

(2) Inductive sensors measure inductance variations caused by movement of a flux-concentrating element. They are probably the most versatile of all position sensors, with a wide range of operating characteristics **[139]**.

(3) Capacitive sensors rely on the changing capacitance between two plates, one fixed, the other free to move, to detect changes in linear position of up to 0.4 in. (10 mm). They require somewhat complex support electronics and are very sensitive to changes in environmental conditions such as temperature, humidity, etc. **[138, 139]**

(4) Hall sensors produce output voltages proportional to the strength of a nearby magnetic field generated by a moving magnet. They have relatively poor temperature

performance, but can be effectively used for short-range position sensing where cost is most important and temperature is not an issue **[139]**.

Advancements in digital electronics and improvements in the hardware performance of controllers have given rise to many sensor-less observations of the piston position in free-piston machines. Piston position can be detected by integrating back electromotive force (EMF) directly **[103]**, and some algorithm were employed to compensate DC offset in the back-EMF calculated from the measured motor current and voltage **[98-101]**. Efforts in this area also include an external self-sensor circuit that achieves the estimation of piston stroke by measuring voltage and current applied into the linear motor **[102]**. However, all these works assume that equivalent resistance, equivalent inductance and magnetic force constant of linear motors are invariable., Observers for piston stroke have also been developed **[105, 106]**, but many parameters need to be identified and accuracy were affected by the modelling of electrical and mechanical models. The stroke can detect using inductive coils as reported by Liang et al. **[135]** but an accurate value of mutual inductance between the main coil and the inductive coil was required.

5.2 Artificial Neural Network

Development in artificial intelligence technologies provides an alternative forecast approach of precise and accurate results **[140]**. An artificial neural network is the piece of a computing system designed to simulate the way the human brain analyses and processes information. It is the foundation of artificial intelligence (AI) and solves problems that would prove impossible or difficult by human or statistical standards. ANNs have self-learning capabilities that enable them to produce better results as more data becomes available. Instead of using complex rules and mathematical routines, artificial neural network (ANN) is able to learn the key information patterns within a multi-dimensional information domain **[141]**.

Since the 1990s, the applications of neural network in electrical machines have appeared

[142]. The reported prediction results using ANN were impressive in terms of accuracy **[143, 144]**. In **[145]** and **[146]**, an ANN model was employed for rotor speed estimation with offline training and online training respectively. ANN was employed to estimate the rotor position in a switched reluctance motor through measurement of the phase flux linkages and phase currents **[147]**. Kim et al. **[135]** estimated rotor speed and fed it back into the speed control loop to achieve sensor-less speed vector control.

Application of ANN into conventional compressor has been performed by Cortés et al. **[148]** to optimize operating conditions related to compressor performance. A feed-forward neural network with one hidden layer was employed and trained using Levenberg–Marquardt learning algorithm. Performance map of an axial compressor was predicted with a three-layer back propagation neural network **[149]**, which was trained with Levenberg-Marquardt algorithm. Good agreements were found between the predictive results from the ANN models and experimental results. Ghorbanian and Gholamrezaei **[150]** compared various artificial neural network, such as general regression neural network, radial basis function network, multilayer perceptron network, and a modified technique based on general regression neural network, in reconstructing compressor performance map. It was concluded that multilayer perceptron network technique is preferred when a good accuracy needs to be assured for any operating conditions. Sanaye et. al **[151]** presented an ANN based thermal modelling of a rotary vane compressor. Output parameters such as mass flow rate of refrigerant, discharge temperature, and power consumption of the compressor were predicted with mean relative errors ranging from 2.79% to 7.36%. However, there is no ANN model carried out for detecting the stroke in linear compressors, and very few works can be found in literature regarding the stroke estimation using ANN method in other free-piston machines.

5.3 ANN based Stroke Prediction

5.3.1 Stroke Prediction Approach

Fig. 5.1 shows the schematic of data processing and neural network training and testing. Although measured current, voltage and displacement signals appear to be sine waves, the waveforms cannot be described with one basic sine function, which means harmonics exist in the sampled signals. Fast Fourier transform (FFT) analysis was conducted to extract harmonic terms from sampled current and voltage. The harmonic terms were then fed into the ANN model as inputs. The targets of the ANN model are strokes that were calculated based on sampled displacement. During the training processing, the outputs of the ANN model were passed backward for training. Harmonic term independency was studied by comparing six cases with different number of harmonic items as inputs to the ANN model.

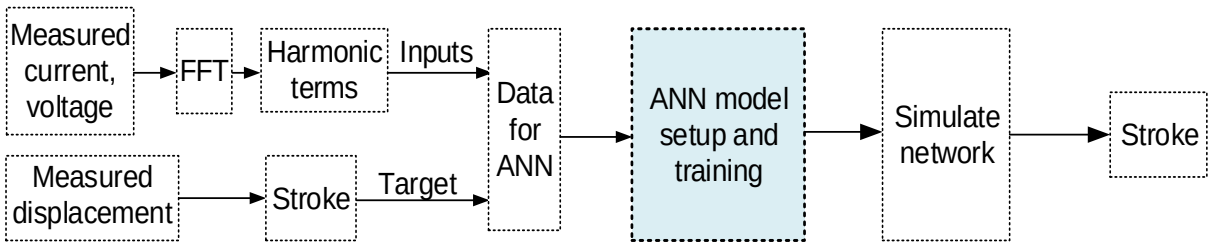

Fig. 5.1 The approach of the ANN based stroke prediction

5.3.2 Test Conditions

ANN model requires large volumes of data for training. A number of tests that cover a wide range of operating conditions were carried out in a refrigeration system driven by the oil-free linear compressor. Current, voltage and displacement signals were measured and recorded for the training and testing of the ANN model. Table 5.1 lists the test conditions for the linear compressor in refrigeration system. 542 tests were conducted with various strokes from 6 mm to 13 mm. The driving frequency of the voltage signal was kept at the resonant frequency. Linear compressor was operated at clearances of 0.4-0.8 mm and zero offset for various strokes. It is worth noting that strokes smaller than 11 mm were not considered for tests, as low clearance could not be achieved when piston offset is small.

Table 5.1 Test conditions of the refrigeration system

Refrigerant	R1234a, R1234yf, R152a
Pressure ratio	2.0, 2.5, 3.0, 3.5
Compressor stroke (mm)	6-13
Operating frequency (Hz)	26-35

5.4 FFT Analysis and ANN Model

5.4.1 FFT Analysis and Signal Processing

The recorded current and voltage are time series in steady state. Although the time series can be used directly for training and testing of ANN models, it takes significantly long time to train the ANN model as there are numerous data points. Alternatively, the features of measured data can be extracted to provide inputs and outputs for ANN models. For sinusoidal waveforms, amplitude, frequency and phase are easy to calculate and they are features that can fully specify the waveforms. However, in the case of linear compressors, the voltage and current signals from measurements were distorted and deviated from sinusoidal waveforms due to heat and mass transfer within the compression chamber with reed valves opening and closing, leakage across the radial clearance gap, non-linear cooling loads, and hysteresis loss in the motor.

FFT is an algorithmic implementation of the Fourier Transform which acts on discrete samples of a time domain waveform. The transformed time domain data gives a frequency domain representation of the captured signal spectrum. The discretely sampled signal can be described by the sum of a finite number of sine and cosine components. The first six harmonic terms were used to describe sampled current and voltage signal as follows:

$$I = \sum_{i=1}^{6} I_i \cos(2\pi i f t + \varphi_{Ii}) + b_i \quad (6.1)$$

$$V = \sum_{i=1}^{6} v_i \cos(2\pi i f t + \varphi_{vi}) + b_v \quad (6.2)$$

where I and V are sampled current and voltage, f is the fundamental frequency, I_i and v_i are the amplitudes of current and voltage of the ith harmonic term, φ_{Ii} and φ_{vi} are the phase for the, b_i and b_v are the DC offset of current and voltage.

Fig. 5.2 shows the steady state voltage, displacement and current signals in two cycles form measurements with a sampling rate of 5000 Hz with a pressure ratio of 2.5 using R1234yf as working fluid. About 139 data points were recorded in each cycle. The periods of three signals are all 27.8 ms, which corresponds to operating frequency of 36 Hz. Although the distortion and deviation of the signals from sinusoidal waveforms is not very obviously shown in Fig. 5.2, harmonics exist in the sampled signals. The current lagged the voltage about 79 degree, which is due to the combined effect of electrical inductance, capacitance and the equivalent reluctance of gas load.

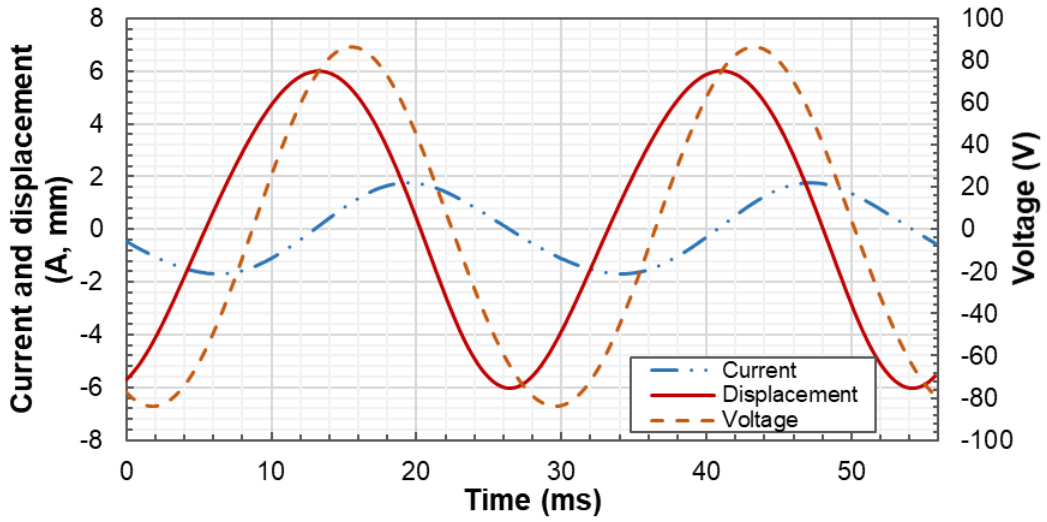

Fig. 5.2 Measured steady-state current, displacement and voltage signal from the test rig

Fig. 5.3 shows the spectrum of the measured signals from FFT analysis. The logged amplitude of current and voltage with frequency are shown in Fig. 5.3a and Fig. 5.3b respectively. The first six harmonic terms appear to be substantial. The fundamental frequency is 36 HZ, which agrees with the operating frequency during the testing. The amplitude of the first harmonic term of current and voltage is 1.6981 A and 85.2315 V

respectively. With the increase of the harmonic order, the amplitude decreases gradually.

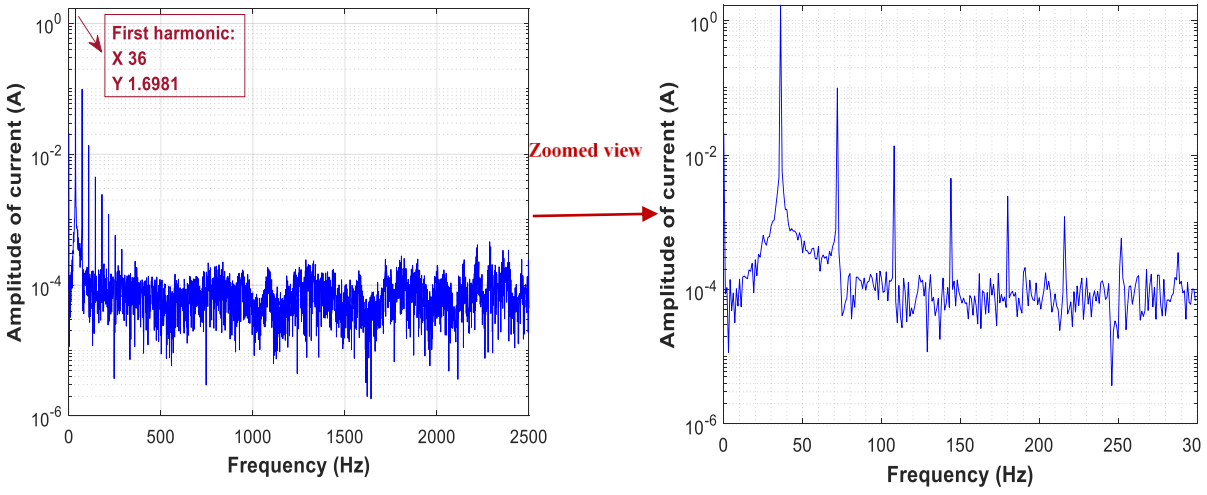

(a)

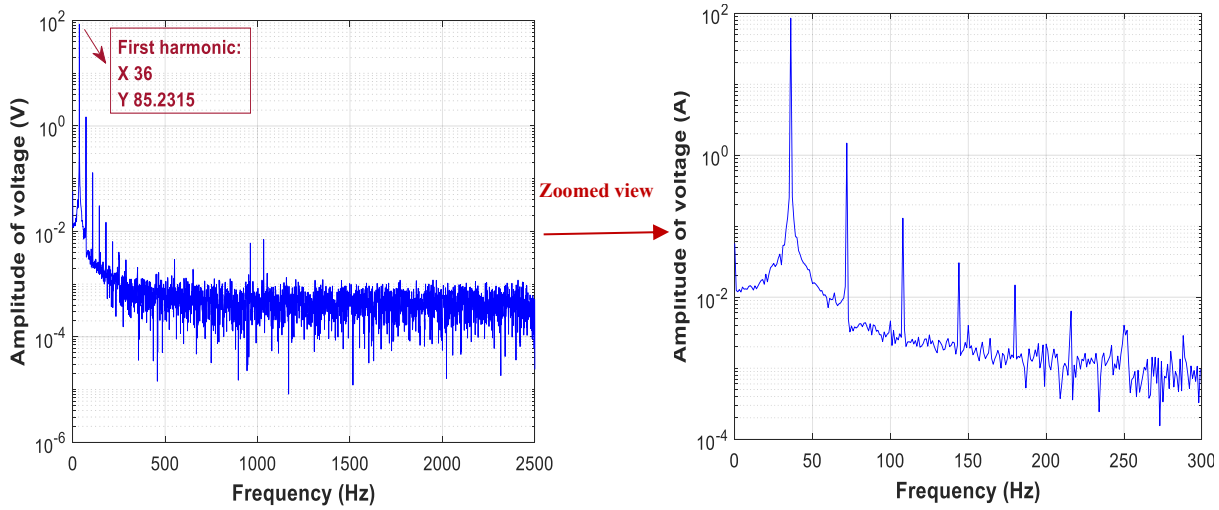

(b)

Fig. 5.3 Spectrum of the measured signals from FFT analysis (a) current (b) voltage

Total harmonic distortion (THD) is a measurement index that shows how much voltage or current signals were deviated and distorted from sine waveforms due to harmonics. Higher frequency components exist in a periodical but not purely sinusoidal signal and contributes to the harmonic distortion of the signal. The mathematical definition of THD is shown as follows:

$$\mathrm{THD} = \frac{\sqrt{\sum_{n=2}^{\infty} V_n^2}}{V_1} \tag{5.3}$$

where V_1 is root mean square (RMS) displacement of the fundamental frequency, V_n is the RMS displacement of the high order harmonic components. Fast Fourier Transform (FFT) analysis was used to determine the amplitude of each harmonic term. The first six harmonic terms were considered in this study. Lower THD in power systems, suggests less heat generation, smaller peak currents, less motor loss, and lower electromagnetic emissions **[152]**. Fig. 5.4 shows the THDs of voltage signals at strokes of 9-12 mm for the linear motor that drives the linear compressor. Generally higher strokes have higher THD. Possible reason for this is that the linear motor is close to saturation with higher strokes where higher currents are supplied. The THD is 1.9% at a stroke of 13 mm. The recommended range of voltage harmonics are within 3% for any single harmonic and 5% for THD **[153]**, which shows that the THDs of voltage of the moving magnet linear motor is within the acceptable range. However, to improve the accuracy of the ANN based sensor-less stroke prediction, FFT analysis was conducted to extract the harmonic terms of signals.

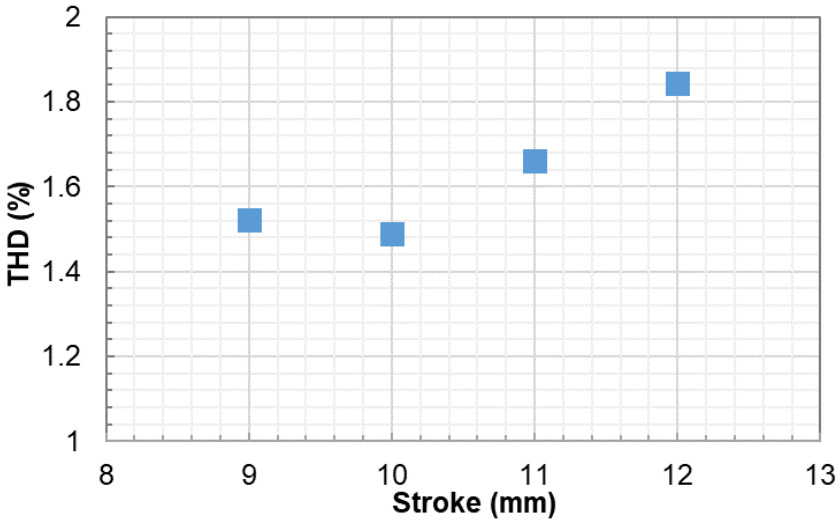

Fig. 5.4 The THDs of measured voltages versus stroke

5.4.2 ANN Model

ANN is a nonlinear mapping system that has emerged as a consequence of a simplification of biological neurons in a brain. ANNs consist of interconnected group of units that receive inputs and deliver outputs based on their predefined activation functions. Their ability to learn by experimental data makes them flexible and powerful tool for approximation.

Fig. 5.5 shows an artificial neural unit which consists of inputs, weights, summation, activation function and output. Input layer feeds data into ANN models. No weights and activation function are contained in an input layer, so it is not a computing layer. The predictive result of an ANN is output through the output layer. In a computing layer, each neuron receives weighted results from the layer before it goes through incoming connections, and then all the weighted results are summed and passed through activation function.

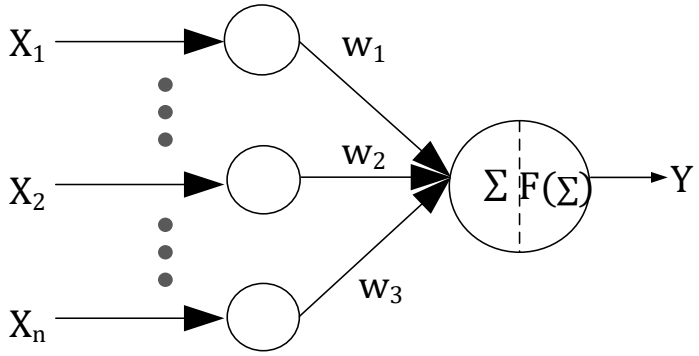

Fig. 5.5 The schematic of artificial unit

A multi-layer perceptron (MLP) contains one or more hidden layers (apart from one input and one output layer). While a single layer perceptron can only learn linear functions, a MLP also learn non-linear functions. The hidden layer neurons allow us to capture subtle interactions among our inputs which affect the final output downstream. Another way to interpret this is that the hidden layers represent higher-level “features” or attributes of our data. Each of the neurons in the hidden layer weights the inputs differently, learning some different intermediary characteristic of the data, and our output neuron is then a function of these instead of the raw inputs. By including more than one hidden layer, we give the

network an opportunity to learn multiple levels of abstraction of the original input data before arriving at a final output.

Fig. 5.6 shows the structure of the MLP neural network model developed for predicting the stroke in the linear compressor. There were two hidden layers and each hidden layer had eight neurons. Inputs of the ANN model were harmonic terms extracted from sampled current and voltage signals. The DC offset of current and voltage calculated based on FFT analysis were neglected as they were small. The target of the ANN model was stroke calculated from measured displacement. Fundamental frequency f, the amplitude of the ith harmonic term of current I_i, the amplitude of the ith harmonic term of voltage V_i, phase difference $\Delta\theta_{vi}$ between current and voltage and phase difference $\Delta\theta_{ij}$ were fed into the ANN as inputs. The phase difference $\Delta\theta_{vj}$ and $\Delta\theta_{ij}$ are defined as follows:

$$\Delta\theta_{vi} = \varphi_{vi} - \varphi_{vi} \tag{5.4}$$

$$\Delta\theta_{Ii} = \varphi_{Ii} - i * \varphi_{I1} \quad (i=2,3,4,5,6) \tag{5.5}$$

While linear functions are particularly used in input and output layers, non-linear activation functions can be used for hidden and output layers. The most commonly used nonlinear activation functions are the sigmoid (logistic) and tangent hyperbolic functions. Using the tangent activation function caused faster convergence of the learning algorithms than did the sigmoid function. In the ANN model, tangent hyperbolic activation function was used in the hidden layers. The tangent hyperbolic function is as follows:

$$tansig(n) = (e^n - e^{-n})/(e^n + e^{-n}) \tag{5.6}$$

The output of the first hidden layer is:

$$y_j^1 = (e^{n_j^1} - e^{-n_j^1})/(e^{n_j^1} + e^{-n_j^1}) \tag{5.7}$$

$$n_j^1 = \sum_{x=1}^{i}(p_x * w_{xj}^1 + b_j^1) \tag{5.8}$$

The output of the second hidden layer is:

$$y_k^2 = (e^{n_k^2} - e^{-n_k^2})/(e^{n_k^2} + e^{-n_k^2}) \tag{5.9}$$

$$n_k^2 = \sum_{x=1}^{j}(y_x^1 * w_{xk}^1 + b_k^1) \tag{5.10}$$

The output of the ANN model is:

$$S = \sum_{x=1}^{k}(y_x^2 * w_{x1}^1 + b_1^3) \tag{5.11}$$

The MLP neural network model was trained and tested with the inputs and targets calculated from sampled signals. Harmonic term independency analysis was carried out by comparing the results with different number of harmonic terms fed into ANN model as inputs. Six cases were considered with the number of harmonic terms ranging from one to six.

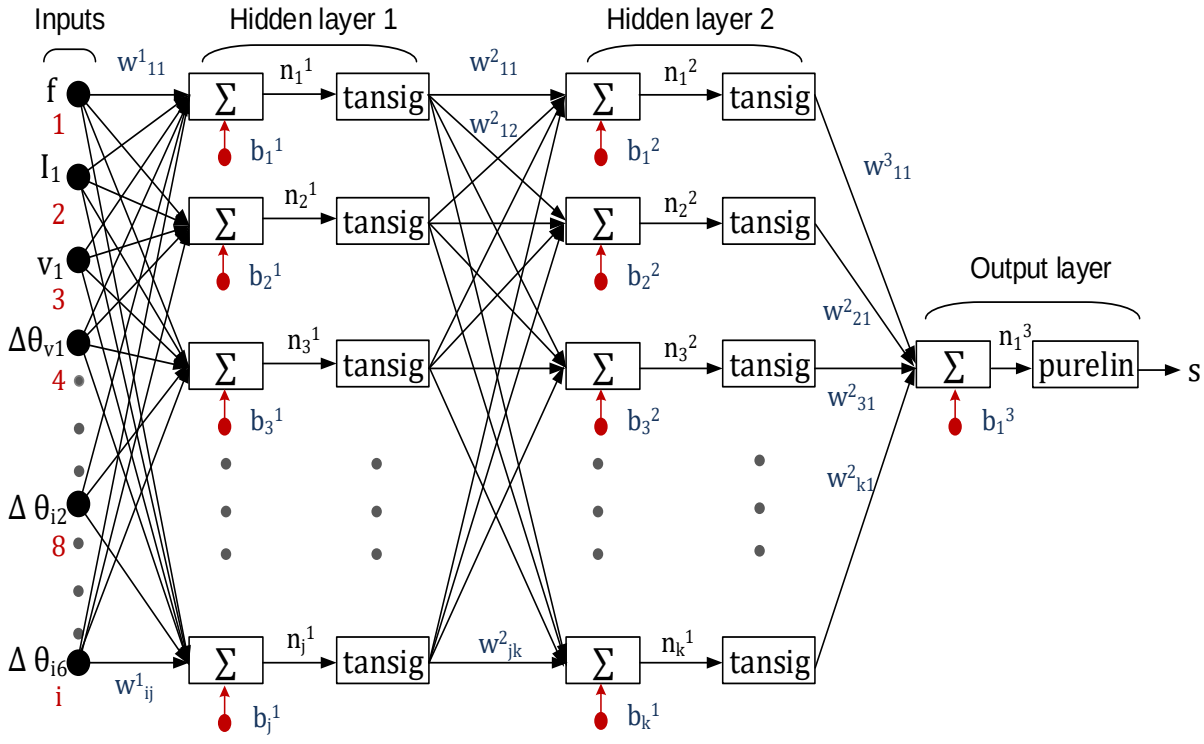

Fig. 5.6 The structure of the neural network model of two hidden layers

Table. 5.2 shows the number of terms of inputs and target for 6 cases. In the Case 1, only the fundamental frequency and the first harmonic terms of current and voltage were

considered. In the Case 3 and Case 6, 12 inputs were included respectively.

Table 5.2 Inputs and output of the ANN model for the six cases

	Name	Number					
		Case 1	Case 2	Case 3	Case 4	Case 5	Case 6
input	amplitude of voltage v_j	1	2	3	4	5	6
	amplitude of current I_j	1	2	3	4	5	6
	phase difference $\Delta\theta_{vn}$	1	2	3	4	5	6
	phase difference $\Delta\theta_{in}$	0	1	2	3	4	5
	fundamental frequency f	1	1	1	1	1	1
target	stroke s	1	1	1	1	1	1

5.5 Results and Discussions

5.5.1 Results of ANN model

There are 542 sets of data in total, 452 sets of which were used for training and the other 89 sets of which were used for testing. The ANN model for each Case was trained with Bayesian regularization (BR) backpropagation algorithm to obtain a small error. Essentially, BR has an objective function that includes a residual sum of squares and the sum of squared weights to minimize estimation errors and to achieve a good generalized model **[149]**.

Fig. 5.7 shows the training performance improving with iterations for the Case 3. Mean squared error (MSE) was chosen as the performance function for training and testing. Generally, both the MSE for training and testing decreases with iteration. The iteration at which the testing performance reached a minimum of 2.23e-4 is 298. The training

continued for three more iterations before the training stopped. This figure does not indicate any major problems with the training. The validation and test curves are similar. The testing performance is 9.94e-4, which is a little worse than the training performance. The comparison of MSE for three cases is shown in Table. 5.3. Both the testing and training performance can be improved by increasing the harmonic terms from one to three whereas performance deterioration is indicated when harmonic terms are increased from three to four. Small performance improvement is shown when the number of harmonic term is increased to over 5. Over-fitting occurs in Case 4-6 as the training MSE decreases while testing performance is hardly improved.

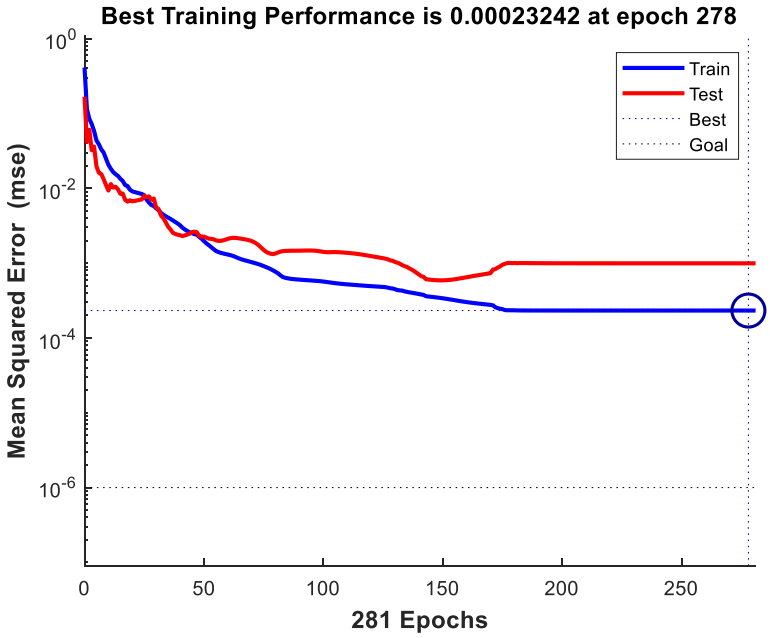

Fig. 5.7 Training performance improving with iterations for Case 3

The performance of ANN based prediction can be indicated by a regression analysis between the outputs of the ANN model, i.e. predicted strokes, and the corresponding targets, i.e. actual strokes from measurements. Correlation coefficient (R) is an index that evaluates the strength of the relationship between the network outputs and targets:

$$R(y,t) = Cov(y,t)/\sqrt{Cov(y,y)Cov(t,t)} \tag{5.12}$$

where y represents sets of network output, t represents corresponding targets, and *Cov(y,t)*

denotes the covariance between network outputs and targets.

R ranges between -1 and +1. *R* values close to +1/-1 indicate a stronger positive/negative linear relationship, whereas *R* values close to 0 indicate no linear relationship between network outputs and targets. Fig. 5.8 shows the regression plots for training and testing between the network outputs and targets. The dashed line in each plot represents the perfect results that network outputs equal to targets. The solid line in each plot is the fitted linear regression line between outputs and targets. For this case, the fit is reasonably good for both training and testing data sets, with *R* values of 0.9999 and 0.99256 respectively. As shown in Table. 5.3, *R* value of testing data increases by 0.0186 when harmonic terms is increased from one to three, but small difference of R values of testing data are found between Case 3 and Case 6.

Table 5.3 Mean squared error and Correlation coefficient for the six cases

case number	MSE		R	
	training	testing	training	testing
1	5.60e-3	3.40e-3	0.9841	0.9739
2	3.26e-4	6.26e-4	0.9909	0.9954
3	2.32e-4	9.94e-4	0.9993	0.9925
4	1.37e-4	1.10e-3	0.9996	0.9914
5	9.19e-5	9.03e-4	0.9997	0.9929
6	3.63e-5	9.62e-4	0.9999	0.9926

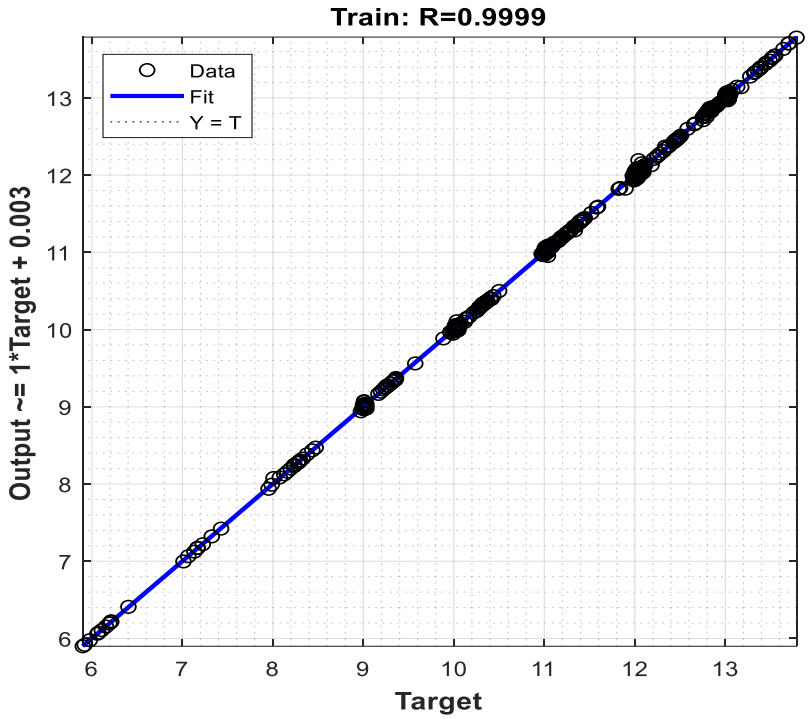

(a)

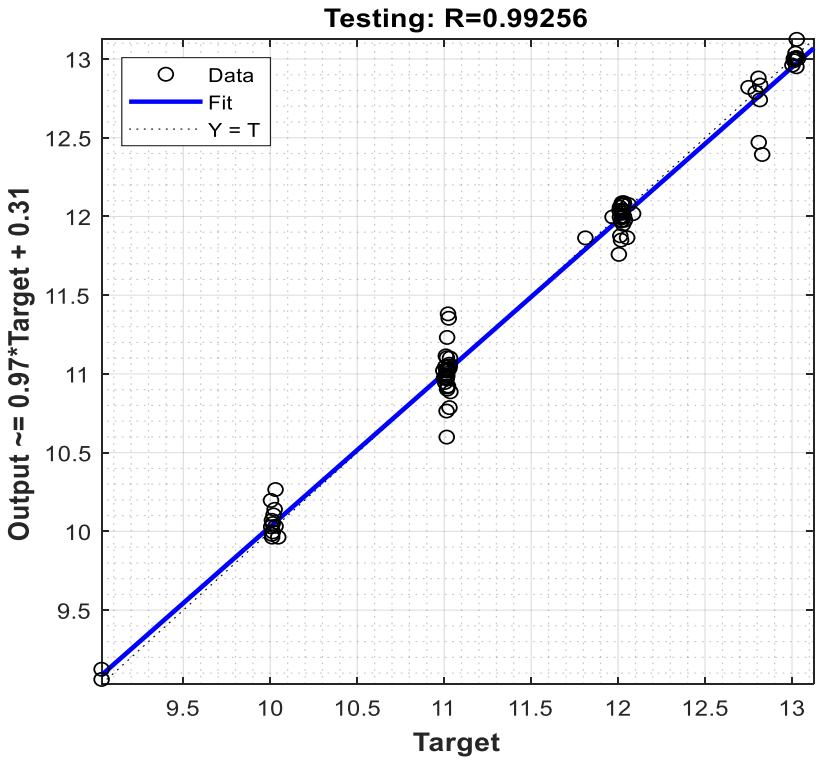

(b)

Fig. 5.8 Regression plotting between targets and output results from the ANN model for Case 6 (a) training (b) testing

An error histogram provides a quick way for visualizing the distribution of errors between network outputs and targets. An efficient ANN model would show a peak around zero, quickly falling off as the data numbers of errors of greater magnitude diminishes. As mentioned in Section IV, three cases with one, three and six harmonic terms of current and voltage as inputs were considered. Instead of plotting error histogram, percentage error histograms are plotted for a better visualization of the accuracy of the ANN based prediction. Percentage error (PE) is calculated as:

$$PE = 100 * (y - t)/t \tag{5.13}$$

Fig. 5.9 shows the percentage error histogram for three cases. The real valued network percentage errors are divided into 20 bins and counting the number of percentage errors in each bin. The blue bars represent training data, and the green bars represent testing data. Outliers are shown in Fig. 5.9a, which refer to data points where the fit is significantly worse than most of data. The majority of the percentage errors fall within ±5.6% whereas the largest percentage error is -16.86%. Fig. 5.9b shows the percentage error histogram for Case 3. The largest percentage error is about 4.6%, the range of percentage error that includes the majority of data is between -2% and 1.4%. As shown in Fig. 5.9c, Case 6 shows a better percentage error distribution than Case 1 and 3 with most of the percentage error falling within ±0.7% and the largest percentage error of 3.5%. Three harmonic terms as inputs gives the best results as it demonstrates good accuracy and the chance that over-fitting occurs is smaller.

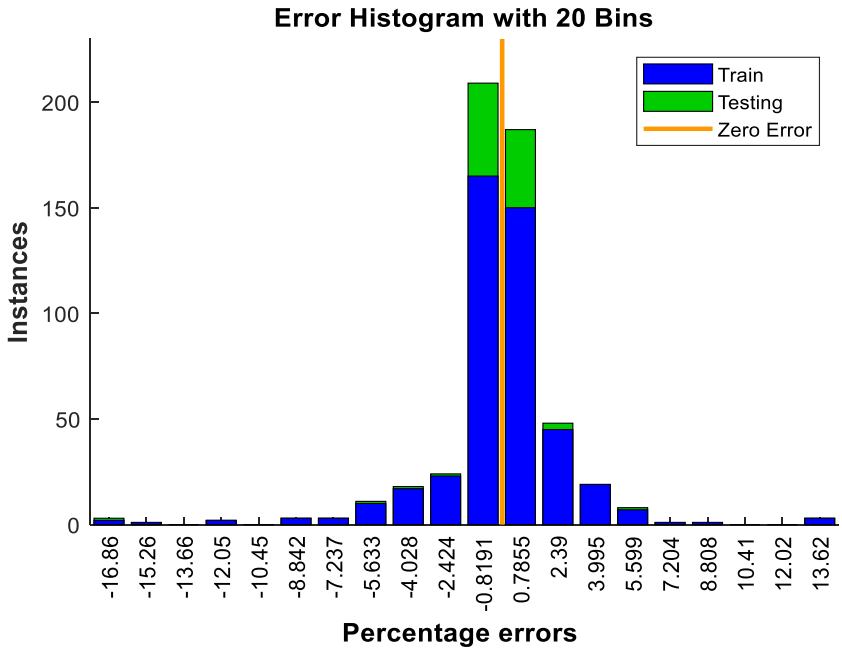
Error Histogram with 20 Bins
Train
Testing
Zero Error
Instances
0
50
100
150
200
-16.86
-15.26
-13.66
-12.05
-10.45
-8.842
-7.237
-5.633
-4.028
-2.424
-0.8191
0.7855
2.39
3.995
5.599
7.204
8.808
10.41
12.02
13.62
Percentage errors

(a)

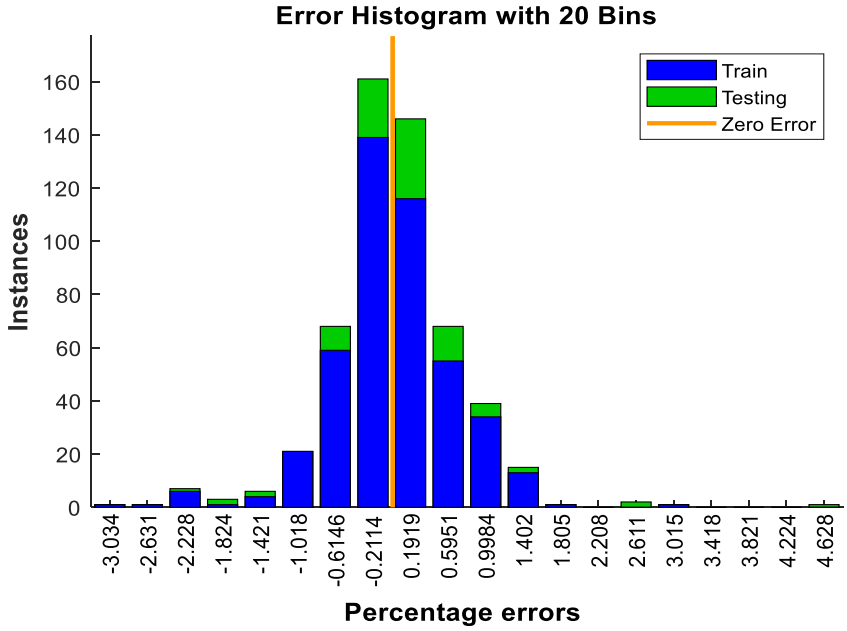
Error Histogram with 20 Bins
Train
Testing
Zero Error
Instances
0
20
40
60
80
100
120
140
160
-3.034
-2.631
-2.228
-1.824
-1.421
-1.018
-0.6146
-0.2114
0.1919
0.5951
0.9984
1.402
1.805
2.208
2.611
3.015
3.418
3.821
4.224
4.628
Percentage errors

(b)

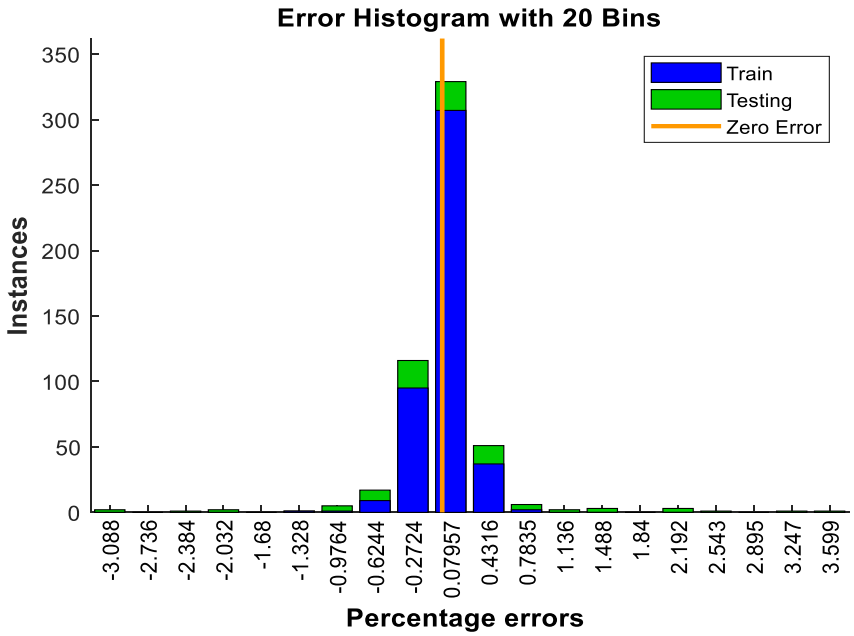

(c)

Fig. 5.9 Percentage errors of training and testing (a) Case 1 (b) Case 3 (c) Case 6

5.5.2 Predicted Stroke for System Performance

The stroke prediction based on the ANN model forms the basis for a sensor-less control method for the linear compressor. The stroke can be regulated according to external load variation with sampled current and voltage. Fig. 5.10 plots the measured mass flow rate by mass flow meter against predicted strokes from the ANN model when the linear compressor is operated with a pressure ratio of 2.5 using R1234yf as working refrigerant. An increase of 3 mm in stroke produces the increase in mass flow rate from 0.27 to 1.33 g/s.

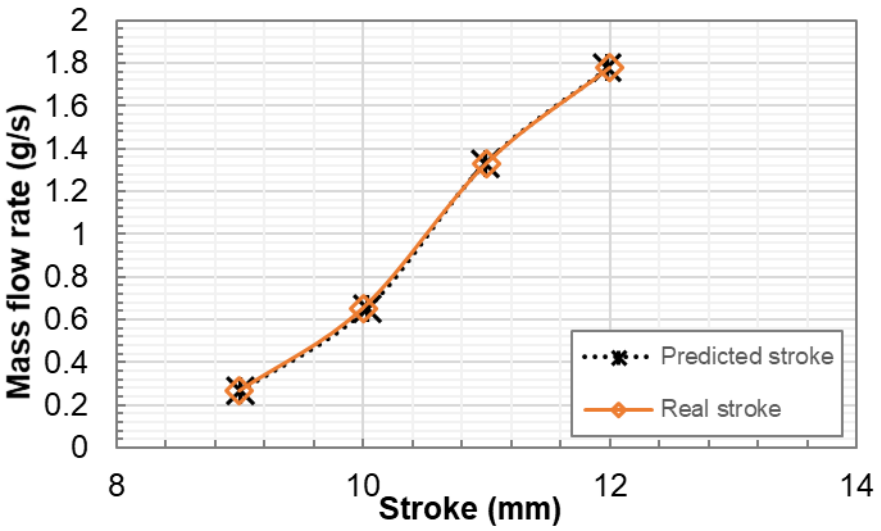

Fig. 5.10 Mass flow rate versus predicted strokes using R1234yf with a pressure ratio of 2.5

Fig. 5.11 shows electrical power input and cooling capacity for various predicted strokes of 10-12 mm. Both power input and cooling capacity increase with predicted stroke. With the increase of predicted stroke from 10mm to 12 mm, the power input of the linear compressor increases from 22 W to 81 W, and the cooling capacity increases from 35 W to 241 W. With the ANN based stroke prediction, it is possible to develop a control system that could adjust the drive signal (amplitude of input voltage for the power amplifier) thus the stroke according to the cooling load without need for a displacement sensor. We can also monitor the instantaneous stroke to avoid the piston hitting the cylinder head.

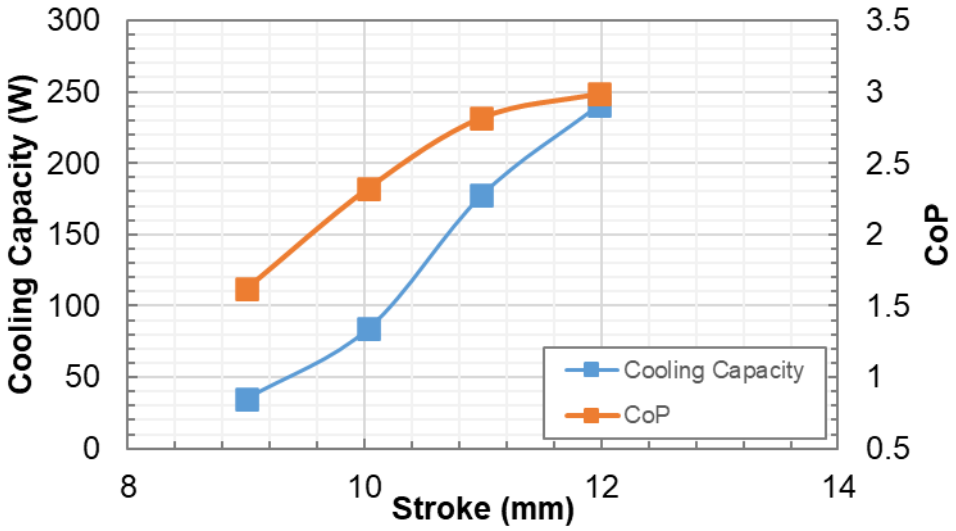

Fig. 5.11 Power input and cooling capacity versus predicted strokes using R1234yf with a pressure ratio of 2.5

5.6 Conclusions

An ANN model based stroke prediction method that can be used in linear compressors was introduced in this chapter. A number of tests were conducted in the refrigeration system driven by a novel oil-free linear compressor. Although measured current, voltage and displacement signals appear to be sine waves, the waveforms can not be described with one basic sine function, which means harmonics exist in the sampled signals. FFT analysis was performed on measured current and voltage to extract harmonic terms that were fed into the ANN model as inputs. Harmonic term independency study was carried out by considering different number of harmonic terms as inputs. Key findings are shown as below:

(1) Voltage and current from measurements were distorted and deviated from sinusoidal waveforms, and the first six harmonic terms are dominant.

(2) Both the mean squared errors and correlation coefficient values are improved with the increase of harmonic terms from one to three whereas the improvements are not obvious with harmonic terms increased from three to six.

(3) Six harmonic terms as inputs demonstrates better percentage error distribution with the majority falling within ±0.7% and the largest percentage error of 3.5%.

(4) With the stroke prediction using ANN presented in this chapter, and the sensor-less piston offset detection method reported in **[135]**, axial clearance can be detected without a displacement sensor, and can be adjusted in accordance with cooling capacity demands.

Although the sensor-less stroke detection using ANN can achieve a good accuracy for most of the cases, the potential risk of collision between piston and cylinder head still exists as the neural network model may give a very inaccurate result for a few cases. A more robust, reliable and accurate sensor-less stroke detection technique needs to be proposed. In next chapter, a novel sensor-less stroke detection technique based on inductive coil will be presented.

Chapter 6 Sensor-less Stroke Detection using Low-cost Inductive Coil with Resonant Operation

6.1 Introduction

When a linear compressor is operated at its resonant frequency, system efficiency reaches maximum. Some researchers have investigated the modelling of resonant frequency for linear compressors. The non-linear characteristic of gas pressure makes it difficult to derive the exact gas spring stiffness. A simple linearization approach to obtain the approximation of gas stiffness was presented by Cadman and Cohen **[10]**, which is widely adopted by Bradshaw **[154]** and Liang et al. **[109]**. The experimental results by Liang **[109]** showed the feasibility of this approach. A new solution to the linearization of the gas pressure force was proposed by Dainez et al. **[155]**. Based on the same effect on compressor of the gas pressure and equivalent forces, an equivalent damping force, an equivalent spring force, and an equivalent continuous force were used to replace the nonlinear gas force. However, in most of the studies mentioned above, the influence of magnet spring was not taken into account. As presented by Chen et al. **[119]**, when zero current was supplied, magnetic force was zero at central position, but this increased greatly with the displacement. Xia et al. **[125]** further considered the effect of position-dependable magnetic force without excitation current as 'magnet spring'. Simulations and tests were conducted to analyse the resonant frequency of the linear compressor for Stirling cryocooler. The results showed that magnet spring existed and influenced the resonant frequency for Sunpower type moving magnet linear compressor.

The resonant operation can also be achieved by using resonance tracking algorithm Lin et al. **[156]** achieved the resonance tracking of a linear compressor by adjusting operation frequency to reach maximum input power for a fixed amplitude of current. Resonance can be identified according to the phase difference between motor current and piston position **[157]** or between current and velocity **[158]** as well.

Using displacement sensors is very expensive even for mass production of free-piston machines. Existing sensor-less approaches require complex modelling and parameter identification. There is hardly a generic sensor-less technique for any free-piston machines. There is a clear gap between demand and supply of low-cost sensor-less technique for free-piston machines. This chapter introduces a novel sensor-less stroke detection technique using inductive coils for free piston machines operated at resonance. The low-cost technique is straightforward as no complex calculation is required. Little space is required for installation so that it can be used for stroke detection in small-size machines.

6.2 Stroke Detection Technique Using Inductive Coil

Generally, in a moving magnet type linear motor, the flux linkage in cores is induced by magnets and excitation AC current applied into main coils. For resonant operation, the current is zero when piston displacement reaches maximum, and the flux linkage induced by the current equals zero. By calculating the flux linkage difference between two zero crossing points of current, the flux linkage variation in one core induced by the movement of magnets can be identified. The relation between the stroke (peak-to-peak displacement) and the variation of the flux linkage can then be identified. Inductive coil which doesn't carry any current can be wound around main coil to find the relation between flux linkage variation and magnet motion.

The open circuit inductive coils wound around the middle and end cores were used to detect the piston stroke by calculating the variation of flux linkage across the inductive coil where no current flows. Fig. 6.1 shows the inductive coil with 10 turns wounded around the main coil with a magnet placed in the slot. The two ends of each inductive coil were wired up to the analogue input channel of NI DAQ card for voltage measurement.

For any free-piston machine, resonant frequency can be calculated based on gas force stiffness, mechanical spring stiffness and magnetic spring stiffness so that operating

frequency can be adjusted accordingly **[118]**. The resonant operation can be monitored by looking at the measured current and displacement. If the current reaches zero at maximum and minimum displacements, resonance can be confirmed **[159]**.

The flux linkage variation $\Delta\varphi$ is the flux linkage difference (FLD) between two zero crossing points of current where piston displacement reaches maximum and minimum at resonance. $\Delta\varphi$ can be calculated by

$$\Delta\varphi = \varphi_2 - \varphi_1 \tag{6.1}$$

$$\varphi = \int V_s \, dt \tag{6.2}$$

where V_s is the open-circuit voltage of inductive coil, φ is the flux linkage in the middle core/end core, φ_1 and φ_2 are the flux linkage at two zero crossing points of current.

The variation of the FLD with the stroke can be modelled and verified by experimental data in prototyping stage. When the FLD as a linear function of the stroke is obtained, the instantaneous FLD in the inductive coils can be used to infer the stroke.

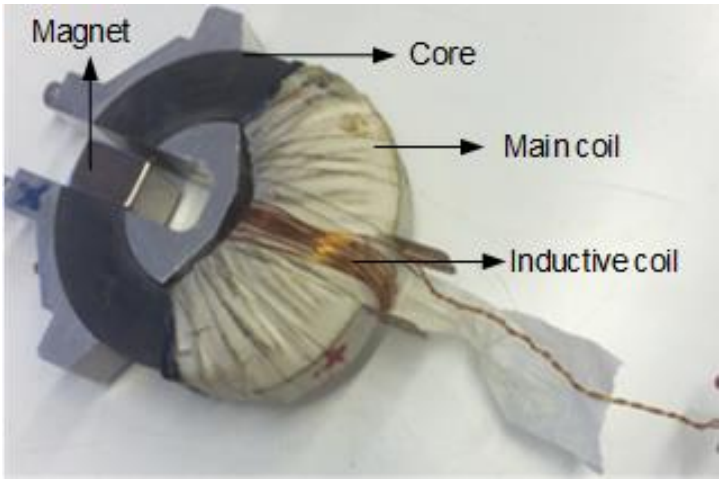

Fig. 6.1 Core with main coil and inductive coil wound around adapted from **[135]**

A one-dimensional (1-D) magnetic equivalent circuit (MEC) model and a three-dimensional (3-D) finite element analysis (FEA) model were established to investigate the flux linkage variation against the piston position with no current supplied.

Experiments of the linear compressor at various piston strokes were conducted at resonance to validate the two models and to evaluate the accuracy of the inductive coil technique. The influence of phase lag induced by the LVDT and off-resonance on the accuracy of the stroke detection technique was also investigated.

6.3 Magnetic Equivalent Circuit Model

6.3.1 Model Description

A magnetic equivalent circuit model of the linear motor when there is no external excitation is shown in Fig. 6.2. The model consists of permanent magnets, external excitation through main coil, cores, air gap, and flux leakage paths. The main flux flows from permanent magnets to cores through the air gap between magnets and poles, and back to the other side of magnets through air gap. The two air gaps are symmetric so that the top reluctances representing the top air gap are same as bottom ones. Permanent magnets are represented by the combinations of equivalent flux source and reluctance. Flux leakage paths include the leakage between two adjacent magnets and leakage between two adjacent cores. A resistance represents each air gap between a magnet and a core, and the reluctance values vary with piston position.

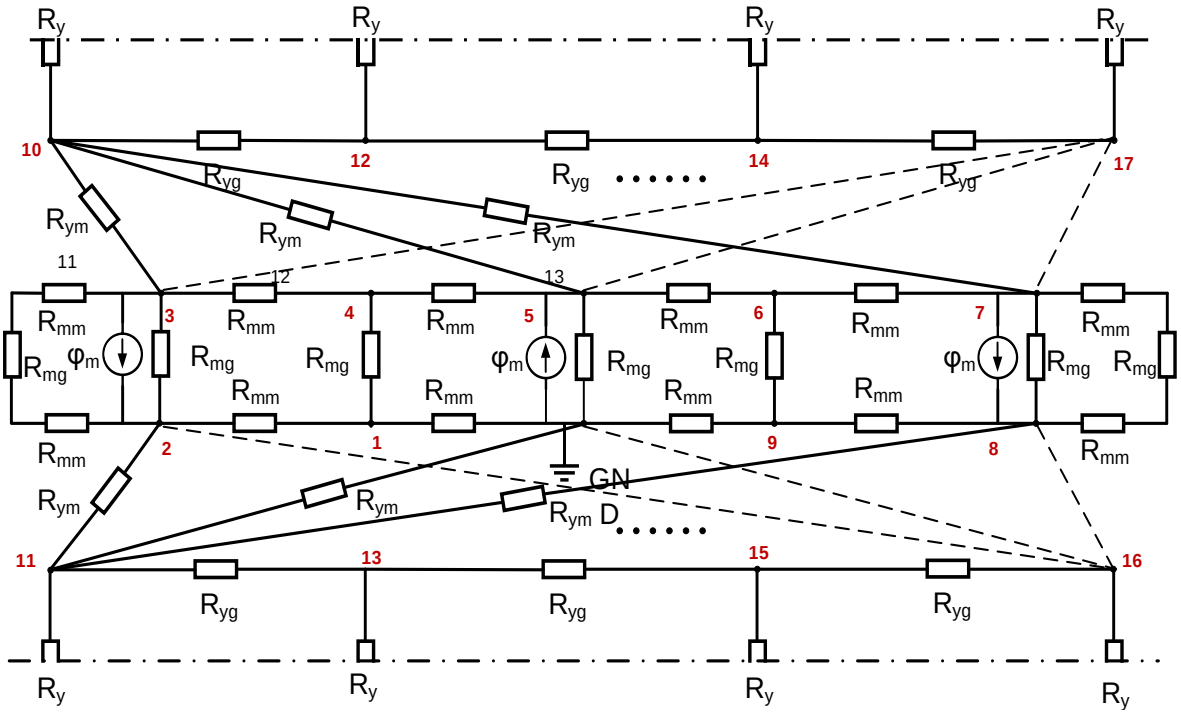

Fig. 6.2 The 1-D magnetic equivalent circuit model of the moving magnet linear motor

6.3.2 Equivalent Magnetic Reluctance

A general expression for the value of reluctance R is

$$R = lH/AB \tag{6.3}$$

where H is magnetic field intensity in a circuit, B is magnetic flux density, l is the length of the magnetic circuit, and A is the area of the cross section of the magnetic circuit (see Fig. 1b).

The equivalent flux source φ_{m} and reluctance $\mathrm{R_m}$ for permanent magnets and excitation flux units are

$$R_m = h_m/(\mu_0 \mu_{rm} w_m L) \tag{6.4}$$

$$\varphi_m = H_c h_m / R_m \tag{6.5}$$

where h_m, w_m and L represent the height along magnetization direction, width, and thickness magnets as shown in Fig. 1b. μ_0 and μ_{rm} are magnetic permeability of

vacuum and magnets respectively. H_c is the coercive force of permanent magnets.

The reluctance of core R_y is

$$R_y = p_y/(\mu_0 \mu_{ry} w_y L) \tag{6.6}$$

where p_y and w_y represent the perimeter of cores and width of cores respectively. μ_{ry} is magnetic permeability of cores.

The flux leakage between two adjacent magnets was modelled by reluctance R_{mm} representing path from one magnet to the middle of gap between two adjacent magnets and R_{mm} representing path from one side of the magnet to the other **[160]**. Leakage reluctance between two adjacent cores was represented by R_{yg}. Reluctances R_{mm}, R_{mg} and R_{yg} that represent flux leakage are **[159]**

$$R_{mg} = h_m/(\mu_0 w_{mm} L) \tag{6.7}$$

$$R_{mm} = [\mu_0 L/\pi \, ln \, (1 + \pi g/w_{mm})]^{-1} \tag{6.8}$$

$$R_{yg} = w_{yy}/(\mu_0 A_{yy}) \tag{6.9}$$

where g and w_{mm} are the air gap between magnets and cores, and the distance between two adjacent magnets respectively. w_{yy} and A_{yy} are the distance between two adjacent cores, and the flux leakage area between two adjacent cores respectively as shown in Fig. 6.3.

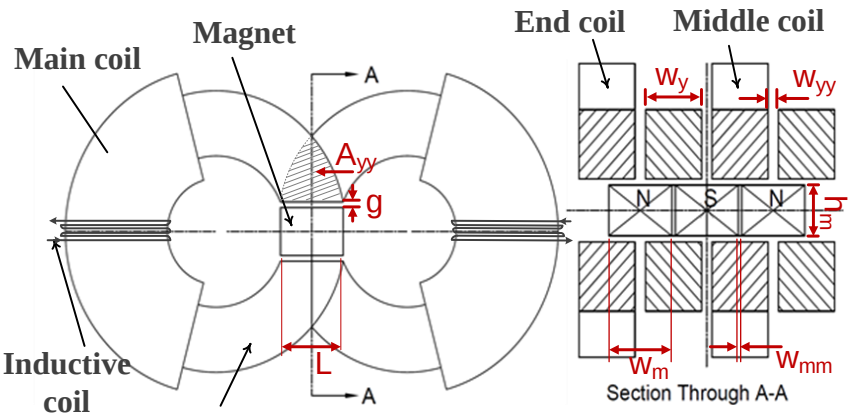

Fig. 6.3 Denotation of the symbols used in the equivalent magnetic circuit model

The relative position of magnets and cores changes as the piston oscillates. To quantify the reluctance between each magnet and core, in axial direction, three cases were considered depending on the relative position of the magnet and the core: magnet inside the slot of core, magnet partially inside the slot of core and magnet fully outside the slot of core. When the magnet is inside or partially inside the core slot, air reluctance calculation includes three parts: the calculation of cuboid air reluctance formed by the pat of magnet and core (the rectangular part shown in Fig. 6.4a and Fig. 6.4b, and the calculation of the remaining two parts with consideration of fringing effect. As shown in Fig. 6.4c, the air reluctance is composed of two paralleled reluctances when a magnet is fully outside the slot of the core. The permanence shown in Fig. 6.4a is calculated as

$$P_{ym} = P_1 + P_2 + P_3 \tag{6.10}$$

$$P_1 = \mu_0 w_y L/g \tag{6.11}$$

$$P_2 = \int_0^{w_2} \mu_0 L dx/(g + x\,\pi/2)$$

$$= 2\,\mu_0 L/\pi * \ln\,(1 + w_2\,\pi/(2\,g)) \tag{6.12}$$

$$P_3 = 2\,\mu_0 L/\pi * \ln\,(1 + w_3\,\pi/(2\,g)) \tag{6.13}$$

where w_2 and w_3 are the widths of the two parts outside the slot as shown in Fig. 4a.

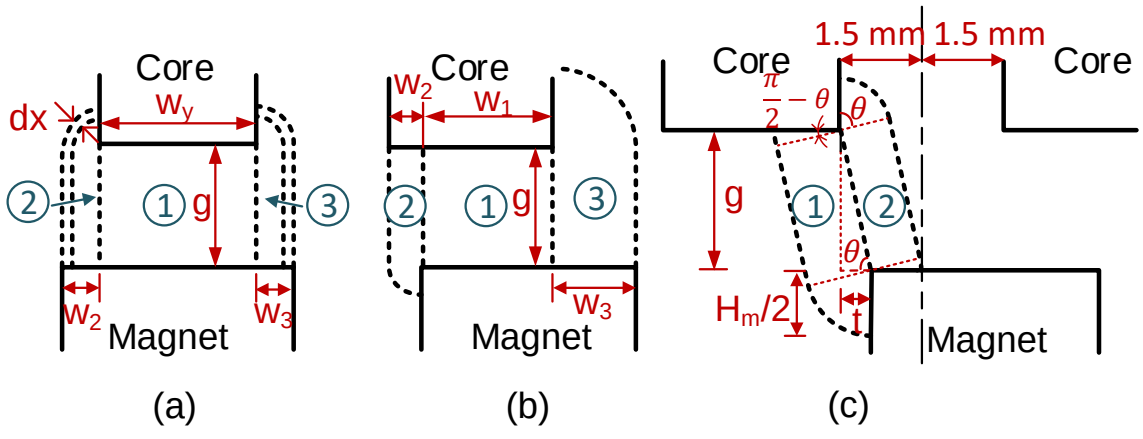

Fig. 6.4 Schematic of discretization of magnets and cores (a) magnet inside the slot of core; (b) magnet partially inside the slot of core; (c) magnet outside the slot of core

An assumption was made to simplify the calculation of the air permanence in Fig. 6.4b and Fig. 6.4c. Only the part of the magnet on the left side of the central axis of two adjacent cores was considered to form the flux path with the core on the left. The permanence of three parts is calculated as

$$P_1 = \mu_0 w_1 L/g \tag{6.14}$$

$$P_2 = 2\,\mu_0 L/\pi * \ln\,(1 + \min(w_2, hm/2) * \pi/(2\,g)) \tag{6.15}$$

$$P_3 = 2\,\mu_0 L/\pi * \ln\,(1 + \min(w_3, 1.5) * \pi/(2\,g)) \tag{6.16}$$

where w_1 is the width of the magnet inside core slot, min(a, b) represents the smaller value of a and b. The permanence shown in Fig. 4c is calculated as

$$P_{ym} = P_1 + P_2 \tag{6.17}$$

$$P_1 = 2\,\mu_0 L/\pi * \ln\,(1 + \pi h_m/(4\sqrt{g^2 + t^2})) \tag{6.18}$$

$$P_2 = 2\,\mu_0 L/\pi * \ln\,(1 + \pi(1.5 - t)/(2\sqrt{g^2 + t^2})) \tag{6.19}$$

where t denotes the distance between the magnet and the core.

6.3.3 Solution using Nodal Law

In a way similar to electrical circuits, a magnetic circuit is composed of a group of branches. The nodal law and loop law allow establishing the algebraic relations between magnetic branches of the circuit in Fig. 6.2. In a complete network of permeance, all the branch flux values and the node magnetic potentials can be computed. The basic equation, which governs each node of the magnetic circuit model, is given by

$$[P]^{-1}[\emptyset] = [F] \tag{6.20}$$

where $[P]$, $[\emptyset]$ and $[F]$ are permeance matrix, flux source vector and magneto-motive force (MMF) respectively.

When there is no zero external exercitation, permanent magnets are the only magnetic flux sources in magnetic equivalent circuit, and the flux source vector is formed as

$$[\emptyset] = [0 \ \varphi_m \ -\varphi_m \ 0 \ \varphi_m \ 0 \ -\varphi_m \ \varphi_m \ 0 \ \cdots \ 0]^T \tag{6.21}$$

The MMF for each node can be calculated using Equation 6.22 when $[P]$ and $[\emptyset]$ are given. The flux between node j and k can be expressed as

$$\varphi_{jk} = \left(F_k - F_j\right)P_{jk} \tag{6.22}$$

where F_k and F_j are the MMF of node k and j respectively. P_{jk} is an element in jth row and kth column of the permeance matrix, which also represents the permeance between node k and j. P_{jk} is calculated as the total admittance joining node j to k.

6.3.4 Flux Linkage Induced by Magnets

The FEA model introduced in the chapter 2 was employed to validate the results from the equivalent magnetic circuit model. A cross sections of a middle core and an end core was created respectively. The FEA model was computed for various displacements with zero current fed into coils. Flux linkage through each cross section was integrated using the field calculator. The computed flux density through a cross section integrated over the cross section gives the flux linkage. The flux linkage calculated from the field calculator was induced by permanent magnets.

Fig. 6.5 shows the flux linkage induced by the magnets for various displacements of -7 mm to 7 mm from MEC and FEA models. The flux linkages induced by the magnets in the middle and end cores vary linearly with displacements, which is mainly due to the linear variation of the air permeance between the magnets and cores as the other reluctances remain unchanged with the displacement. When the piston moves from -7 mm to 7 mm, the flux linkage in the end core varies from -0.28 mWeb to -0.04 mWeb as shown in Fig. 9a, and the flux linkage in the middle core varies from 0.22 mWeb to -0.24 mWeb as shown in Fig. 9b. The average difference between the MEC and FEA models is

4.7% and 8.5% for the end core and middle core respectively.

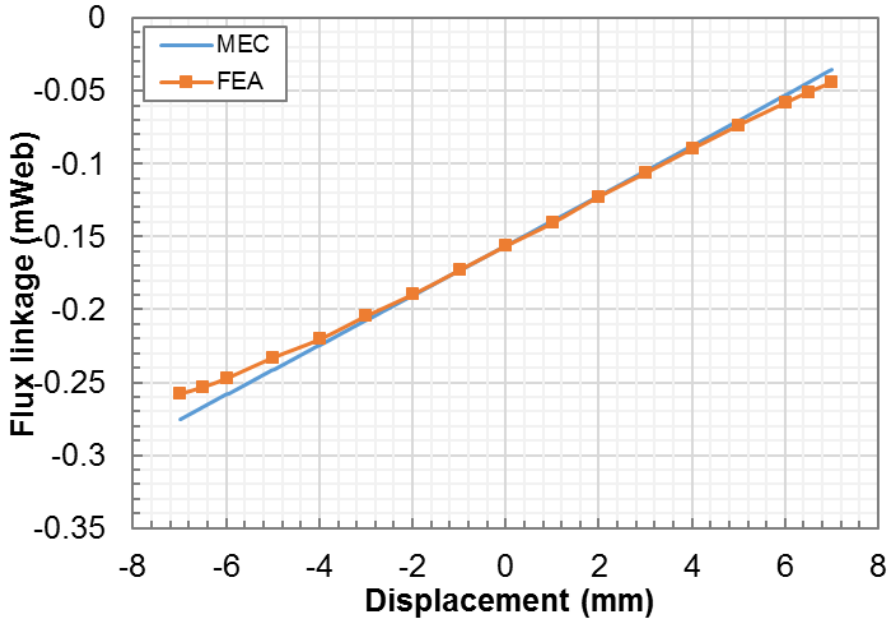

(a)

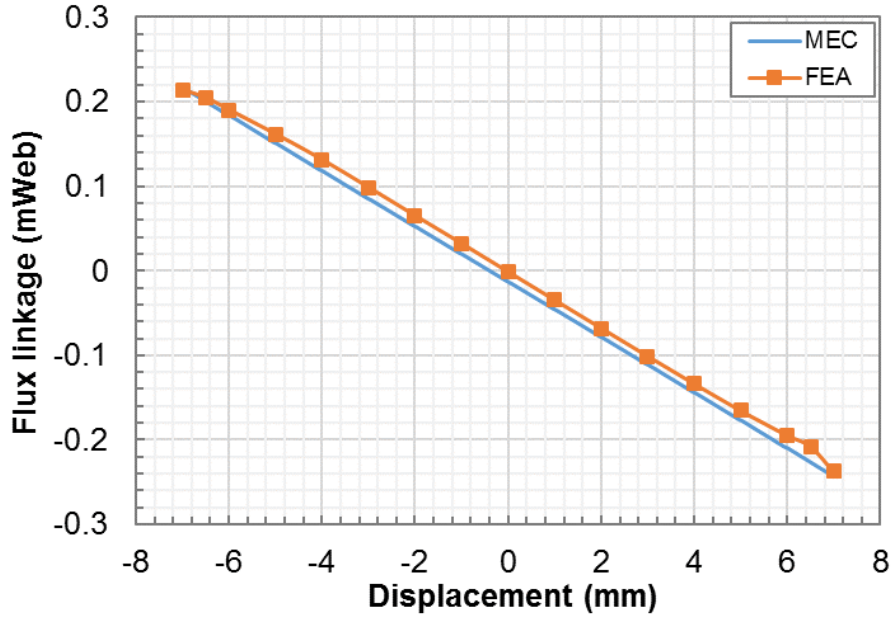

(b)

Fig. 6.5 The flux linkage induced by magnets of middle core and end core for different displacement (a) end core (b) middle core

6.4 Experiments

In order to validate the MEC and FEA models, a number of experiments were carried out in the linear compressor test rig shown in Fig. 2.2 with inductive coils wound around cores in the moving-magnet linear motor. The resonant frequency was calculated automatically with linearized gas spring stiffness and mechanical spring stiffness in LabVIEW. The operating frequency was adjusted manually to ensure that the linear compressor operates at resonance for various strokes. A number of tests were conducted at resonance and off-resonance with various strokes from 6 mm to 13 mm. The current through main coils, voltage across inductive coils and displacement were measured and recorded.

However, the use of the LVDT induces phase lag to the measured displacement signal as reported by Liang et al. **[22]**, which will influence the accuracy of the stroke detection technique. The calculated resonance needs to be verified by checking whether the displacement reaches maximum at zero-current crossing points. The phase lag of displacement caused by the LVDT transducer should be removed.

6.5 Effect of LVDT

The phase lag response to frequency within a range of 30 - 350 Hz is given in Fig. 6.6. It can also be seen from Fig. 6.6 that the phase lag response is a linear function of frequency which can easily give the corresponding phase lag values for each operating condition of the linear compressor, with different resonant frequency. Therefore, the displacement signals from the LVDT transducer can be corrected.

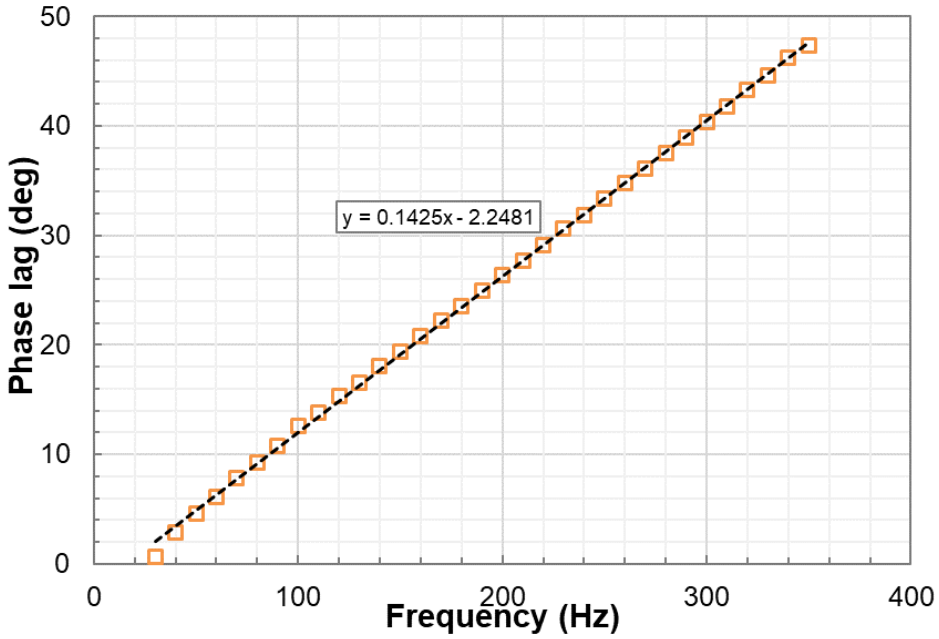

Fig. 6.6 Phase lag characteristic of the LVDT displacement transducer **[22]**

A minimization algorithm based on a solver in MATLAB named 'fminunc', which seeks to find a minimum of a scalar function of several variables, was used to minimize the RMS error between the measured data points and the reconstructed harmonics of displacement signal. With the phase lag characteristic for the LVDT against frequency that was calibrated in the lab, the signal reconstruction was undertaken by removing the phase lag from each harmonic term. Fig. 6.7 shows the reconstructed displacement in comparison with the original signal from measurement. A phase lag of 2.9 degree can be found at 36 Hz. If the phase lag induced by the LVDT displacement transducer is not removed from the measured signal, there will be error in verifying resonant frequency. Note that the phase difference between the current and displacement signals is 90 degree at resonance.

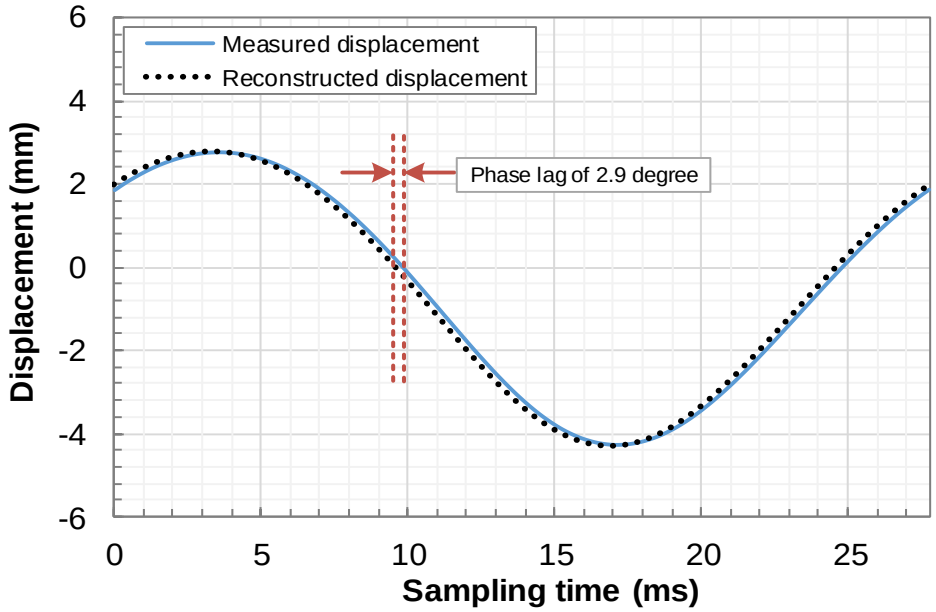

Fig. 6.7 Reconstructed displacement using harmonics fitting

Fig. 6.8 compares the averaged absolute percentage error of flux linkage difference (FLD) calculated from measurements using original and reconstructed signals. The accuracy of the inductive coil technique can be improved if the measured displacement is reconstructed by removing the phase lag.

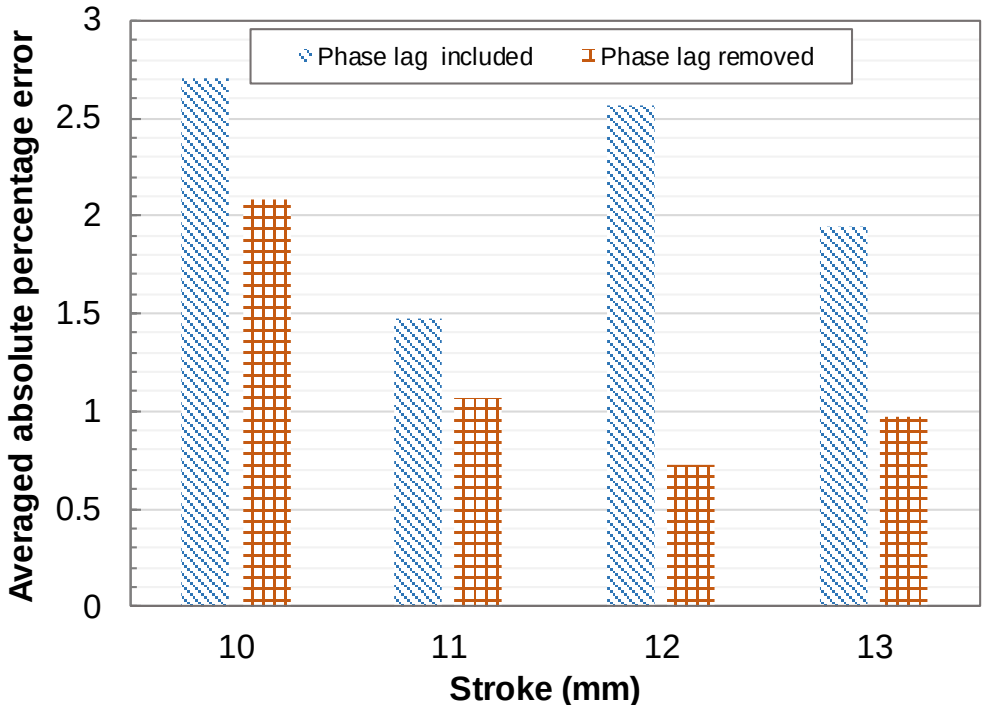

Fig. 6.8 Averaged absolute percentage error of FLD using measured signals and reconstructed signals with consideration of phase lag induced by LVDT

6.6 Flux Linkage Difference at Resonance

Fig. 6.9 shows the measured displacement, current, and voltage, and calculated flux linkage using Equation 6.2 in one cycle for a stroke of 13 mm at resonance. As shown in Fig. 6.9a, when the piston is at the maximum and minimum displacements, the current becomes zero. The measured voltages across the inductive coils are sinusoidal. Voltages with amplitudes of 0.7 V and 0.94 V were detected across the end and middle inductive coils respectively. The flux linkage integrated from the voltage across the end and middle inductive coils is shown in Fig. 6.9b and Fig. 6.9c respectively. At maximum and minimum displacements, the flux linkages in the middle coil are 0.22 mWeb and -0.24 mWeb respectively. As the current is zero at positions of maximum/minimum displacement, the flux linkage is induced by the moving magnets only.

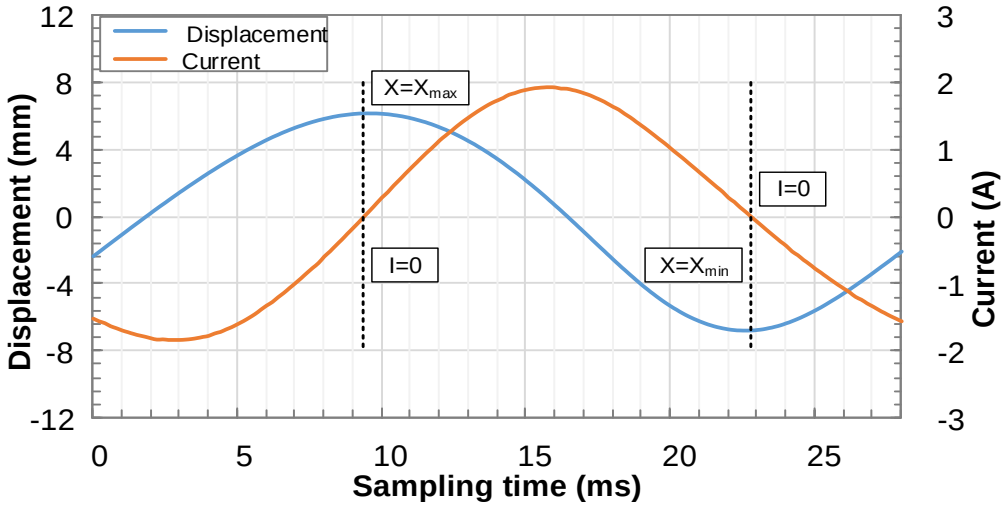

(a)

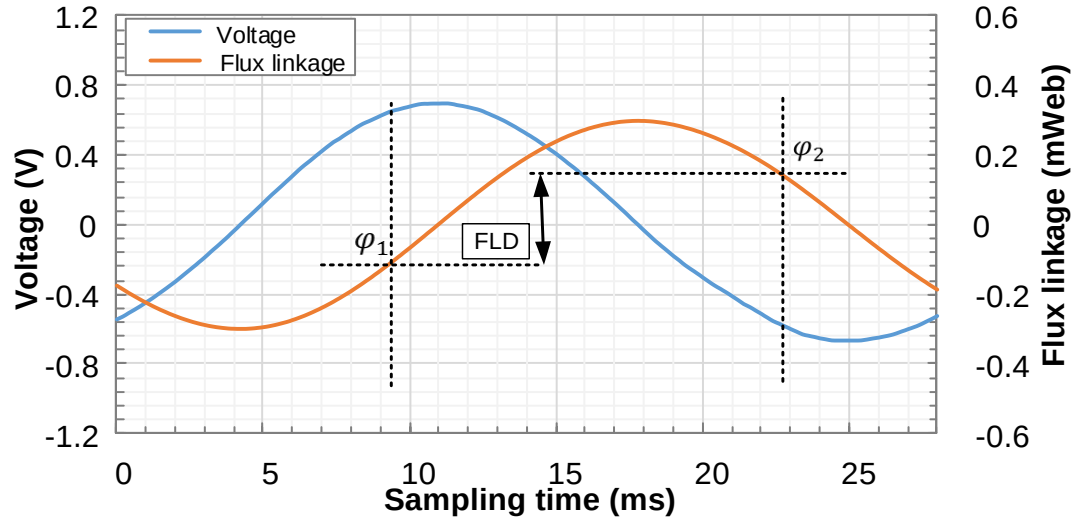

(b)

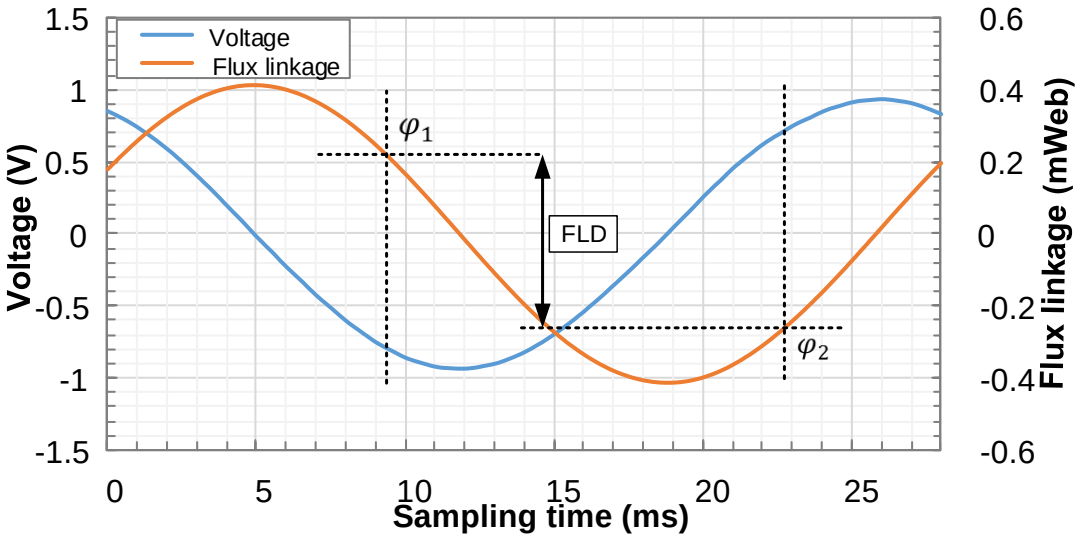

(c)

Fig. 6.9 Measured signals and calculated flux linkage in one cycle for a stroke of 13 mm at resonance (a) measured displacement and current (b) voltage across end inductive coil and calculated flux linkage of end core (c) voltage across middle inductive coil and calculated flux linkage of middle core

Fig. 6.10 shows the FLD induced by the magnets in the end and middle cores at resonance. Based on the linear variation of the flux linkage induced by the magnets with the displacement as shown in Fig. 6.5, the FLD in the end and middle cores for various strokes calculated by MEC and FEA models are shown in Fig. 6.10. The FLD calculated from

experimental data for strokes of 7 mm to 13 mm are plotted in Fig. 6.10 as well. A linear relationship between the FLD and the stroke can be observed. The FLD in the middle core is larger than that in the end core. This is because the air reluctance between the end core and the magnets is larger when the magnets move away from the end core. The maximum percentage error between the measurements and the MEC model is about 14%.

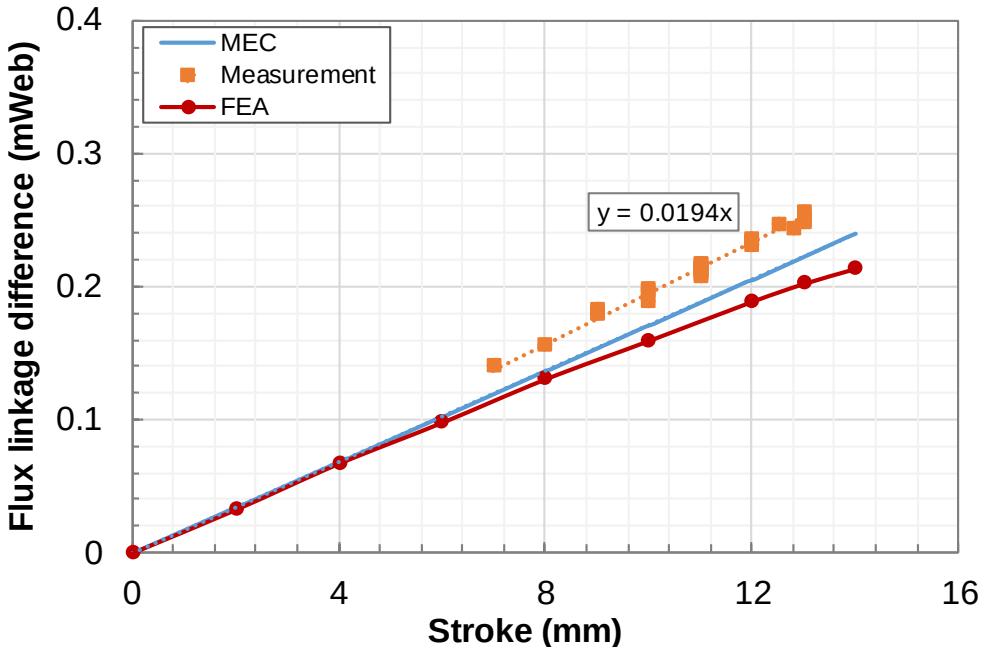

(a)

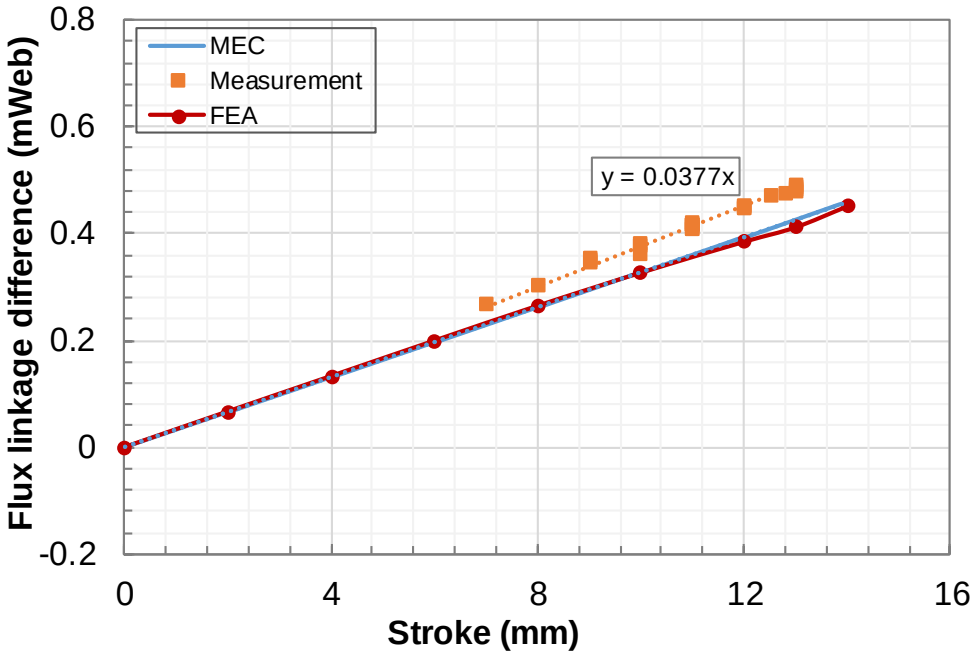

(b)

Fig. 6.10 Flux linkage difference for various strokes at resonance: (a) end core (b) middle core

6.7 Results of Stroke Detection

The FLD calculated from the measurements should be used to infer the stroke. Only one inductive coil will be needed. For each test, the difference between the FLD from the measurements and the fitted equations (shown in Fig. 6.10) indicates the accuracy of the sensor-less stroke detection technique. The error of the technique is below 4%. The inferred stroke based on the flux linkage in the middle core was plotted against the stroke measured by the LVDT transducer as shown in Fig. 6.11. The errors of the detected stroke fall within ±4% of the measured stroke.

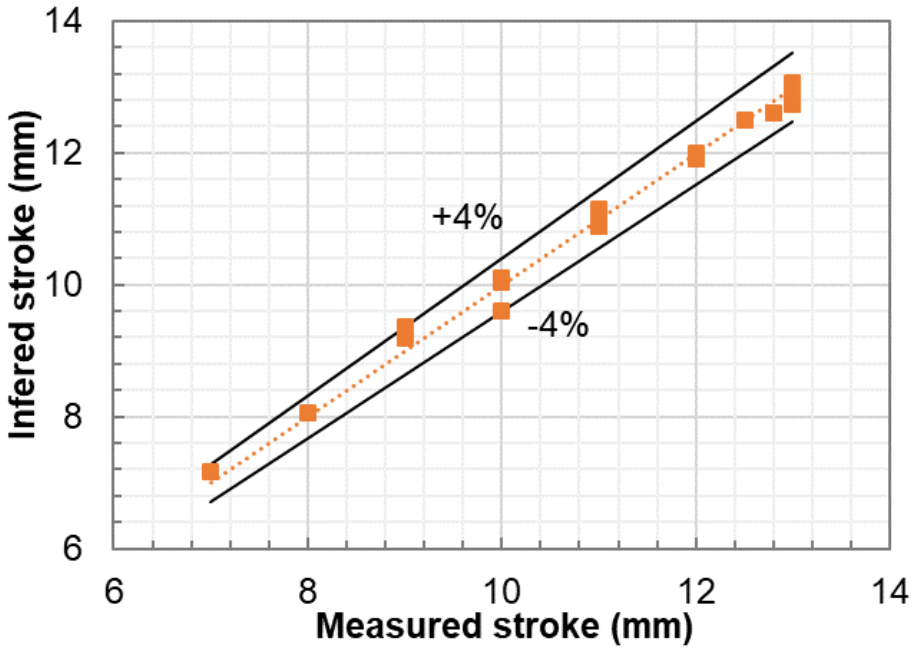

Fig. 6.11 Inferred stroke based on flux linkage in the middle core plotted against the stroke measured by the LVDT transducer

Table 6.2 shows the comparisons between the sensor-less technique and other position sensing techniques in terms of accuracy and. The present technique requires one inductive coil, one voltage sensor (voltage divider), a current sensor and a LVDT for factory

calibration. The inductive coil is a few turns of copper thus it is low-cost. The LVDT is needed only once for calibrating the relationship between the flux linkage and the piston stroke. Therefore, the present sensor-less stroke technique provides fair accuracy with almost very low cost.

Table 6.1 Comparisons between Different Sensing Techniques

Technique	Error
Present sensor-less stroke detection technique	<4%
Self-sensor of piston stroke in a linear compressor **[101]**	< 5%
Self-sensor for electromagnetic actuators **[95]**	5%
Schaevitz Sensors LVDT 02560543-006 **[161]**	0.5%

When the linear compressor is operated off-resonance, the piston displacement at zero-current crossing point (90 degree before and after the point when the derivative of the current reaches zero) is not maximum/minimum. The integration of the voltage across the inductive coil between two consecutive zero-current crossing points in one cycle will be smaller than that at resonance.

A number of off-resonance tests were conducted using the same test rig. Fig. 6.12 shows the inferred stroke using the linearly fitted equation in Fig. 6.10 at frequencies of 32 to 39 Hz with a stroke of 11 mm. The inferred strokes at operating frequencies of 36 Hz and 37 Hz are closest to the actual stroke. Note that the resonant frequency is between 36 Hz and 37 Hz for 11 mm. The closer the operating frequency approaches resonance, the larger the inferred stroke is. When the operating frequency is ±1 Hz away from the resonance, the error of the inductive coil technique is within 6%. When the operating frequency is ±2 Hz away, the error is 10%. This means that the inductive coil technique can still give reasonable accuracy of the piston stroke though the free-piston machine is off-resonance

by 1 Hz. To achieve high-accuracy stroke detection, the operating frequency needs to be very close to the actual resonance.

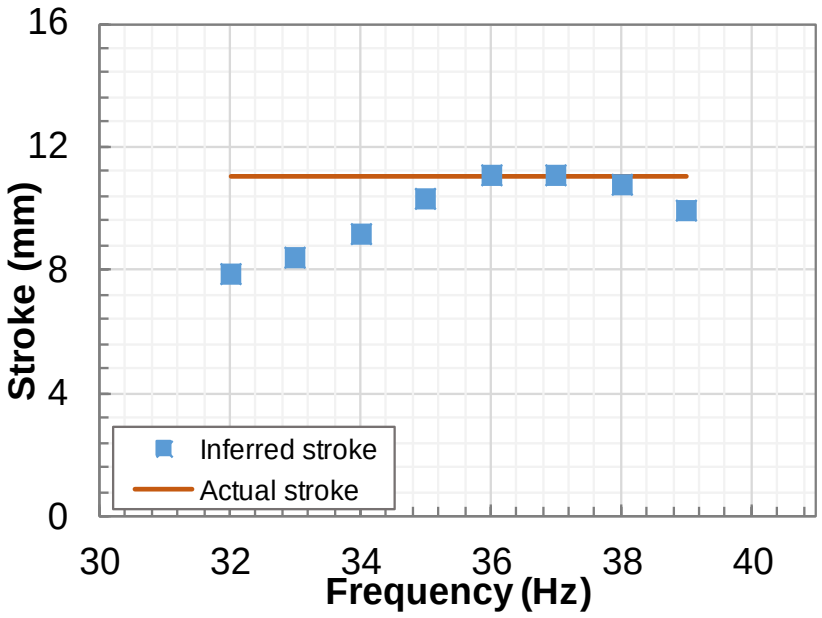

Fig. 6.12 Inferred stroke according to flux linkage difference at various operating frequencies with a stroke of 11 mm

6.8 Conclusions

Free-piston machines such as linear compressor/expander, linear IC engine/generator, and linear Stirling cooler/engine are more efficient than conventional machines due to the elimination of crank mechanism and subsequent mechanical loss. However, the key challenge is the sensing and control of the piston stroke. A novel sensor-less stroke detection technique using low-cost inductive coil cores was proposed in this chapter. The technique provides a low-cost solution to the motion sensing which is crucial to the mass production of free-piston machines. The flux linkage difference between two consecutive zero-current crossing points can be used to infer the piston stroke. A magnetic equivalent circuit model and a finite element analysis model were built to predict the theoretical flux linkage and form the basis of the technique. The inductive coil technique was experimentally implemented in a moving-magnet type linear refrigeration compressor.

Key findings are listed as below:

(1) The flux linkage induced by the magnets in the cores show a linear variation with the piston displacement. The results from MEC and FEA model shows good agreement.

(2) The slope of flux linkage induced by magnets against piston displacement for a middle core is much larger than an end core. Both the linear variation in middle core and end core can be used for the piston stroke detection.

(3) For resonant operation, the flux linkage difference is a linear function of the piston stroke. The average percentage error between the measurements and the MEC model is about 12%.

(4) A linear correlation was fitted to show the variation of flux linkage difference with the stroke, which can be used to infer the stroke in practice. The error of the technique is below 4%.

(5) The present sensor-less technique can still give reasonable accuracy of the piston stroke even if the compressor is operated at off-resonance by 1 Hz. Our future work will focus on how to ensure resonance across the range of operating conditions.

(6) The concept of the inductive coil based sensor-less technique has been successfully proved in this work. Such technique requires one inductive coil, one voltage divider, and one current sensor. The overall cost is significantly lower than existing displacement sensors such as LVDT and linear encoder. With the present technique, the piston position in free-piston machines can be cheaply sensed first before a control system can be developed to avoid the collision between the piston and the cylinder head and to modulate the power output. The present sensor-less technique can be adopted for any other moving-magnet type linear motor.

Chapter 7 Conclusions and Future Work

7.1 Conclusions

Linear compressor technologies for refrigeration were reviewed with a particular focus on linear motors that drive the motions of pistons. The performance of the moving magnet linear motor was analysed. Motor force was simulated in ANSY Maxwell and results were validated with interpolations from static force measurements. The baseline performance of the linear compressor and performance with small clearance operations were also presented. The requirement of active control of piston stroke without displacement sensor to achieve cool capacity modulation was addressed via developing two sensor-less stroke detection approaches.

7.1.1 Performance of the Linear Motor

The characteristics of the linear motor was studied. A finite element analysis model was built to model the motor force and losses of the linear motor. The static motor forces for different values of direct current at various displacements were simulated. The static motor force was validated through the static force measurements. Saturation can be observed with the increase of current. A smaller saturation current was shown for a larger armature displacement. Force constant was given by the slope of motor force against current graph. The force constant of the linear motor shows little variation with armature position when it is within 5 mm from the centre. Good agreements were shown between the computed transient motor force and interpolated results from the static force measurements. The transient motor force in one cycle is in sinusoidal waveform, and the shaft force peaks at zero displacement. Copper loss of the windings is the major loss of the linear motor, which occupies about 90% of the total loss. Compared with moving coil linear motors, moving magnet type has advantages of higher motor efficiency and

superior heat dissipation for coils. Compared with other moving magnet designs, the present linear motor provides fair motor efficiency with simple structure and low manufacturing difficulties. Part load efficiency is particularly high.

7.1.2 Performance of the Linear Compressor

The baseline performance was experimentally evaluated with helium as working fluid. Resonant frequency was calculated with linearized gas spring stiffness, magnetic spring stiffness and mechanical spring stiffness. The calculated resonance was validated experimentally. Results shows that resonance was greatly affected by pressure ratio, and resonance increases pressure ratio, but decreases with stroke. Adiabatic and isothermal efficiency decrease with pressure ratio. When operated with a larger stroke, the difference between isothermal and adiabatic efficiency for various pressure ratios tends to be smaller. Comparisons of refrigeration performances were made between various clearances and an offset of 0 mm with a fixed condenser temperature using R1234yf as refrigerant. Experimental volumetric efficiency increases as axial clearance decreases due to higher mass flow rate. However, motor efficiency decreases due to motor saturation. A 12 % increase in cooling capacity was shown when clearance was reduced from 1.07 mm to 0.4 mm with a pressure ratio of 2.5 and a stroke of 13 mm. The benefit of minimizing the clearance is significant for high pressure ratio operation.

7.1.3 Sensor-less Stroke Detection Approaches

Sensor-less stroke detection using artificial neural network was developed. Through the harmonic term sensitivity study, improvements were shown in the mean squared errors and correlation coefficients with the increase of harmonic terms from one to three. Small difference was indicated between the cases with three and six terms.

A novel sensor-less stroke detection technique using low-cost inductive coil cores was reported. The technique that used the flux linkage difference between two consecutive zero-current crossing points to infer stroke requires the linear compressor to be operated

at resonant frequency. When the resonant operation is ensured, the error of the technique is below 4%. The sensor-less technique can still give reasonable accuracy of the piston stroke even if the compressor is operated at off-resonance by 1 Hz.

Although two sensor-less stroke detection techniques were presented and both of them were proved to be feasible, merits and demerits of each technique should be summarized:

(1) The technique using inductive coil demonstrates higher accuracy and is more reliable than the neural network based approach. The technique can be implemented in any free piston machines to detect stroke. The factory calibration needs to be done before the inductive coil based technique is implemented. However, the technique requires a linear compressor to be operated at resonant frequency, the accuracy decreases as operating frequency moves away from resonance.

(2) The artificial neural network based approach requires large volume of data for network training and testing, which is time consuming. Higher risk lies in the implementation of this approach, piston colliding into cylinder results in the irrevocable damage to linear compressor, as the predicted stroke can be very inaccurate if the neural network is not well trained.

With these two sensor-less stroke detection techniques, the piston position in linear compressor can be cheaply sensed first before a control system can be developed to avoid the collision between the piston and the cylinder head and to modulate the power output. With the sensor-less stroke detection techniques and piston offset detection technique which was presented by Liang **[135]**, the linear compressor can be operated with small clearance volume without a displacement sensor.

7.2 Future Work

There are several aspects related to the linear compressor, sensor-less stroke detection techniques and operation with clearance volume that need to be further investigated.

7.2.1 Resonant Frequency Track

Linear compressors achieve the highest efficiency when operated at resonant frequency. However, resonant frequency varies with stroke, pressure ratio, and in-cylinder gas pressure. Resonant frequency tracking techniques can be developed, which allows the resonant frequency to be identified no matter how operating conditions change. Lin et al. **[156]** reported a resonant frequency tracking technique that performed frequency perturbation to reach the maximum stroke with a fixed amplitude of current. The development of resonant frequency tracking technique can address the inaccuracy of resonant calculation using linearized gas force at high pressure ratios. Reliable and fast-response resonant frequency tracking techniques improve the accuracy of sensor-less stroke detection using inductive coil.

7.2.2 The Optimization of the Linear Motor

The sensitivity of geometric parameters on the performance of linear motor can be further studied via the finite element model. The design of the linear motor can be optimized with respect to some key parameters, such as air gap, number of magnets and cores, dimensions of magnets. How shape and dimensions of core affects the performance need to be researched to achieve compact design. Approaches to optimizing the design of linear motors have been presented in previous researches **[64, 162, 163]**, with various aims, e.g., motor efficiency improvement, weight reduction with constraints of thrust and detent force. Finite element modelling, analytical modelling and genetic algorithms can be used for motor design optimization.

7.2.3 Capacity Modulation System

How clearance volume affects the refrigeration performance can be investigated via modelling the whole vapour refrigeration compression system including linear compressor, heat exchangers, valves. This can provide guidance for the operation mode for different load demands and pressure ratios and therefore achieving energy saving.

With the system model, cooling capacity modulation can be further performed. The corresponding stroke can be regulated based on the system model to achieve the desired cooling capacity.

7.2.4 Implementation of Inductive Coil in LabVIEW

The two sensor-less stroke detection techniques can be further implemented in the test rig to develop sensor-less stroke control. The multi-layer perceptron neural network and the flux linkage variation in the middle/end core can be programmed in LabVIEW. More experimental validations can be performed to compare the presented sensor-less approaches with commercial sensors and previously reported sensor-less stroke detection techniques. With the modelling of the whole refrigeration system including linear compressor, heat exchangers, and valves, model-based sensor-less stroke control can be developed to adjust stroke in accordance with external load demands.

References

[1] D. Coulomb, J. L. Dupont, and A. Pichard., The role of refrigeration in the global economy, 29th Informatory Note on Refrigeration Technologies, 2015.

[2] X. R. Liu, B. L. Wang, W. X. Shi, and P. L. Zhang, "A novel vapor injection structure on the blade of a rotary compressor," *Applied Thermal Engineering,* vol. 100, pp. 1219-1228, 2016.

[3] M. Shin, S. Na, J. Lee, B. Min, and G. Choi, "Model analysis of a novel compressor with a dual chamber for high-efficiency systems," *Applied Thermal Engineering,* vol. 158, 2019.

[4] Y. L. Teh, K. T. Ooi, and D. W. Djamari, "Theoretical study of a novel refrigeration compressor - Part II: Performance of a rotating discharge valve in the revolving vane (RV) compressor," *International Journal of Refrigeration-Revue Internationale Du Froid,* vol. 32, pp. 1103-1111, 2009.

[5] Y. L. Teh and K. T. Ooi, "Theoretical study of a novel refrigeration compressor - Part I: Design of the revolving vane (RV) compressor and its frictional losses," *International Journal of Refrigeration,* vol. 32, pp. 1092-1102, 2009.

[6] B. L. Wang, X. R. Liu, W. X. Shi, and Y. C. Ding, "An enhanced rotary compressor with gas injection through a novel end-plate injection structure," *Applied Thermal Engineering,* vol. 131, pp. 180-191, 2018.

[7] M. Stewart, *Surface Production Operations: Volume IV - Pump and Compressor Systems: Mechanical Design and Specification*, 2018

[8] X. L. Yu, Y. M. Ren, Q. Tan, Z. Lu, X. F. Jia, and X. L. Wang, "Study on the torsional movement of a reed valve in a rotary compressor," *Advances in Mechanical Engineering,* vol. 10, 2018.

[9] D. H. O. Herrmann, "Small electric refrigerating machine," Patents, 1954.

[10] R. Cadman and R. Cohen, "Electrodynamic oscillating compressors: Part 2—Evaluation of specific designs for gas loads," *ASME Journal of Basic Engineering*, pp. 664-670, 1969.

[11] R. Cadman and R. Cohen, "Electrodynamic oscillating compressors: Part 1—Design based on linearized loads," *ASME Journal of Basic Engineering*, pp. 656-663, 1969.

[12] G. Davey, "Review of the Oxford cryocooler," in *Advances in cryogenic engineering*, 1990, pp. 1423-1430.

[13] T. Bradshaw, J. Delderfield, S. Werrett, and G. Davey, "Performance of the Oxford miniature Stirling cycle refrigerator," in *Advances in cryogenic engineering*, pp. 801-809, 1986,.

[14] P. Bailey, M. Dadd, N. Hill, C. Cheuk, J. Raab, and E. Tward, "High performance flight cryocooler compressor," in *Cryocoolers 11*, pp. 169-174, 2002.

[15] N. R. Vanderwalt and R. Unger, "The simulation and design of a high-efficiency, lubricant free, linear compressor for a domestic refrigerator," *Proceedings of the*

1992 International Compressor Engineering Conference at Purdue, Vols 1-4, pp. 1-9, 1992.

[16] W. VAN DER and R. Nicholas, "Linear compressors-a maturing technology," in *International Appliance Technical Conference*, 1994, pp. 1-6.

[17] R. Redlich, R. Unger, and N. v. der Walt, "Linear compressors: motor configuration, modulation and systems," in *Proceeding of the international compressor engineering conference*, 1996, pp. 341-346,.

[18] R. Unger and N. R. van der Walt, "Linear compressors for non-CFC refrigeration," in *Proceedings International Appliance Technical Conference*, 1996, pp. 373-380.

[19] R. Unger, "Linear compressors for clean and specialty gases," in *Proceeding of the international compressor engineering conference*, 1998, pp. 73-78.

[20] R. Unger and S. Novotny, "A high performance linear compressor for CPU cooling," in *Proceeding of the international compressor engineering conference*, 2002.

[21] K. Park, E. Hong, and H. Lee, "Linear motor for linear compressor," in *Proceeding of the international compressor engineering conference,* pp. 31-38, 2002.

[22] H. Lee, S. M. Wang, and K. B. Park, "Iron loss analysis of linear motor for linear compressor," in *Proceeding of the international compressor engineering conference,* 2004.

[23] H. K. Lee, G. Song, J.-S. Park, E. Hong, W. Jung, and K. Park, "Development of the linear compressor for a household refrigerator," in *Proceeding of the international compressor engineering conference,* 2000, pp. 31-38.

[24] H. Lee, S. S. Jeong, C. W. Lee, and H. K. Lee, "Linear compressor for air-conditioner," in *Proceeding of the international compressor engineering conference,* 2004, pp. 1-7.

[25] C. R. Bradshaw, E. A. Groll, and S. V. Garimella, "A comprehensive model of a miniature-scale linear compressor for electronics cooling," *International Journal of Refrigeration,* vol. 34, pp. 63-73, 2011.

[26] C. R. Bradshaw, E. A. Groll, and S. V. Garimella, "Sensitivity analysis of a comprehensive model for a miniature-scale linear compressor for electronics cooling," *International Journal of Refrigeration,* vol. 36, pp. 1998-2006, 2013.

[27] (2016). *Embraco launches the compressor of the future*. Available: https://www.acr-news.com/embraco-future

[28] F. Possamai, D. E. Lilie, A. J. Zimmermann, and R. Mongia, "Miniature vapor compression system," in *Proceeding of the international compressor engineering conference*, 2008, pp. 1-8.

[29] A. Bijanzad, A. Hassan, I. Lazoglu, and H. Kerpicci, "Development of a new moving magnet linear compressor. Part B: Performance analysis," *International Journal of Refrigeration,* vol. 113, pp. 94-102, 2020.

[30] A. Bijanzad, A. Hassan, I. Lazoglu, and H. Kerpicci, "Development of a new moving magnet linear compressor. Part A: Design and modeling," *International Journal of Refrigeration,* vol. 113, pp. 70-79, 2020.

[31] X. Zhang, D. Ziviani, J. E. Braun, and E. A. Groll, "Experimental analysis of an oil-free linear compressor for a domestic refrigerator," *9th International Conference on Compressor and Refrigeration, 2019.*

[32] C. R. Bradshaw, E. A. Groll, and S. V. Garimella, "Linear compressors for electronics cooling: Energy recovery and its benefits," *International Journal of Refrigeration,* vol. 36, pp. 2007-2013, 2013.

[33] B. Ku, J. Park, Y. Hwang, and J. Lee, "Performance evaluation of the energy efficiency of crank-driven compressor and linear compressor for a household refrigerator," in *Proceeding of the international compressor engineering conference*, 2010, pp. 1-8.

[34] K. Liang, R. Stone, W. Hancock, M. Dadd, and P. Bailey, "Comparison between a crank-drive reciprocating compressor and a novel oil-free linear compressor," *International Journal of Refrigeration,* vol. 45, pp. 25-34, 2014.

[35] P. Bansal, E. Vineyard, and O. Abdelaziz, "Advances in household appliances - A review," *Applied Thermal Engineering,* vol. 31, pp. 3748-3760, 2011.

[36] K. Liang, "A review of linear compressors for refrigeration," *International Journal of Refrigeration,* vol. 84, pp. 253-273, 2017.

[37] F. Poltschak, "A high efficient linear motor for compressor applications," *2014 International Symposium on Power Electronics, Electrical Drives, Automation and Motion (Speedam),* pp. 1356-1361, 2014.

[38] K. Liang, "Analysis of oil-free linear compressor operated at high pressure ratios for household refrigeration," *Energy,* vol. 151, pp. 324-331, 2018.

[39] J. Beckers, D. Coppitters, W. De Paepe, F. Contino, J. Van Mierlo, and B. Verrelst, "Multi-fidelity design optimisation of a solenoid-driven linear compressor," *Actuators,* vol. 9, 2020.

[40] J. F. Gieras, Z. J. Piech, and B. Z. Tomczuk, "Linear Synchronous Motors: Transportation and Automation Systems, 2nd Edition," *Linear Synchronous Motors: Transportation and Automation Systems, 2nd Edition,* pp. 1-496, 2012.

[41] (2010). *Charles Wheatstone*. Available: https://www.kcl.ac.uk/aboutkings/history/famouspeople/charleswheatstone

[42] A. Zehden, "Electric traction apparatus," ed: Google Patents, 1905.

[43] R. Hellinger and P. Mnich, "Linear motor-powered transportation: history, present status, and future outlook," *Proceedings of the IEEE,* vol. 97, pp. 1892-1900, 2009.

[44] H. W. Lee, K. C. Kim, and J. Lee, "Review of maglev train technologies," *IEEE Transactions on Magnetics,* vol. 42, pp. 1917-1925, 2006.

[45] M. Magill, "Laboratory Experiment No.5: Advanced Induction Machine Topics," 2010.

[46] A. Cassat, N. Corsi, R. Moser, and N. Wavre, "Direct linear drives: Market and performance status," in *Proceedings of the 4th International Symposium on Linear Drives for Industry Applications*, 2003, pp. 1-11.

[47] S. Chevailler, "Comparative study and selection criteria of linear motors," 2006, .École polytechnique fédérale de Lausanne.

[48] M. Salman, "Analysis, design and control aspects of linear machines using co-simulation," 2012, KTH Royal Institute of Technology.
[49] T. Ibrahim, J. Wang, D. Howe, and N. Mohd Nor, "Design and optimisation of a moving-iron linear permanent magnet motor for reciprocating compressors using finite element analysis," *International Journal of Electrical & Computer Sciences* vol. 10, no. 2, pp. 1–7, 2010.
[50] T. H. Kim, H. W. Lee, Y. H. Kim, J. Lee, and I. Boldea, "Development of a flux concentration-type linear oscillatory actuator," *IEEE Transactions on Magnetics,* vol. 40, pp. 2092-2094, 2004.
[51] T. Ibrahim, "Short-stroke, single-phase tubular permanent magnet motors for refrigeration applications," 2009, University of Sheffield.
[52] Z. Q. Zhu, P. J. Hor, D. Howe, and J. Rees-Jones, "Novel linear tubular brushless permanent magnet motor," *Eighth International Conference on Electrical Machines and Drives,* pp. 91-95, 1997.
[53] Z. S. Al-Otaibi and A. G. Jack, "On the design of oscillating linear single phase permanent magnet motors," *Proceedings of the 41st International Universities Power Engineering Conference, Vols 1 and 2,* pp. 705-708, 2006.
[54] J. Lee, T.-B. Im, and I. Boldea, "Linear reciprocating flux reversal permanent magnetic machine," Patents, 2003.
[55] A. Hassan, A. Bijanzad, and I. Lazoglu, "Electromechanical modeling of a novel moving magnet linear oscillating actuator," *Journal of Mechanical Science and Technology,* vol. 32, pp. 4423-4431, 2018.
[56] J. B. Wang, G. W. Jewell, and D. Howe, "A general framework for the analysis and design of tubular linear permanent magnet machines," *IEEE Transactions on Magnetics,* vol. 35, pp. 1986-2000, 1999.
[57] Z. X. Jiao, T. Y. Wang, and L. Yan, "Design of a tubular linear oscillating motor with a novel compound Halbach magnet array," *IEEE-Asme Transactions on Mechatronics,* vol. 22, pp. 498-508, Feb 2017.
[58] K. J. Ko, S. M. Jang, J. H. Choi, J. Y. Choi, S. Y. Sung, and Y. T. Park, "Analysis on electric power consumption characteristics of cylindrical linear oscillatory actuator with Halbach permanent magnet array mover under electromechanical resonance frequency," *Journal of Applied Physics,* vol. 109, 2011.
[59] Y. Shen, G. Y. Liu, Z. P. Xia, and Z. Q. Zhu, "Determination of maximum electromagnetic torque in PM brushless machines having two-segment Halbach array," *IEEE Transactions on Industrial Electronics,* vol. 61, pp. 718-729, 2014.
[60] K. J. Meessen, B. L. J. Gysen, J. J. H. Paulides, and E. A. Lomonova, "Halbach permanent magnet shape selection for slotless tubular actuators," *IEEE Transactions on Magnetics,* vol. 44, pp. 4305-4308, 2008.
[61] J. Wang, Z. Lin, and D. Howe, "Analysis of a short-stroke, single-phase, quasi-Halbach magnetised tubular permanent magnet motor for linear compressor applications," *IET Electric Power Applications,* vol. 2, pp. 193-200, 2008.
[62] J. B. Wang, D. Howe, and Z. Y. Lin, "Comparative study of winding configurations of short-stroke, single phase tubular permanent magnet motor for

refrigeration applications," *Conference Record of the 2007 IEEE Industry Applications Conference Forty-Second Ias Annual Meeting,* pp. 311-318, 2007.
[63] J. B. Wang, D. Howe, and Z. G. Lin, "Comparative studies on linear motor topologies for reciprocating vapor compressors," *IEEE Iemdc 2007: Proceedings of the International Electric Machines and Drives Conference,* pp. 364-369, 2007.
[64] J. B. Wang, D. Howe, and Z. Y. Lin, "Design optimization of short-stroke single-phase tubular permanent-magnet motor for refrigeration applications," *IEEE Transactions on Industrial Electronics,* vol. 57, pp. 327-334, 2010.
[65] T. Ibrahim, J. B. Wang, and D. Howe, "Analysis and experimental verification of a single-phase, quasi-Halbach magnetized tubular permanent magnet motor with non-ferromagnetic support tube," *IEEE Transactions on Magnetics,* vol. 44, pp. 4361-4364, 2008.
[66] X. S. Luo, C. Zhang, S. P. Wang, E. Zio, and X. J. Wang, "Modeling and analysis of mover gaps in tubular moving-magnet linear oscillating motors," *Chinese Journal of Aeronautics,* vol. 31, pp. 927-940, 2018.
[67] T. Yamada, S. Koganezawa, K. Aruga, and Y. Mizoshita, "A High-performance and low-profile moving-magnet actuator for disk drives," *IEEE Transactions on Magnetics,* vol. 30, pp. 4227-4229, 1994.
[68] E. Byckling and K. Perkio, "Dynamic properties of moving magnet transducers," *IEEE Transactions on Magnetics,* vol. 16, pp. 468-473, 1980.
[69] R. E. Clark, "Resonant linear permanent magnet actuator for compressor," 2000, University of Sheffield.
[70] B. Lequesne, "Permanent-magnet linear motors for short strokes," *IEEE Transactions on Industry Applications, v*ol. 32, pp. 161-168, 1996.
[71] C. Z. Li, J. G. Li, L. F. Tang, J. Sun, H. M. Zou, and J. H. Cai, "Effects of the driving voltage waveform on the performance of vapor compression cycle system driven by the moving coil oil-free linear compressor," *International Journal of Refrigeration,* vol. 108, pp. 200-208, 2019.
[72] H. Z. Dang, J. Q. Li, J. Tan, Y. B. Zhao, R. Zha, T. Zhang*, et al.*, "Theoretical modeling and experimental verification of the motor design for a 500 g micro moving-coil linear compressor operating at 90-140 Hz," *International Journal of Refrigeration-,* vol. 104, pp. 502-512, 2019.
[73] H. Z. Dang, "Development of high performance moving-coil linear compressors for space Stirling-type pulse tube cryocoolers," *Cryogenics,* vol. 68, pp. 1-18, 2015.
[74] J. Wang, G. W. Jewell, and D. Howe, "Design optimisation and comparison of tubular permanent magnet machine topologies," *IEE Proceedings-Electric Power Applications,* vol. 148, pp. 456-464, 2001.
[75] J. B. Wang, D. Howe, and G. W. Jewell, "Analysis and design optimization of an improved axially magnetized tubular permanent-magnet machine," *IEEE Transactions on Energy Conversion,* vol. 19, pp. 289-295, 2004.
[76] M. G. Lee and D.-G. Gweon, "Optimal design of a double-sided linear motor with a multi-segmented trapezoidal magnet array for a high precision positioning

system," *Journal of magnetism and magnetic materials,* vol. 281, pp. 336-346, 2004.
[77] J. Raab and E. Tward, "Northrop Grumman aerospace systems cryocooler overview," *Cryogenics,* vol. 50, pp. 572-581, 2010.
[78] T. Nguyen, J. Raab, D. Durand, and E. Tward, "Small high cooling power space cooler," in *AIP Conference Proceedings*, 2014, pp. 365-370.
[79] A. Jomde, V. Bhojwani, and S. Deshnnukh, "Challenges in implementation of a moving coil linear compressor in a household refrigerator," *International Journal of Ambient Energy,* 2019.
[80] I. Boldea, S. A. Nasar, B. Penswick, B. Ross, and R. Olan, "New linear reciprocating machine with stationary permanent magnets," in *Proceeding of IEEE Indusrty Application Conference,* vol. 2, pp. 825-829, 1996..
[81] S. A. Nasar and I. Boldea, "Linear electrodynamic machine and method of making and using same," ed: Google Patents, 1997.
[82] B. Lequesne, "Permanent magnet linear motors for short strokes," *IEEE Transactions on Industry Applications,* vol. 32, pp. 161-168, 1996.
[83] S. A. Evans, I. R. Smith, and J. G. Kettleborough, "Permanent-magnet linear actuator for static and reciprocating short-stroke electromechanical systems," *IEEE-Asme Transactions on Mechatronics,* vol. 6, pp. 36-42, 2001.
[84] X. Li, W. Xu, C. Y. Ye, and J. G. Zhu, "Novel hybrid-flux-path moving-iron linear oscillatory machine with magnets on stator," *IEEE Transactions on Magnetics,* vol. 53, 2017.
[85] M. A. Rahman, A. Rahman, A. S. Kumar, and H. S. Lim, "CNC microturning: an application to miniaturization," *International Journal of Machine Tools & Manufacture,* vol. 45, pp. 631-639, 2005.
[86] . Ojo, W. Zhiqiao, G. Dong and S. Asuri, "High-performance speed-sensorless control of an induction motor drive using a minimalist single-phase PWM converter", *IEEE Transactions on Industry Applications*, vol. 41, no. 4, pp. 996-1004, Jul./Aug. 2005.
[87] A. Khalid and A. Nawaz, "Sensor less control of DC motor using Kalman filter for low cost CNC mchine," *2014 International Conference on Robotics and Emerging Allied Technologies in Engineering (Icreate),* pp. 180-184, 2014.
[88] T. Fukumoto, H. Hamane, and Y. Hayashi, "Performance improvement of the IPMSM position sensor-less vector control system by the on-line motor parameter error compensation and the practical dead-time compensation," in *Proceedings of the fourth Power Conversion Conference,* pp. 314-321, 2007..
[89] M. Tabrez, F. I. Bakhsh, and S. Al-Ghnimi, "Position estimators for sensor-less vector control of a Permanent Magnet Synchronous Motor," in *Proceedings of the International Conference on Intelligent Sustainable Systems,* pp. 371-374, 2017.
[90] S. Singh and A. Anvari-Moghaddam, "Sensor-based and sensorless vector control of PM synchronous motor drives: a comparative study," *In Proceedings of the 2018 IEEE 4th Southern Power Electronics Conference,* 2018, pp. 1-6.

[91] T. Ramesh, A. K. Panda, and S. S. Kumar, "Type-2 fuzzy logic control based MRAS speed estimator for speed sensorless direct torque and flux control of an induction motor drive," *ISA Transactions,* vol. 57, pp. 262-275, 2015.
[92] G. Wang, G. Zhang, and D. Xu, *Position Sensorless Control Techniques for Permanent Magnet Synchronous Machine Drives*: Springer, 2020.
[93] A. A. Z. Diab, *Development of Adaptive Speed Observers for Induction Machine System Stabilization*: Springer Nature, 2020.
[94] T. Fukumoto, H. Hamane, and Y. Hayashi, "Reduction of cyclic speed change using a bandpass filter for compressor PMSM sine-wave position sensorless drives," *Electrical Engineering in Japan,* vol. 169, pp. 75-84, 2009.
[95] B. Hanson and M. Levesley, "Self-sensing applications for electromagnetic actuators," *Sensors and Actuators a-Physical,* vol. 116, pp. 345-351, Oct 15 2004.
[96] J. Latham, "Observation and estimation study for sensorless control of linear vapor compressors," 2017, University of Louisville.
[97] R. W. Redlich, "Method and apparatus for measuring piston position in a free piston compressor," Patents, 1994.
[98] X. Y. Xu and D. W. Novotny, "Implementation of direct stator flux orientation control on a versatile Dsp based system," *IEEE Transactions on Industry Applications,* vol. 27, pp. 694-700, 1991.
[99] J. Hu and B. Wu, "New integration algorithms for estimating motor flux over a wide speed range," *IEEE Transactions on Power Electronics,* vol. 13, pp. 969-977, 1998.
[100] B. K. Bose and N. R. Patel, "A programmable cascaded low-pass filter-based flux synthesis for a stator flux-oriented vector-controlled induction motor drive," *IEEE Transactions on Industrial Electronics,* vol. 44, pp. 140-143, 1997.
[101] J. Q. Zhang, Y. F. Chang, and Z. W. Xing, "Study on Self-Sensor of Linear Moving Magnet Compressor's Piston Stroke," *IEEE Sensors Journal,* vol. 9, pp. 154-158, 2009.
[102] J. K. Son, T. W. Chun, H. H. Lee, H. G. Kim, and E. C. Nho, "Method of estimating precise piston stroke of linear compressor driven by PWM inverter," *2014 16th International Power Electronics and Motion Control Conference and Exposition,* pp. 673-678, 2014.
[103] Y. Q. Zhang, Y. Y. Ye, M. H. Yu, and Y. M. Xia, "Estimation method of mover position for linear oscillatory motor with two separated stators," *2009 International Conference on Electrical Machines and Systems,* pp. 1-4, 2009.
[104] M. S. Tang, H. M. Zou, X. Li, and C. Q. Tian, "Stroke estimation for linear compressor with energy method," *2019 IEEE International Conference on Mechatronics and Automation,* pp. 1196-1200, 2019.
[105] J. Latham, M. L. McIntyre, and M. Mohebbi, "Parameter estimation and a series of nonlinear observers for the system dynamics of a linear vapor compressor," *IEEE Transactions on Industrial Electronics,* vol. 63, pp. 6736-6744, 2016.

[106] J. Latham, M. L. McIntyre, and M. Mohebbi, "Sensorless resonance tracking and sroke control of a linear vapor compressor via nonlinear observers," *IEEE Transactions on Industrial Electronics,* vol. 65, pp. 3720-3729, 2018.
[107] J. W. Sung, C. W. Lee, G. S. Kim, T. A. Lipo, C. Y. Won, and S. Choi, "Sensorless control for linear compressors," *International Journal of Applied Electromagnetics and Mechanics,* vol. 24, pp. 273-286, 2006.
[108] K. Liang, M. Dadd, and P. Bailey, "Clearance seal compressors with linear motor drives. Part 1: Background and system analysis," *Proceedings of the Institution of Mechanical Engineers Part a-Journal of Power and Energy,* vol. 227, pp. 242-251, 2013.
[109] K. Liang, "A novel linear electromagnetic-drive oil-free refrigeration compressor," 2014, University of Oxford.
[110] R. Venkataraman, J. Rameau, and P. S. Krishnaprasad, "Characterization of an ETREMA MP 50/6 magnetostrictive actuator," Technical report of the Institute for System Research, University of Maryland at College Park, 1998
[111] (2020). *Gas Correction Factors for Thermal-based Mass Flow.* Available: https://www.mksinst.com/n/gas-correction-factors-for-thermal-based-mass-flow-controllers
[112] (2020). *Flow Measurement & Control Frequently Asked Questions*. Available: https://www.mksinst.com/n/flow-measurement-control-frequently-asked-questions
[113] (2020). *Gas Conversion Factors for 300 Series*. Available: https://www.teledyne-hi.com/resourcecenter/Documents/Gas%20Conversion%20Factors%20for%20300%20Series.pdf#search=gas%20factor
[114] Y. A. Cengel and M. A. Boles, *Thermodynamics: An Engineering Approach 6th Editon (SI Units)*: The McGraw-Hill Companies, Inc., New York, 2007.
[115] (2017). *Thermophysical Properties of Fluid Systems*. Available: https://webbook.nist.gov/chemistry/fluid/.
[116] T. Lubin, S. Mezani, and A. Rezzoug, "Development of a 2-D analytical model for the electromagnetic computation of axial-field magnetic gears," *IEEE Transactions on Magnetics,* vol. 49, pp. 5507-5521, 2013.
[117] H. Tiegna, Y. Amara, and G. Barakat, "Overview of analytical models of permanent magnet electrical machines for analysis and design purposes," *Mathematics and Computers in Simulation,* vol. 90, pp. 162-177, 2013.
[118] H. Y. Jiang, K. Liang, and Z. H. Li, "Characteristics of a novel moving magnet linear motor for linear compressor," *Mechanical Systems and Signal Processing,* vol. 121, pp. 828-840, 2019.
[119] N. Chen, Y. J. Tang, Y. N. Wu, X. Chen, and L. Xu, "Study on static and dynamic characteristics of moving magnet linear compressors," *Cryogenics,* vol. 47, pp. 457-467, 2007.
[120] X. Li, W. Xu, C. Y. Ye, and I. Boldea, "Comparative study of transversal-flux permanent-magnetic linear oscillatory machines for compressor," *IEEE Transactions on Industrial Electronics,* vol. 65, pp. 7437-7446, 2018.

[121] I. I. Abdalla, T. Ibrahim, and N. B. Nor, "Development and optimization of a moving-magnet tubular linear permanent magnet motor for use in a reciprocating compressor of household refrigerators," *International Journal of Electrical Power & Energy Systems,* vol. 77, pp. 263-270, 2016.

[122] K. J. Ko, J. H. Choi, S. M. Jang, and J. Y. Choi, "Analysis of eddy current losses in cylindrical linear oscillatory actuator with Halbach permanent magnet array mover," *Journal of Applied Physics,* vol. 111, 2012.

[123] I. Abdalla, T. Ibrahim, N. Perumal, and N. Nor, "Minimization of eddy-current loss in a permanent-magnet tubular linear motor," *International Journal on Advanced Science, Engineering and Information Technology,* vol. 7, pp. 964-970, 2017.

[124] (2019). *Ansys Maxwell*. Available: http://www.ansys.com/

[125] M. Xia and X. P. Chen, "Analysis of resonant frequency of moving magnet linear compressor of stirling cryocooler," *International Journal of Refrigeration-Revue Internationale Du Froid,* vol. 33, pp. 739-744, Jun 2010.

[126] T. W. Chun, J. R. Ahn, J. Y. Yoo, and C. W. Lee, "Analysis and control for linear compressor system driven by PWM inverter," *Iecon 2004 - 30th Annual Conference of IEEE Industrial Electronics Society, Vol. 1,* pp. 263-267, 2004.

[127] A. Smith and K. Edey, "Influence of manufacturing processes on iron losses,"in *Proceedings of* the *IEE Electrical Machines and Drives Conference*, 1995, pp. 77-81.

[128] E. Pollak, W. Soedel, R. Cohen, and F. Friedlaender, "On the resonance and operational behavior of an oscillating electrodynamic compressor," *Journal of Sound and Vibration,* vol. 67, pp. 121-133, 1979.

[129] P. S. Spoor and J. A. Corey, "A novel method for controlling piston drift in devices with clearance seals," *Cryocoolers 13,* pp. 215-223, 2005.

[130] H. Zou, S. Shao, M. Tang, L. Zhang, and G. Peng, "Performance investigation of linear compressor with one side springs," in *Proceeding of the international compressor engineering conference,* 2012, pp. 1-7.

[131] G. S. Choe and K. J. Kim, "Analysis of nonlinear dynamics in a linear compressor," *Jsme International Journal Series C-Mechanical Systems Machine Elements and Manufacturing,* vol. 43, pp. 545-552, 2000.

[132] J. Reed, D. A. Mike, B. A. Paul, P. B. Michael, and J. Raab, "Development of a valved linear compressor for a satellite borne J-T cryocooler," *Cryogenics,* vol. 45, pp. 496-500, 2005.

[133] K. Liang, R. Stone, M. Dadd, and P. Bailey, "The effect of clearance control on the performance of an oil-free linear refrigeration compressor and a comparison between using a bleed flow and a DC current bias," *International Journal of Refrigeration-Revue Internationale Du Froid,* vol. 69, pp. 407-417, 2016.

[134] H. Lee, S. Ki, S. Jung, and W. Rhee, "The innovative green technology for refrigerators development of innovative linear compressor," 2008.

[135] K. Liang, R. Stone, M. Dadd, and P. Bailey, "Piston position sensing and control in a linear compressor using a search coil," *International Journal of Refrigeration-Revue Internationale Du Froid,* vol. 66, pp. 32-40, 2016.

[136] G. Zhang, Y. Chen, Z. Zhou, and S. Li, "Design of an inductive long displacement measurement instrument," in *2006 6th World Congress on Intelligent Control and Automation*, 2006, pp. 5098-5101.

[137] (2011). *Measurement Product Guide 2011*. Available: http://www.micro-epsilon.com

[138] Y. P. Yang and Y. Y. Ting, "Improved angular displacement estimation based on Hall-effect sensors for driving a brushless permanent-magnet motor," *IEEE Transactions on Industrial Electronics,* vol. 61, pp. 504-511, 2014.

[139] A. Gupta and S. K. Arora, *Industrial automation and robotics*: Laxmi publications, 2009.

[140] Y. Yu, T. M. Choi, and C. L. Hui, "An intelligent quick prediction algorithm with applications in industrial cntrol and loading problems," *IEEE Transactions on Automation Science and Engineering,* vol. 9, pp. 276-287, 2012.

[141] K. Gurney, *An introduction to neural networks*: CRC press, 1997.

[142] J. R. Heredia, F. P. Hidalgo, and J. L. D. Paz, "Sensorless control of induction motors by artificial neural networks," *IEEE Transactions on Industrial Electronics,* vol. 48, pp. 1038-1040, 2001.

[143] V. T. Tran, H. T. Pham, B. S. Yang, and T. T. Nguyen, "Machine performance degradation assessment and remaining useful life prediction using proportional hazard model and support vector machine," *Mechanical Systems and Signal Processing,* vol. 32, pp. 320-330, 2012.

[144] C. Bennett, J. F. Dunne, S. Trimby, and D. Richardson, "Engine cylinder pressure reconstruction using crank kinematics and recurrently-trained neural networks," *Mechanical Systems and Signal Processing,* vol. 85, pp. 126-145, 15 2017.

[145] P. P. Cruz and J. J. R. Rivas, "A small neural network structure application in speed estimation of an induction motor using direct torque control," *in Proceedings of the 32nd Annual Power Electronics Specialists Conference,* pp. 823-827, 2001.

[146] S. D. J. P. P. Sonawane, "Sensorless Speed Control of Induction Motor by Artificial Neural Network," *International Journal of Industrial Electronics and Electrical Engineerin,* vol. 5, pp. 44-48, 2017.

[147] E. Mese and D. A. Torrey, "An approach for sensorless position estimation for switched reluctance motors using artifical neural networks," *IEEE Transactions on Power Electronics,* vol. 17, pp. 66-75, 2002.

[148] O. Cortes, G. Urquiza, and J. A. Hernandez, "Optimization of operating conditions for compressor performance by means of neural network inverse," *Applied Energy,* vol. 86, pp. 2487-2493, 2009.

[149] Y. H. Yu, L. E. Chen, F. R. Sun, and C. Wu, "Neural-network based analysis and prediction of a compressor's characteristic performance map," *Applied Energy,* vol. 84, pp. 48-55, 2007.

[150] K. Ghorbanian and M. Gholamrezaei, "An artificial neural network approach to compressor performance prediction," *Applied Energy,* vol. 86, pp. 1210-1221, 2009.
[151] S. Sanaye, M. Dehghandokht, H. Mohammadbeigi, and S. Bahrami, "Modeling of rotary vane compressor applying artificial neural network," *International Journal of Refrigeration,* vol. 34, pp. 764-772, 2011.
[152] J. Lundquist, "Total Harmonic Distortion and effects in electrical power systems," 2017.
[153] I. F II, "IEEE recommended practices and requirements for harmonic control in electrical power systems," *New York, NY, USA,* pp. 1-1, 1993.
[154] C. R. Bradshaw, "A Miniature-Scale Linear Compressor for Electronics Cooling," 2012, Purdue University.
[155] P. S. Dainez, J. de Oliveira, A. Nied, and M. S. M. Cavalca, "A linear resonant compressor model based on a new linearization method of the gas pressure force," *International Journal of Refrigeration,* vol. 48, pp. 201-209, 2014.
[156] Z. G. Lin, J. B. Wang, and D. Howe, "A resonant frequency tracking technique for linear vapor compressors," *in Proceedings of the International Electric Machines and Drives Conference,* pp. 370-375, 2007.
[157] S. B. Yang, "Linear compressor control circuit to control frequency based on the piston position of the linear compressor," Patents, 1999.
[158] M. Yoshida, S. Hasegawa, and M. Ueda, "Driving apparatus of a linear compressor," Patents, 2004.
[159] B. Sheikh-Ghalavand, S. Vaez-Zadeh, and A. H. Isfahani, "An improved magnetic equivalent circuit model for iron-core linear permanent-magnet synchronous motors," *IEEE Transactions on Magnetics,* vol. 46, pp. 112-120, 2010.
[160] T. W. Chun, J. R. Alm, H. H. Lee, H. G. Kim, and E. C. Nho, "A novel strategy of efficiency control for a linear compressor system driven by a PWM inverter," *IEEE Transactions on Industrial Electronics,* vol. 55, pp. 296-301, 2008.
[161] (2019). *Schaevitz Sensors LVDTs*. Available: https://www.cdiweb.com
[162] H. M. Hasanien, A. S. Abd-Rabou, and S. M. Sakr, "Design optimization of transverse flux linear motor for weight reduction and performance improvement using response surface methodology and genetic algorithms," *IEEE Transactions on Energy Conversion,* vol. 25, pp. 598-605, 2010.
[163] L. Y. Li, D. H. Pan, and X. Z. Huang, "Analysis and optimization of ironless permanent-magnet linear motor for improving thrust," *IEEE Transactions on Plasma Science,* vol. 41, pp. 1188-1192, 2013.

Appendix A FFT Code

```
clear all
close all
clc
% Import the data from Compressor Experiment 2 to 32
for i = 1:41
exp_dir = 'N:\Search Coil Data&Program\Data\10th May 2018 R134a 330g\data';
exp_name = strcat('HDAQ_calibrated_data_',num2str(i),'.xls');
exp_path = strcat(exp_dir,exp_name);
M = xlsread(exp_name);
% FFT to find out the fundamental frequency and initial value for
% minimization
% Sampling Frequency
y= M(1:5000,5);
Fs = 5000;                          % Sampling frequency
L = length(y);                          % Length of signal
Y = fft(y,L);
P2 = (abs(Y)/L); %??
P1=P2(1:(L/2+1));
```

```
P1(2:end-1)=2*P1(2:end-1);
dc=Y(1)/L;
f=Fs*(0:(L/2))/L;

theta = angle(Y);
[a1, b1]=max(P1);
mag1=a1;
f1=f(b1);
fai1=theta(b1);
%%%%%2
df=abs(f(:)-f1*2);
x=min(df);
b2=find(df==x);
mag2=P1(b2);
f2=f(b2);
fai2=theta(b2);
%%%%%3
df=abs(f(:)-f1*3);
x=min(df);
```

```
b3=find(df==x);
mag3=P1(b3);
f3=f(b3);
fai3=theta(b3);
%%%%%4
df=abs(f(:)-f1*4);
x=min(df);
b4=find(df==x);
mag4=P1(b4);
f4=f(b4);
fai4=theta(b4);
%%%%5
df=abs(f(:)-f1*5);
x=min(df);
b5=find(df==x);
mag5=P1(b5);
f5=f(b5);
fai5=theta(b5);
%%%%6
```

```
% [a6,b6]=max(P1(b5+1:end));
% mag6=a6;
% f6=f(b6);
% fai6=theta(b6);
df=abs(f(:)-f1*6);
x=min(df);
b6=find(df==x);
mag6=P1(b6);
f6=f(b6);
fai6=theta(b6);

for ii=0:1:4999
volt(ii+1,1)=dc+mag1*cos(f1*2*pi*ii/Fs+fai1)+
mag2*cos(f2*2*pi*ii/Fs+fai2)+mag3*cos(f3*2*pi*ii/Fs+fai3)+mag4*cos(f4*2*pi*ii/Fs
+fai4)+mag5*cos(f5*2*pi*ii/Fs+fai5)+mag6*cos(f6*2*pi*ii/Fs+fai6);%
end
Harmonics_volt(i,1:15)                                                    =
[i,f1,mag1,fai1,mag2,fai2,mag3,fai3,mag4,fai4,mag5,fai5,mag6,fai6,dc];
end
xlswrite('Harmonic_volt_HJ.xls', Harmonics_volt)

```

Appendix B MEC Code

```
clc
clear
L=18*0.001; %Motor width
wm=18*0.001;
wf=1*0.001; %clerance between magnets
hm=12.7*0.001; % magnet height %magnets geometry
%
g=1.5*0.001;%1.5
u0=4*pi*10^(-7);
%
Br=1.33;
Hc=10^6; %magnets material
urm=Br/(u0*Hc); % relative permeability of NdFeb
% Geometry of yoke
wy=16*0.001;
hs=(12.7+2*g)*0.001; %slot height
ri=20*0.001;
ro=72.88763648/2*0.001;%74.47/2
```

```
ra=(ri+ro)/2;
uy=1/17.74;
% Gy
theg=asin(hs/2/ri); %half of the slot arc angle
lc=2*pi*ra*(pi-theg)/pi; %arc length of the yoke
Gy=uy*wy*(ro-ri)/lc;
N=620;
ic=0;
faii=N*ic*Gy;
Gyy=lc*u0*(ro-ri)/0.022;
Gm=(u0*urm*1.8*1.8)/1.27/100;
Gmg=(u0*wf*L)/hm;
% Gmm=(u0*L)/pi*log(1+pi*g/wf);
Gmm=(u0*L)/pi*log(1+pi*g/wf);
faim=Hc*hm*Gm; %machine secondary
%%

for i=1:201
    x(i,1)=(i-1)*14*0.001/200-7*0.001;
```

```
1          xx=x(i,1)*1000;
2          D=[-9.5*0.001-x(i,1)  9.5*0.001-x(i,1)  28.5*0.001-x(i,1)  47.5*0.001-x(i,1);  -
3  28.5*0.001-x(i,1)  -9.5*0.001-x(i,1)  9.5*0.001-x(i,1)  28.5*0.001-x(i,1);  -47.5*0.001-
4  x(i,1) -28.5*0.001-x(i,1) -9.5*0.001-x(i,1) 9.5*0.001-x(i,1)];
5          theta=acos(g./sqrt(D.*D+g^2));
6  %          Gmy=u0*wmy*L*cos(theta)./sqrt(D.*D+g^2);
7  Gmy=permeag(xx);%.*cos(theta)
8  %           Gmy=abs(u0*wmy*L*g./(D.*D+g^2));
9  %          Gmy=abs(u0*wmy*L./sqrt(D.*D+g^2));
10         %% equavalent air gap permeance
11         Gs=Gmm*3*Gmg*Gmm/(2*3*Gmg*Gmm+Gmm*Gmm)+Gm;  %  equavalent
12 permeance betwween the side nodes 2,1 qnd nodes 3,8
13         % equavalent air gap permeance of Core 1-4 to magnet 1-3 at nodes 3, 5, 7
14         Gy1=Gmy(1,1)+Gmy(1,2)+Gmy(1,3)+Gmy(1,4); %core 1-4 to magnet 1 node 3
15         Gy2=Gmy(2,1)+Gmy(2,2)+Gmy(2,3)+Gmy(2,4); %core 1-4 to magnet 2 node 5
16         Gy3=Gmy(3,1)+Gmy(3,2)+Gmy(3,3)+Gmy(3,4); %core 1-4 to magnet 3 node 7
17         Gm1=Gmy(1,1)+Gmy(2,1)+Gmy(3,1);          %Magnet 1-3 to core 1 node 10, 11
18         Gm2=Gmy(1,2)+Gmy(2,2)+Gmy(3,2);          %Magnet 1-3 to core 2 node 12, 13
19         Gm3=Gmy(1,3)+Gmy(2,3)+Gmy(3,3);          %Magnet 1-3 to core 3 node 14, 15
20         Gm4=Gmy(1,4)+Gmy(2,4)+Gmy(3,4);          %Magnet 1-3 to core 4 node 16, 17
```

```
1        Airreluctance(i,1)=Gm1;
2       Airreluctance(i,2)=Gmy(1,2);
3       Airreluctance(i,3)=Gmy(2,2);
4         %%
5         P=[2*Gmm+Gmg -Gmm        0          -Gmg          0          0          0
6   0          0          0          0          0          0          0          0
7   0          0;          %1
8              -Gmm     Gs+Gy1+Gmm     -Gs          0          0          0
9   0          0          0          0          -Gmy(1,1)  0          -Gmy(1,2)  0
10  -Gmy(1,3)  0          -Gmy(1,4); %2
11             0          -Gs        Gs+Gy1+Gmm  -Gmm        0          0          0
12  0          0          -Gmy(1,1)  0          -Gmy(1,2)  0          -Gmy(1,3)  0
13  -Gmy(1,4)  0;          %3
14             -Gmg       0          -Gmm       2*Gmm+Gmg  -Gmm       0
15  0          0          0          0          0          0          0          0
16  0          0          0;         %4
17             0          0          0          -Gmm       Gy2+2*Gmm+Gm  -Gmm
18  0          0          0          -Gmy(2,1)  0          -Gmy(2,2)  0          -Gmy(2,3)
19  0          -Gmy(2,4)  0;         %5
20             0          0          0          0          -Gmm       2*Gmm+Gmg  -
21  Gmm        0          -Gmg       0          0          0          0          0
22  0          0          0;         %6
23             0          0          0          0          0          -Gmm
```

```
1  Gs+Gy3+Gmm -Gs 0 -Gmy(3,1) 0 -Gmy(3,2) 0 -
2  Gmy(3,3) 0 -Gmy(3,4) 0; %7

3  0 0 0 0 0 0 -Gs
4  Gs+Gy3+Gmm -Gmm 0 -Gmy(3,1) 0 -Gmy(3,2) 0 -
5  Gmy(3,3) 0 -Gmy(3,4); %8

6  0 0 0 0 0 -Gmg 0
7  -Gmm 2*Gmm+Gmg 0 0 0 0 0
8  0 0 0; %9

9  0 0 -Gmy(1,1) 0 -Gmy(2,1) 0 -Gmy(3,1)
10 0 0 Gm1+Gy+Gyy -Gy 0 0 -Gyy 0
11 0 0; %10

12 0 -Gmy(1,1) 0 0 0 0 0
13 -Gmy(3,1) 0 -Gy Gm1+Gy 0 0 0
14 0 0 0; %11

15 0 0 -Gmy(1,2) 0 -Gmy(2,2) 0 -Gmy(3,2)
16 0 0 0 0 Gm2+Gy+Gyy -Gy 0 0
17 -Gyy 0; %12

18 0 -Gmy(1,2) 0 0 0 0 0
19 -Gmy(3,2) 0 0 0 -Gy Gm2+Gy 0
20 0 0 0; %13

21 0 0 -Gmy(1,3) 0 -Gmy(2,3) 0 -Gmy(3,3)
22 0 0 -Gyy 0 0 0 Gm3+Gy+Gyy -Gy
23 0 0; %14

24 0 -Gmy(1,3) 0 0 0 0 0
```

```
-Gmy(3,3)  0          0          0          0          0          -Gy
Gm3+Gy     0          0;         %15

           0          0          -Gmy(1,4)  0          -Gmy(2,4)  0          -Gmy(3,4)
0          0          0          0          -Gyy       0          0          0
Gm4+Gy+Gyy -Gy;       %16

           0          -Gmy(1,4)  0          0          0          0          0
-Gmy(3,4)  0          0          0          0          0          0          0
-Gy        Gm4+Gy; ]; %17

        %

        fai=[0;    -faim;   faim;   0;    -faim;   0;    faim;   -
faim;   0;    -faii;   faii;   faii;   -faii;   -faii;   faii;   faii;   -
faii;];

        P1=inv(P);

        F=P1*fai;

        fai1(i,1)=(F(11)-F(10))*Gy;

        fai2(i,1)=(F(13)-F(12))*Gy;

        fai3(i,1)=(F(15)-F(14))*Gy;

        fai4(i,1)=(F(17)-F(16))*Gy;

end
```

Publications

1. **H. Jiang**, K. Liang*, and Z. Li, "Characteristics of a novel moving magnet linear motor for linear compressor," *Mechanical Systems Signal Processing*, vol. 121, pp. 828-840, 2019. (Associated with Chapter 3)

2. **H. Jiang**, Z. Li, and K. Liang*, "Performance of a linear refrigeration compressor with small clearance volume," *International Journal of Refrigeration,* vol. 109, pp. 105-113, 2020. (Associated with Chapter 4)

3. **H. Jiang**, K. Liang*, Z. Li, Z. Zhu, X. Zhi, and L. Qiu, "A sensor-less stroke detection technique for linear refrigeration compressors using artificial neural network," *International Journal of Refrigeration*, vol. 114, pp. 62-70, 2020. (Associated with Chapter 5)
4. **H. Jiang**, Z. Li, and K. Liang*, "A Novel Sensor-less Stroke Detection Technique using Low-cost Inductive Coil for Resonant Free-Piston Machines," *IEEE Transactions on Industrial Electronics*, vol. 68, no. 2, pp. 1087 - 1094， 2021. (Associated with Chapter 6)

5. X. Chen, **H. Jiang***, Z. Li, and K. Liang*, "Modelling and Measurement of a Moving Magnet Linear Motor for Linear Compressor," *Energies*, vol. 13, no. 15, pp. 4030, 2020. (Associated with Chapter 3)

6. **H. Jiang**, Kun L., and Z. Li. "Sensor-less position detection of oil-free linear compressor for refrigeration," *25th IIR International Congress of Refrigeration*: Montréal, Canada, August 28, 2019.

7. Z. Li, K. Liang*, and **H. Jiang**, “Thermodynamic analysis of linear compressor using R1234yf.” *International Journal of Refrigeration*, vol. 104, pp. 530-539, 2019.

8. Z. Li, **H. Jiang**, X. Chen, and K. Liang*, “Comparative study on energy efficiency of low GWP refrigerants in domestic refrigerators with capacity modulation.” *Energy and Buildings*, vol. 192, pp. 93-100, 2019.

9. Z. Li**,** K. Liang*. and **H. Jiang**, “Experimental study of R1234yf as a drop-in replacement for R134a in an oil-free refrigeration system.” *Applied Thermal Engineering*, vol. 153, pp. 646-654, 2019.

10. Z. Li, **H. Jiang**, X. Chen, and K. Liang*, “Evaporation heat transfer and pressure drop of low-gwp refrigerants in a horizontal tube.” *International Journal of Heat and Mass Transfer*, vol. 148, pp. 119-150, 2020.

11. Z. Li, **H. Jiang**, X. Chen, and K. Liang*, “Optimal refrigerant charge and energy efficiency of an oil-free refrigeration system using R134a.” *Applied Thermal Engineering*, 164, p.114473, 2020.

12. X. Chen, Z. Li *, Y. Zhao, **H. Jiang**, K. Liang *. and J. Chen*, “Modelling of refrigerant distribution in an oil-free refrigeration system using R134a.” *Energies*, vol. 12, no. 24, p.4792, 2019.

13. Z. Li, and K. Liang*, and **H. Jiang**, "Performance of an oil-free linear compressor using R1234yf." in *Proceedings of 1st IIR International Conference on the Application of HFO Refrigerants*. Vol. 1128. International Institute of Refrigeration, 2018.

14. K. Liang*, Z. Li, M. Chen, and **H. Jiang**, "Comparisons between heat pipe, thermoelectric system, and vapour compression refrigeration system for electronics cooling," *Applied Thermal Engineering*, vol. 146, pp. 260-267, 2019.